Energy-efficient silicon photonics switches towards mode-division-multiplexed interconnects

Rubana Bahar Priti

Department of Electrical & Computer Engineering

McGill University

Montreal, Canada

October 2019

A thesis submitted to McGill University in partial fulfillment of the requirements for the degree of Doctor of Philosophy.

Abstract

With sky-rocketing internet traffic and subsequent increase in data-center size and capacity, the escalating trend of power consumption has been a huge challenge in implementing energy-efficient optical interconnection networks. Silicon Photonics is considered to be a potential alternative to the electrical interconnects in high-performance computers (HPC) and data centers due to its high throughput, compatibility with CMOS fabrication, large bandwidth scalability and energy efficiency. To reduce the communication bottleneck in inter- and intra-chip data communications, the aggregated bandwidth and link capacity should be increased by using advanced multiplexing and switching techniques. In the recent years, mode-division-multiplexing (MDM) has gained attention alongside wavelength-division multiplexing (WDM) and polarization-division multiplexing (PDM) to address the challenge of Shannon's limit - the theoretical maximum data rate of a communication channel - by increasing the data transmission capacity of the on-chip optical links in data center interconnects. MDM potentially offers more scalability than both of the other two multiplexing methods by sending multiple modes in a single optical channel, and reduces energy consumption by exploiting only one laser for the transmission of multiple data channels.

In this thesis, we present energy-efficient silicon photonics switches using low-loss thermo-optic phase shifters. First, a rearrangable non-blocking broadband 4×4 Beneš switch is investigated in C-band with the detail design of the doped silicon resistive phase shifters and 2×2 Mach-Zehnder interferometer (MZI) elementary building blocks. A 2.4 μs switching time is

achieved with -11.0 dB worst case crosstalk. The design methodology leads to the inception of more innovative contribution towards silicon photonics multimode (de)multiplexing and switching. A novel reconfigurable MDM (de)multiplexer/switch is investigated for path reconfigurable switching of multiple parallel optical modulated data signals offering higher bandwidth density and lower power consumption. This multimode component is reconfigurably used in an MDM (de)multiplexer and a mode selecting switch (MSS). Simultaneous transmission of two parallel 10 Gb/s optical data packets exhibits 2.8 dB power penalty with an estimated 1.55 pJ/bit energy efficiency. Next, a scalable multimode switch is proposed using multimode interference (MMI) couplers and metal heater phase shifters. This device is capable of switching either two or three transverse electric (TE) modes increasing footprint efficiency. A detail study on scalability estimates that multimode switches can significantly reduce on-chip power by 63% compared to their single-mode counterparts. Finally, the scalability potential of this device is experimentally verified by switching three TE modes with 3×10 Gb/s aggregated bit rate and 12.0 μs switching time. The investigations of this thesis experimentally demonstrate new promises towards high-throughput data intensive multimode switching for energy-efficient optical interconnects.

Abrégé

Avec le trafic internet qui monte en flèche et l'accroissement associé de la taille et de la capacité des centres de données, la tendance à la hausse de la consommation d'énergie est un énorme défi lors de l'implémentation de réseaux d'interconnexions optiques à faible consommation énergétique. La photonique sur silicium (SiP) est considérée comme une plateforme à fort potentiel pour les ordinateurs hautes performances (HPC) et les centres de données en raison du débit binaire plus élevé, de la compatibilité avec la fabrication CMOS, de la plus grande extensibilité de la bande passante et de la haute efficacité énergétique. Pour réduire le goulot d'étranglement de communication dans les communications de données inter et intra-puces, la bande passante agrégée et la capacité de liaison devraient être augmentées en appliquant des techniques avancées de multiplexage et de commutation. Au cours des dernières années, le multiplexage par division de mode (MDM) a attiré l'attention parallèlement au multiplexage par division de longueur d'onde (WDM) et au multiplexage par division de polarisation (PDM) pour relever le défi de la limite de Shannon le débit théorique maximal de données d'un canal de communication en augmentant la capacité de transmission de données des liaisons optiques sur puce dans les interconnexions des centres de donnée. MDM offre potentiellement plus d'évolutivité que les deux autres méthodes de multiplexage en envoyant plusieurs modes dans un seul canal optique, et réduit la consommation d'énergie en exploitant un seul laser pour la transmission par le biais de plusieurs canaux de données.

Dans cette thèse, nous présentons des commutateurs photoniques sur Silicium à haute efficacité énergétique utilisant des déphaseurs thermo-optiques à faibles pertes. Tout d'abord, un commutateur Beneš 4×4 à large bande, réarrangeable et non bloquant est investigué dans la bande C. Nous présentons la conception détaillée du déphaseur résistif en silicium dopé et des blocs élémentaires que sont les interféromètres Mach-Zehnder (MZI) 2×2. Un temps de commutation de 2.4 μs est atteint avec une diaphonie de -11.0 dB dans le cas le plus défavorable. La méthodologie de conception conduit à des contributions plus innovantes au (dé)multiplexage multimode et à la commutation photonique sur Silicium. Un nouveau multiplexeur/commutateur MDM reconfigurable est étudié pour la commutation à chemin variable de plusieurs débits binaires optiques parallèles, permettant une plus grande densité de la bande passante et une consommation d'énergie réduite. Ce composant multimode est utilisé dans plusieurs configurations d'un (dé)multiplexeur MDM et d'un commutateur de sélection de mode (MSS). La transmission simultanée de deux paquets de données optiques parallèles à 10 Gb/s présente une pénalité de puissance de 2.8 dB, avec une efficacité énergétique estimée de 1.55 pJ/bit. Ensuite, un commutateur multimode extensible utilisant des coupleurs d'interférence multimode (MMI) et des déphaseurs optiques chauffants métalliques est proposé. Cet appareil est capable de commuter soit deux ou trois modes électriques transversaux (TE) augmentant l'efficacité de l'empreinte. Une étude détaillée sur l'évolutivité estime que les commutateurs multimodes peuvent réduire significativement la puissance sur puce de 63 % par rapport aux commutateurs monomodes. Ensuite, le potentiel d'extensibilité de ce dispositif est vérifié expérimentalement en commutant trois modes TE

avec une bande passante agrégée de 3×10 Gb/s et un temps de commutation de 12.0 μs. Ce travail démontre expérimentalement de nouvelles avenues vers la commutation multimode à haut débit binaire pour des interconnexions optiques à haute efficacité énergétique.

To Ramin

Acknowledgments

First, I would like to express my gratitude to Almighty Allah for giving me the strength, courage and patience to pursue this epic journey of doctoral studies. Next, I sincerely thank my PhD supervisor, Prof. Odile Liboiron-ladouceur, for giving me the privilege to be a part of her research group. It is her guidance, advice and, above all, the continuous support that has shaped this thesis in its desired form. She always inspired me to focus on technical details, which helped improve my knowledge and research skills. I am indebted to the members of my PhD committee, Prof. Michaël Ménard and Prof. Andrew Kirk, for their valuable comments and suggestions. I would also like to thank Prof. David Plant and Prof. José Azaña for sharing their resources with me on several occasions.

The graduate students of McGill's Photonics Systems Groups have been my family for the last few years. Together we struggled, learnt, and moved forward with new experiences. I really appreciate my team mates: Monireh M.P. Fard, Behnam Banan, Yule Xiong, Hamed P. Bazarghani, Guowu Zhang, Farhad Shokhraneh, and Bahaa Raadi for being there whenever I needed them. Special thanks goes to David Patel, Eslam Elfiky, Imtiaz Alamgir and Maxime Jacque for their enormous support.

It is my parents' love and prayers that have held my motivation high at all times. I am blessed with some amazing friends who have always stayed by my side with their empathy and concern. Finally, my heartfelt appreciation to my kind and caring son, whose boundless energy and smiles made this journey enjoyable.

Contents

List of Figures

List of Tables

List of Acronyms

3MS	Three-Mode Switch
ADC	Asymmetric Directional Coupler
APD	Avalanche Photo Diode
ASE	Asynchronous Source Noise
AWG	Arrayed Waveguide Grating
BER	Bit Error Rate
BOA	Booster Optical Amplifier
BOX	Buried OXide
CAGR	Compound Annual Growth Rate
CLK	Clock
CMC	Canadian Microelectronic Corporations
CMOS	Complementary Metal Oxide Semiconductor
CVD	Chemical Vapour Deposition
CW	Continuous Wave

DBR	Distributed Bragg Reflector
DC	Directional Coupler
DCA	Digital Communication Analyzer
DFB	Distributed FeedBack
DUT	Device Under Test
DUV	Deep Ultra Violet
DWDM	Dense Wavelength-Division Multiplexing
EBL	Electron Beam Lithography
ED	Error Detector
EDFA	Erbium Doped Fiber Amplifier
EME	EigenMode Expansion
EO	Electro-Optic
ER	Extinction Ratio
FA	Fiber Array
FSR	Free Spectral Range
GC	Grating Coupler
HPC	High Performance Computing
ICP	Inductively Coupled Plasma
IL	Insertion Loss
MCW	Multi Contact Wedge

MD	Mode Demultiplexer
MDM	Mode-Division Multiplexing
MFD	Mode Field Diameter
MMF	MultiMode Fiber
MMI	MultiMode Interference
MPW	Multi Project Wafer
MRM	Micro-Ring Modulator
MRR	Micro-Ring Resonator
MSM	Metal Semiconductor Metal
MSS	Mode Selecting Switch
MZI	Mach-Zehnder Interferometer
NRZ	Non-Return-to-Zero
OSNR	Optical Signal-to-Noise Ratio
PC	Polarization Controller
PD	Photo Detector
PDM	Polarization-Division Multiplexing
PGC	Phase Generating Coupler
PIC	Photonic Integrated Circuit
PPG	Pulse Pattern Generator
PRBS	Pseudo Random Bit Sequence

PS	Phase Shifter
QD	Quantum Dot
RIE	Reactive Ion Etching
RMDS	Reconfigurable Mode (De)multiplexer/Switch
RTO	Real Time Oscilloscope
SDM	Space-Division Multiplexing
S-matrix	Scattering matrix
SMF	Single Mode Fiber
SMS	Scalable Mode Switch
SNR	Signal-to-Noise Ratio
SOA	Semiconductor Optical Amplifier
SOI	Silicon-On-Insulator
SWG	Sub-Wavelength Grating
TE	Transverse Electric
TEC	Thermal Expansion Coefficient
Ti/W	Titanium/Wolfram (Tungsten)
TIA	TransImpedance Amplifier
TiN	Titanium Nitride
TM	Transverse Magnetic
TMM	Transfer Matrix Method

TO	Thermo-Optic
TOC	Thermo-Optic Coefficient
TVGC	Tunable Vertical Grating Coupler
UMZI	Unbalanced Mach-Zehnder Interferometer
VCSEL	Vertical Cavity Surface Emitting Laser
VLSI	Very-Large-Scale Integration
VOA	Variable Optical Attenuator
WDM	Wavelength-Division Multiplexing
YB	Y-Branch

Chapter 1

Introduction

The escalating demand of bandwidth density and computation speed in large-scale data centres and high-performance computing (HPC) systems enforce ultra-dense integration of several thousands of massively parallel processors in a single server. As the intra-data center IP traffic is rapidly increasing up to the range of zettabyte [1], the growing number of network resources can be constrained by its large carbon footprint. The traffic within data centers including storage, production and data development is expected to occupy 71.5% of total data center traffic by the year 2021, as shown in Fig 1.1 (adopted from [1]). The compound annual growth rate (CAGR) of electricity consumption in data centers is already double the global projection rate, imposing an environmental concern [2]. Due to continually shrinking feature sizes, higher clock frequencies, and the simultaneous growth in complexity, the role of interconnect becomes a dominant factor in determining circuit performance. Data center interconnects, consuming approximately 10% of the overall server power, will soon face

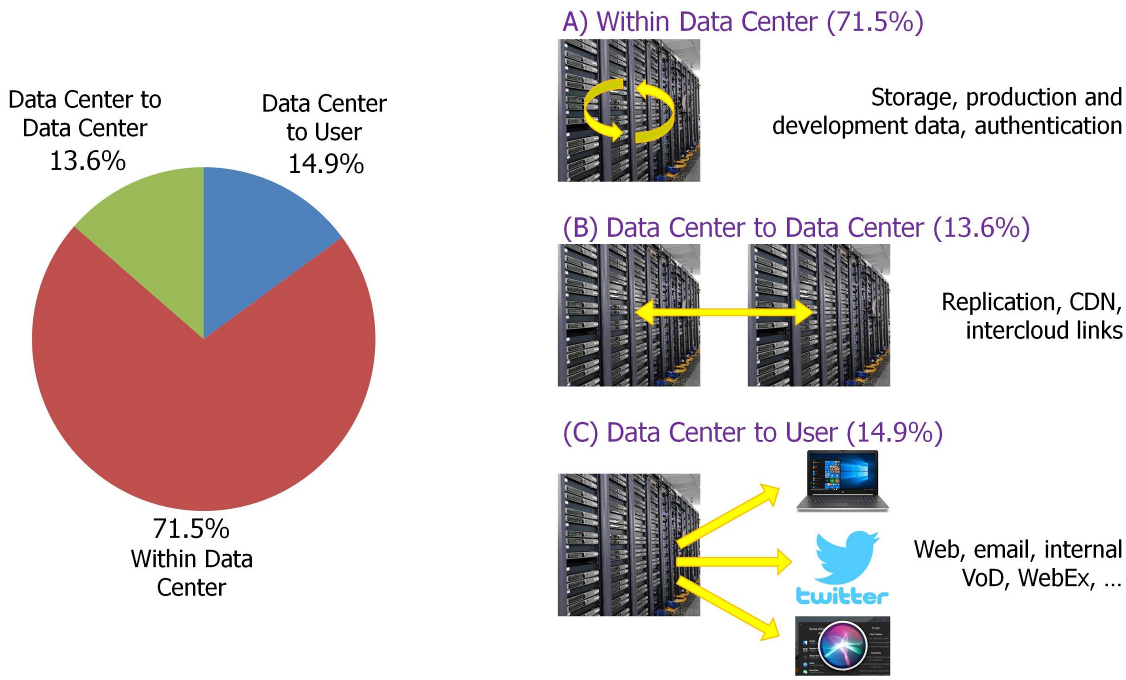

Figure 1.1 *Left*: global data center traffic by destination in 2021; *right*: examples of various categories of data center traffic (reproduced from [1]).

inevitable challenges in power handling capacity due to the big data paradigm shift [3]. The growing number of network resources in future zetta-scale data centers can be constrained by its large carbon footprint. To overcome the economic and environmental challenges in power handling capacity of on-chip and chip-to-chip communication, optical interconnects are a viable alternative to the conventional electrical interconnects [4].

1.1 Silicon photonics in short reach interconnects

Since the pioneering work of Goodman *et al.* [5], the scope and application of optical interconnects in very-large-scale integration (VLSI) electronic systems have been extensively investigated [6, 7, 8]. The perception of optical digital computing and optical switching for faster data communication gained momentum with the development of vertical cavity surface emitting lasers (VCSELs) in the early 80's [9, 10]. Today, most of the short reach interconnects are based on VCSELs and multimode fiber (MMF) [11] within the range of 100 m to 300 m. Although inexpensive, the best reported energy per bit performance of commercial VCSELs is 77 fJ/bit [12], imposing challenge to achieve the target 0.1 pJ/bit chip-to-chip energy efficiency when accounting for all the other components[13].

Photonics integrated circuit (PIC) can be a viable alternative as a cost-effective platform for optical interconnects enabling large-scale high-density integration. Different materials have been used in realizing PICs including III-V (InP/GaAs), silica (SiO_2), polymer, and silicon-on-insulator (SOI). Complementary metal oxide semiconductor (CMOS) compatible SOI technology offers low cost, low loss, low power and high bandwidth data communication improving the energy per bit performance of data center interconnects [14, 15, 16]. The substantial reduction of device size and power consumption by the silicon photonics (SiP) systems makes it a promising candidate for PIC interconnects. The commercialization of PICs takes advantage of the volume manufacturing process of CMOS foundries, which minimizes the cost while maximizing the production yield [17]. Optical interconnection in the zero-dispersion O-band (1260 nm-1360 nm) are deployed in data centers for efficient transmission between 300 m and 2 km [18]. IBM's 16 Gb/s monolithic SiP transceiver [19], Intel's 400 GHz CWDM transmitter [20], and Luxtera's 100G-PSM4 transceiver [21] are some of the state-of-the-art examples of commercial SiP systems. The flexibility of SiP for monolithic, hybrid and heterogeneous integration with electronic devices have made possible the

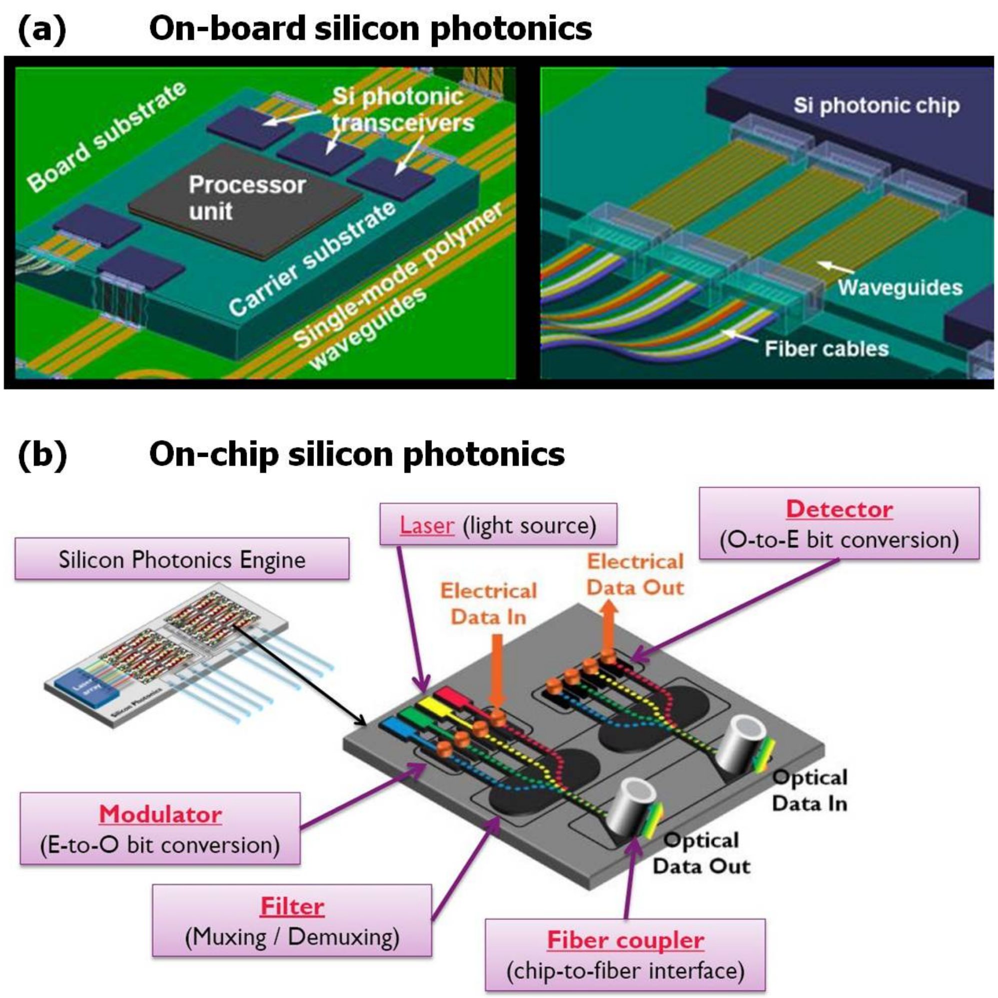

Figure 1.2 (a) *left*: Electro-optic integration of the silicon photonics chip with the processor unit, co-packaged on the same carrier (board substrate), and *right*: optical I/O connections using single-mode polymer (SMP) waveguides on carrier [22]; (b) high performance (25 Gb/s) on-chip silicon photonics transceiver [23].

ultra-dense high-speed communication systems with large bandwidth density (Gb/cm^2) for on-board (chip-to-chip) and on-chip (intra-chip) interconnects, as shown in Figs. 1.2(a) and (b), respectively.

The bandwidth density can be further increased by introducing dense wavelength-division-multiplexing (DWDM) enabling simultaneous transmission of multiple parallel data signals. Although a three wavelength-channel chip-to-chip WDM link with <1.5 pJ/bit is reported in [24], using WDM in ultra-dense short-reach interconnects (<5 cm) increases fabrication cost and system complexities due to the control, tuning and routing of tens to hundreds of optical channels. As WDM needs individual optical source for each wavelength channel, the large power requirement of the lasers significantly increases the overall power consumption diminishing the merit of DWDM in short reach interconnects [25]. To exploit the energy advantage of silicon photonics integrated circuits (PICs), DWDM should be combined with advanced multiplexing schemes, such as mode-division-multiplexing (MDM).

1.2 MDM silicon photonics systems

Conventional single-mode SiP systems reduce on-chip losses by eliminating modal dispersion and, therefore, are favorable in certain applications. Albeit the design complexity and the risk of modal crosstalk due to fabrication non-uniformity, multimode SiP is an enticing technology offering bandwidth and energy advantage over its single-mode counterpart. As the capacity of optical fiber reached a plateau, mode-division multiplexing (MDM) is implemented in fiber based networks as a design alternative to WDM [26, 27]. In recent years, MDM has gained attention for both inter- and intra-chip communication, alongside WDM and polarization-division multiplexing (PDM), to address the challenge of Shannon's limit - the theoretical maximum data rate of a communication channel - by increasing the data

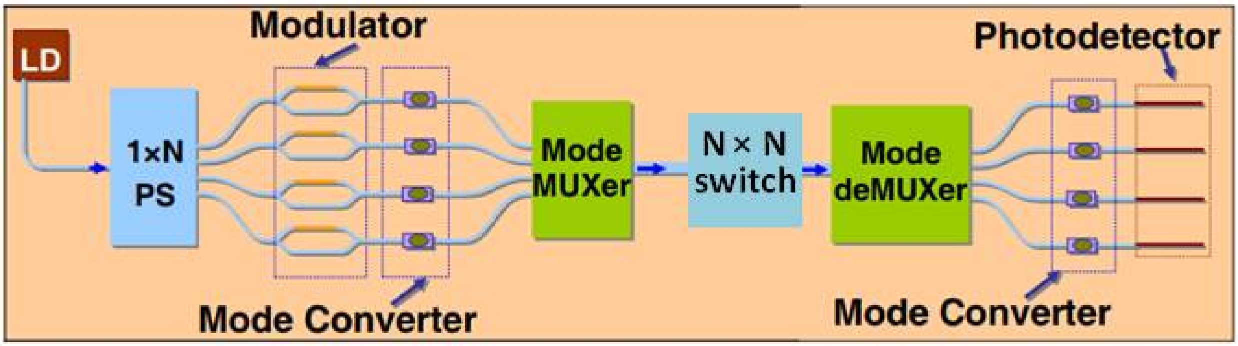

Figure 1.3 Schematic of a SiP MDM link (adapted from [33]). LD: laser diode, PS: power splitter, N: number of ports (or switch radix).

transmission capacity of the on-chip optical links in data center interconnects. In SOI PICs, the large difference in the refractive indices (Δn$\sim$2) between the silicon waveguide and the surrounding oxide allows precise control and manipulation of optical eigenmodes employing MDM as a WDM-compatible multiplexing method [28]. As individual data channels propagate over different orthogonal guided modes, one single laser can be used for multiple data channels increasing energy efficiency. MDM potentially offers more scalability by sending multiple modes in a single optical channel [29], and reduces energy consumption by exploiting only one laser for transmitting multiple data signals over single physical channel. The aggregated optical bandwidth is increased leading to higher link capacity [30]. MDM in silicon-on-insulator (SOI) is promising for high-capacity on-chip optical links and high-throughput optical switches. MDM silicon photonics systems offer efficient generation, conversion, propagation, and phase-tuning of orthogonal guided optical modes enabling the deployment of on-chip multimode reconfigurable optical space switches [31, 32].

Fig. 1.3 is an example of a typical SiP MDM system consisting of an on-chip laser (e.g., DFB, DBR or VCSEL), modulators and photodetectors. The incoming fundamental mode CW optical signal is power divided by the 1×N power splitter, where N is the number of outputs, and then modulated by the on-chip modulators. Electro-optic micro-ring modulator (MRM) or Mach-Zehnder interferometers (MZI) based modulators are usually used. The single-mode modulated data signals are converted into higher order guided modes by the mode converter, and merged in a mode multiplexer before transmitting through the multimode bus waveguide. The N×N switch is a critical component providing path reconfigurable switching in either single-mode or multimode domain. On the receiver side, the mixed mode signals are demultiplexed, and the fundamental mode signals are retrieved by another mode converter for proper detection. The mode converter, (de)multiplexer, and the N×N switch are the prime multimode components in any MDM system. In this thesis, we investigate novel designs of SiP MDM systems by using multimode interference (MMI) couplers and thermo-optic (TO) phase shifter as the building blocks.

1.3 Motivation

Optical switches with high radix may play a significant role in data centers for non-blocking routing of high-speed optical packets between servers [18]. Silicon photonic switches are essential building blocks determining the network performances such as latency, throughput, and optical signal-to-noise ratio (OSNR). From their compactness, relative low-power operation, and compatibility with CMOS, SiP optical switches have been an important prospect for both long-haul and short-reach optical interconnects to meet the bandwidth demand [34]. Already, optical interconnection in the zero-dispersion O-band (1260-1360 nm) are deployed in data centers for efficient transmission over distances between 300 m and 2 km [35]. Despite their slower switching time (μs range) compared to their electro-optic counterparts (ns range), silicon-on-insulator (SOI) thermo-optic (TO) switches offer smaller footprint with lower optical loss. Indeed, the large thermo-optic coefficient (TOC) of silicon with high thermal conductivity, and high refractive index contrast enable dense integration of high radix switch matrix. The measured TOC, $\frac{\delta n}{\delta T}$, is $1.94 \times 10^{-4} K^{-4}$ at $\lambda = 1310\ nm$, and $1.87 \times 10^{-4} K^{-4}$ at $\lambda = 1550\ nm$.

For a high radix switch matrix, the total aggregated power as well as the waste heat increase with a more challenging thermal management. The thermal crosstalk increases with denser integration, a typical scenario in a high radix switch matrix, due to ineffective localized heating. Fabrication of the switches undergo additional steps for the metallization of heater making the optimization of optical loss and operating power related to the dimension and spacing of the metallic heater more challenging. To facilitate the applications of optical switches in reconfigurable WDM photonic networks, a broadband response with high ER and low excess loss is required. Although high radix and low-loss optical space switches have been demonstrated in silicon-on-insulator (SOI) technology [36, 37], power consumption and greater scalability of these switches remain a challenge due to the increasing number of lasers, modulators, photodetectors and opto-electronic I/O interfaces associated with the large number of switch elements.

Integrated MDM switches in SOI platform can be a viable solution to leverage scalable and energy-efficient optical switching. Sending multiple data signals through a single multimode waveguide structure significantly reduces the device footprint leading to better scalability. However, robust to process variation and low-loss photonics devices are a key requirement in MDM systems, as they are more susceptible to inter-modal crosstalk than single-mode PICs [38].

1.4 Thesis organization

The objective of the works presented in this thesis is to demonstrate the proof-of-concept of SiP switches exploiting emerging technologies, like MDM. Different fabrication platforms, such as 248 nm and 193 nm deep ultraviolet (DUV) lithography, and electron beam (Ebeam) are used through cost-effective multi-project wafer (MPW) services. Data intensive applications are demonstrated with analysis of on-chip power budget and scalability.

In chapter 1, the technology roadmap towards future large-scale massively parallel data center is reviewed. The need for optical interconnects is presented in terms of energy consumption and current trend. A brief introduction of mode-division-multiplexing in section 1.2 lays the groundwork for in-depth experimental investigation presented in the later chapters. The research contribution of the candidate, Rubana Priti, is presented.

In chapter 2, the theoretical background for the SiP-based switching is discussed, which are experimentally implemented in the later chapters.The state-of-the-art of SiP TO switches is reviewed with some applications of TO matrix switches. Various types of phase shifters are explained, including a closer look at the different design approaches for the TO phase shifters. The waveguide components, that are used as building blocks in switch designs, are briefly discussed. The emerging technology of MDM SiP is studied with the concept of waveguide modes. The application and current status of SiP MDM switches are surveyed.

Chapter 3 presents a rearrangable non-blocking 4×4 Beneš switch using thermo-optically tuned 2×2 MZI building blocks. The design of the MZI building blocks and the resistive silicon phase shifters were inspired by the works reported in [39] and [40], respectively. The experimental validation of the 4×4 matrix switch with high-speed modulated data signal is presented. The dynamic switching performance was also characterized on a subset of the full switching circuit. The design methodology and characterization procedure instigated further study towards low-power SiP switches.

Chapter 4 presents a SiP MDM component capable of reconfigurably (de)multiplexing and switching of modulated optical data signals with multimode transmission. The multimode interference (MMI) based device is used for the experimental demonstration of a modal switch and a mode (de)multiplexer. The design procedure for the MMI and the operation principle for the mode (de)multiplexer/switch are explained with detail simulation results. A study of energy consumption is discussed and an improved Joule per bit (J/bit) performance is estimated.

In chapter 5, the design of a scalable multimode switch is proposed and explained with simulation results. The device is capable of switching either two or three guided modes offering footprint efficiency and energy advantage over conventional single-mode switches. Experimental characterization results are presented with both individual-mode and simultaneous dual-mode transmission for the 2-mode switch as a subset of the complete device. The scalability and power consumption is discussed with a proposed scheme for higher order mode switching.

In chapter 6, the scalable mode switch presented in the previous chapter is experimentally validated for three mode transmission. The design of an optical 120° hybrid is presented as the reconfigurable switching is enabled by this component. The design methodology of an unbalanced MZI (UMZI) using the 120° hybrid is presented. Both static and dynamic switching performance with high-speed optical data transmission is presented for the reconfigurable switching over three modes.

Chpter 7 presents a thorough planning for the extension of this thesis. As an emerging topic in the field of energy-efficient switching, SiP MDM switches have plenty of avenues to improve in terms of conceptual validation, design methodology, fabrication strategy, experimental procedure, and application. Packaging and prototyping are already a challenge for the industrialization of SiP interconnects, which also needs proper attention for the MDM systems. Some approaches to further investigate scalability, packaging, and fabrication non-uniformity are discussed in this chapter.

In chapter 8, a conclusion of the thesis is presented and the key findings are highlighted. The chapters are summarized based on the theoretical studies and experimental validations. The challenges and scopes of the works presented in each chapter are discussed.

1.5 Research Contribution

The research works presented in this thesis including the concept, design and experimental validation were conducted through continuous collaboration between Prof. Odile Liboiron-Ladouceur and the candidate, Rubana Priti. Most of the contents of this thesis are published in peer-reviewed journals or conference proceedings. The contribution of this thesis is summarized below in the order of content presented in the chapters.

- A silicon photonics mode selecting switch (MSS) is presented enabling both modal and spatial switching between the fundamental and the first-order transverse electric (TE) modes. The novel device uses multimode interference couplers offering better fabrication tolerance and larger operation range than the conventional directional coupler based mode-division-multiplexed (MDM) switches. The MSS can be used for simultaneously (de)multiplexing and switching the optical data stream in a MDM switch matrix, where the transmission of multiple independent optical data packets through a single optical link can improve the scalability and bandwidth capacity. The work was published in OSA Optics Letters, vol. 42, no. 20, 2017. The device was proposed, designed, and characterized by the candidate. Yule Xiong helped the candidate in drawing layout for fabrication. Hamed P. Bazarghani helped with the experimental measurements. Prof. Liboiron-Ladouceur supervised the work and edited the paper which was written by the candidate.

- A reconfigurable mode (de)multiplexer/switch (RMDS) is presented as the building block for the scalable and reconfigurable MDM SiP systems. This novel silicon photonics component is used as the building block in a MDM (de)multiplexer and in the the MSS. The reconfigurability of this device offers design flexibility and scalability potential to implement larger MDM systems. A power consumption analysis is performed estimating promising energy efficiency. The candidate conducted the design and the characterization of RMDS. This contribution was published in IEEE Selected Topics in Quantum Electronics, vol. 24, no. 6, 2018. Prof. Liboiron-Ladouceur supervised the work and edited the paper which was written by the candidate.

- A scalable multimode switch (SMS) is presented for the first time with detail study of scalability and power consumption. The SMS is capable of path reconfigurable switching of either the first two or first three TE modes offering footprint efficiency and scalability advantage. Simultaneous transmission of multiple parallel data signals is experimentally validated. The candidate designed, simulated and characterized this device. The work is published in IEEE Journal of Lightwave Technology in 2019. Prof. Liboiron-Ladouceur supervised the work and edited the paper which was written by the candidate.

- A three-mode switch (3MS) is presented using unbalanced Mach-Zehnder interferometer (UMZI). The unique feature of the UMZI enables reconfigurable switching of three TE modes with higher aggregated bandwidth and lower on-chip power consumption. This is the first demonstration of a UMZI based silicon photonics multimode switch.

This work was published in OSA Optics Express, vol. 27, no. 10, 2019. The design and characterization of this novel device were done by the candidate. Guowu Zhang helped in the result analysis and Matlab modelling of the UMZI. The candidate wrote the paper which was revised by Guowu Zhang. Prof. Liboiron-Ladoucer supervised the work and edited the paper.

1.6 List of publication

1.6.1 Publication related to this thesis

- Journal papers

  1. **Rubana B Priti** and Odile Liboiron-Ladouceur, "Reconfigurable and scalable multimode silicon photonics switch for energy-efficient mode-division-multiplexing systems," IEEE JLT, 2019 (in Press).
  2. **Rubana B. Priti**, Guowu Zhang, and Odile Liboiron-Ladouceur, "3×10 Gb/s silicon three-mode switch with 120° hybrid based unbalanced Mach-Zehnder interferometer," Optics Express, vol. 27, pp. 14199-14212, 2019.
  3. **Rubana B Priti** and Odile Liboiron-Ladouceur, "A reconfigurable multimode demultiplexer/switch for mode-multiplexed silicon photonics interconnects," IEEE JSTQE, vol. 24, no. 6, pp. 1-10, 2018.
  4. **Rubana B Priti**, Hamed P Bazarghani, Yule Xiong and Odile Liboiron-Ladouceur,

"Mode-selecting switch using multimode interference for on-chip optical interconnects," Optics Letters, Vol. 42, No. 20, pp. 4131-4134, 2017.

5. Yule Xiong, **Rubana B Priti** and Odile Liboiron-Ladouceur, "High-speed two-mode switch for mode-division multiplexing optical networks," Optica, Vol. 4, No. 9, pp. 1098-1102, 2017.

- Conference proceedings

1. **Rubana B Priti**, Farhad Shokraneh and Odile Liboiron-Ladouceur, "Scalable 2×2 multimode switch for mode-multiplexed silicon photonics interconnects," in Asia Communications and Photonics Conference, 2018, pp. 1-8, Hangzhou, China.

2. **Rubana B Priti** and Odile Liboiron-Ladouceur, "Mode-selecting switch using multimode interference for on-chip optical interconnects," Invited paper (Presented by the candidate) in SPIE Photonics Europe 2018, Strasbourg, France.

3. **Rubana B Priti** and Odile Liboiron-Ladouceur, "MMI-based silicon mode (de)multiplexer for multichannel parallel data transmission," in Photonics North 2018, Montreal, Canada.

4. **Rubana B Priti** and Odile Liboiron-Ladouceur, "A broadband rearrangable non-blocking MZI-based thermo-optic O-band switch in silicon-on-insulator," Invited paper in Photonics in Switching, 2017, paper no., PM4D.2, New Orleans, LA, USA.

5. **Rubana B Priti**, Yule Xiong and Odile Liboiron-Ladouceur, "Efficiency improvement of an O-band SOI MZI thermo-optic matrix switch," in 29th Annual Meeting of IEEE Photonics Society (IPC), pp. 823-824, Waikoloa, HI, USA, 2016.
6. **Rubana B Priti** and Odile Liboiron-Ladouceur, "MZI-based non-blocking SOI switches using integrated thermo-optic phase-shifter," in Advanced Photonics (Integrated Photonics Research, Silicon and Nano-Photonics), paper no., ITu1B. 3, Vancouver, BC, 2016.
7. **Rubana B Priti**, Fei Lou and Odile Liboiron-Ladouceur, "A high extinctionratio 1310 nm broadband MZI switch," in IEEE International Conference on Group Four Photonics 2015, pp. 114-115, Vancouver, BC, Canada.

1.6.2 Publication not directly related to this thesis

- Journal papers

  1. Felipe de Magalhaes, **Rubana B Priti**, Mahdi Nikdast, Fabiano Hessel, Odile Liboiron-Ladouceur and Gabriela Nicolescu, "Design and modelling of a low-latency centralized controller for optical integrated networks," IEEE Communications Letters, vol. 20, no. 3, pp. 462-465, 2016.

- Conference proceedings

  1. Felipe Gohring de Magalhaes, **Rubana B Priti**, Mahdi Nikdast, Fabiano Hessel and Odile Liboiron-Ladouceur and Gabriela Nocolescu, "A low-latency centralized

controller for MZI-based optical integrated networks," in Photonics in Switching 2015, pp. 118-120, Florence, Italy.

2. F. Lou, M.M.P. Fard, P. Liao, M.S. Hai, **Rubana B Priti**, Y. Huangfu, C. Qiu, Q. Hao, Z. Wei and O. Liboiron-Ladouceur, "Towards a centralized controller for silicon photonic MZI-based interconnects," in IEEE Optical Interconnect Conference 2015, pp. 146-147, CA, USA.

Chapter 2

Background

In this chapter, the theoretical background of different technologies for waveguide switching is described. As the works presented in the later chapters are based on thermo-optic effect, the background and applications are focused on SOI TO switches. The SiP building blocks that are used in out designs are described with their application in TO switches. A comprehensive survey is done in the context of SiP MDM systems, which is also presented in this chapter.

2.1 Thermo-optic effect in silicon

The thermo-optic coefficient (TOC) of a transparent isotropic material can be explained by the Clausius-Mossotti formula [41]

$$\frac{\varepsilon - 1}{\varepsilon + 2} = \frac{4\pi\alpha_m}{3V} \tag{2.1}$$

where, ε is the dielectric constant ($\varepsilon = n^2$; n is the complex index of refraction), α_m is the polarizability of macroscopic small sphere and V is the volume of the sphere. Differentiation of Eq. (2.1) with respect to temperature at a constant pressure leads to three physical processes: [42, 43]

- A decrease in dielectric constant due to the increase in specific volume and subsequent inter-atomic spacing in the lattice.
- An increase in polarizability with respect to volume expansion.
- The dependence of polarizability on temperature at constant volume

In 1973, Tsay *et al.* introduced a two-oscillator model to explain that the temperature dependence of the refractive index ($\frac{dn}{dT}$) is the sum of an electronic contribution consisting of two physical effects: band-to-band transition and lattice vibration [44]. The lattice contribution was found to be negligible for most semiconductors except in a very narrow frequency region near the fundamental phonon angular frequency, ω_0, and the temperature dependant refractive index is dominantly influenced by the temperature variation of the band gap ($E_g = E_0 - \frac{\alpha T^2}{T+\beta}$; T=absolute temperature, α and β are material constants) [45]. Therefore, $\frac{dn}{dT}$ is positive in a semiconductor and in the range of $\approx 10^{-4}\ K^{-1}$. However, this model is not straightforward to apply and imposes challenges as many parameters are unknown.

The Ghosh model [46] explained the TOC by considering three variables in both crystalline and amorphous silicon: thermal expansion coefficient (TEC), temperature coefficient of the excitonic band gap, and a newly introduced isentropic band gap which corresponds to the energy gap that is not affected by temperature variation [41]. For a constant $\frac{dn}{dT}$, Ghosh model can be written in the form:

$$2n\frac{dn}{dT} = GR + HR^2 \tag{2.2}$$

which resembles Sellmeier equation [47]

$$n^2(\lambda, T) = 1 + \sum_{i=1}^{m} \frac{S_i(T)\lambda^2}{\lambda^2 - \lambda_i^2(T)} \tag{2.3}$$

where S_i is the strength of the resonance due to temperature variation at the wavelength λ_i [48]. Both Eqs. (2.2) and (2.3) represent the product of the refractive index and the TOC. The constants, G and H, are called Sellmeier coefficients. They are related to the thermal expansion coefficient and to the temperature coefficient of the excitonic bandgap, respectively. These constants can be defined in terms of the TEC (α) and the excitonic band gap (E_g) by the relations:

$$\begin{cases} G = -3\alpha k^2, \\ \\ H = -\frac{1}{E_g}\frac{dE_g}{dT}k^2 \end{cases} \tag{2.4}$$

where k is the frequency dependant complex refractive index.

Figs. (2.1) and (2.2) are the measured absolute refractive index and the TOC of crys-

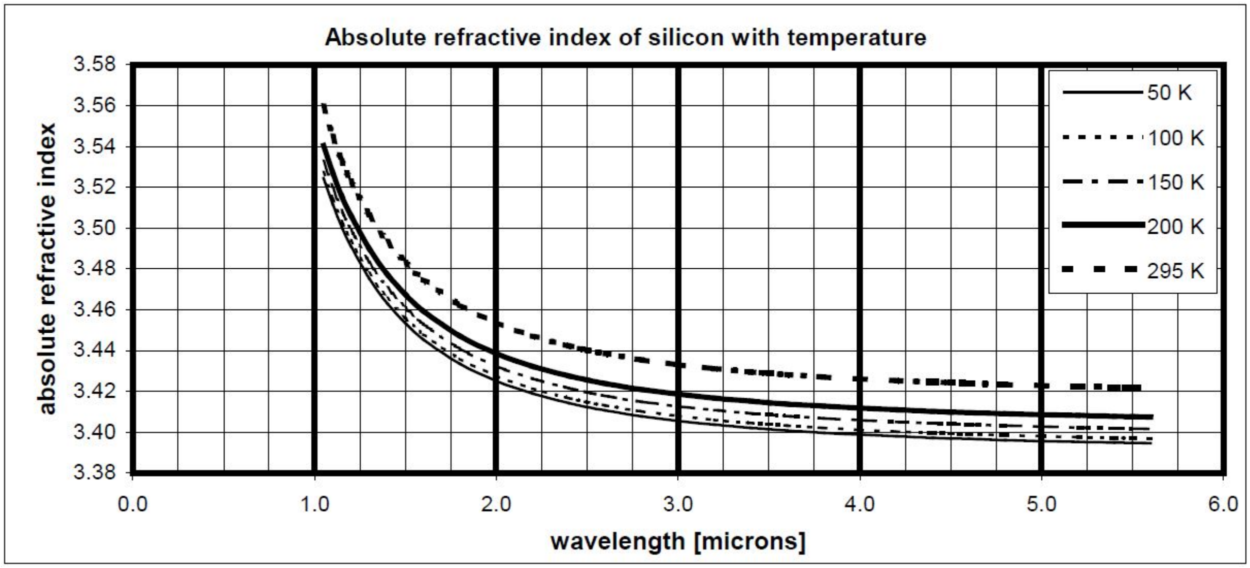

Figure 2.1 Measured absolute refractive index of silicon as a function of wavelength for selected temperatures [48].

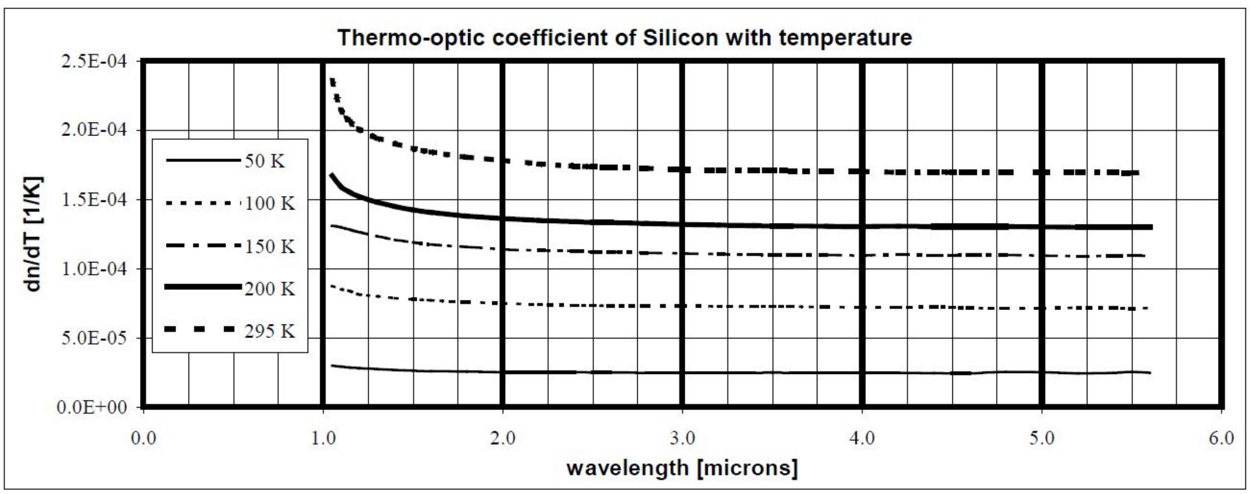

Figure 2.2 Thermo-optic coefficient ($\frac{dn}{dT}$) of silicon as a function of wavelength for selected temperatures [48].

talline silicon, respectively over 1.1 μm to 5.6 μm wavelength range for a temperature variation from 20 K to 300 K [48]. The refractive indices at 1.31 μm and at 1.55 μm for 295 K are 3.5 and 3.47, respectively. For the same temperature, the TOC at 1.31 μm and 1.55 μm are 1.94×10^{-4} and 1.84×10^{-4}, respectively.

2.1.1 Thermo-optic Phase shift

The design methodology of the SiP thermo-optic phase shifters is based on the temperature dependent change in refractive index ($\frac{dn}{dT}$) at a specific wavelength (λ) and temperature (T). A small variation in the thermally-induced refractive index can cause significant change in the optical intensity distribution inside the waveguide. The temperature gradient inside waveguide, induced by micro-heaters or phase shifters, alters the refractive index profile resulting in optical switching [49]. The relation between the refractive index (n) and temperature (T) is given by:

$$n_T = n_{T_0} + (\frac{dn}{dT})_{T-T_0} \tag{2.5}$$

where n_{T_0} and n_T are the refractive indices at temperatures T_0 and T, respectively.

For a steady-state heat transfer, the Poisson's equation ($-\nabla.(k\nabla T) = Q$) is solved for two boundary conditions [50]:

1. Dirichlet boundary condition - fixed temperature at the boundary: This is used for the bottom of the silicon substrate, considering it as a heat sink.

2. Neumann boundary condition - continuous heat flux ($-n.(k\nabla T)$) at the boundary: This applies on all other boundaries, considering them as insulators

These boundary conditions are non-homogeneous. Therefore, a simplified 1D numerical analysis is considered. We consider that the heat generated from the phase shifter uniformly dissipates in all directions, and heats up the waveguide core to induce a change in refractive index according to Eq. 2.5.

The switching time τ is the time to reach $[1 - \frac{1}{e}]$ of the steady-state temperature, and is defined by

$$\tau = \frac{0.47d^2}{\gamma} \tag{2.6}$$

where $\gamma = \frac{k}{\rho c_p}$ is the thermal diffusivity and d is the waveguide thickness. Here, ρ is the material density, c_p is the specific heat, and k is the thermal conductivity of the material. Fischer *et al.* described the transient response of a SiP TO switch by relating the switching power and the cut-off frequency, $f_c = \frac{1}{\tau}$ [51]:

$$f_c = \frac{1}{\pi \lambda \rho c_p} \frac{P_\pi}{A} (\frac{dn}{dT})_{Si} \tag{2.7}$$

where A is the heated cross-section area of the waveguide.

The power dissipation per unit length of the heater to cause a certain temperature gradient, which is required to induce switching is defined as switching power, P_π, which is a function of thermal conductivity k, and the temperature gradient $\Delta T = T - T_0$. This can be approaximated by the following relation [41]:

$$P_s \approx k\Delta T \tag{2.8}$$

Hida *et al.* proposed a 1D heat-flow model to calculate the switching power for the integrated TO switches [52]. This model is used for SOI TO switches, where on/off switching requires a π phase-shift, and can be expressed as:

$$P_\pi = \lambda k_{SiO_2}(\frac{W_H}{t_{SiO_2}} + 0.88)\frac{1}{(\frac{dn}{dT})_{Si}} \tag{2.9}$$

where $k_{SiO_2} = 1.4\ W/m.K$ and t_{SiO_2} are the thermal conductivity and the thickness of the oxide layer, respectively and W_H is the width of the phase shifter. P_π is also called heater efficiency, and expressed in mW/π.

Eq. 2.9 indicates a length independence of the tuning efficiency for a straight phase shifter suggesting that a short thermal phase shifter will achieve the same phase-shift as a long phase shifter at a higher operating temperature. However, the power consumption remains the same for both cases. Heater efficiency can be improved by more compact structure, such as folded waveguides, as heat is more concentrated in this configuration [53]. Other efficient phase shifter designs include selective undercutting of the back side of the substrate under the heater [54], and suspended phase arm by selective etching next to the phase shifter for improved thermal isolation [55].

Thermo-optic tuning is achieved by the shift in resonant wavelength in an optical filter. The change in effective refractive index of the waveguide due to the thermo-optic effect changes the effective optical path length which, in turn, causes a phase-shift in the output optical signal. For the on/off switching in an interferometric structure like MZIs, the required phase-shift between the maximum transmission T_{max} and the minimum transmission T_{min} is given by [56]:

$$\Delta\varphi = \frac{2\pi}{\lambda}(\frac{dn}{dT})_{Si}\Delta L_H \Delta T \tag{2.10}$$

where ΔT and L_H are the temperature variation and the length of the phase shifter, respectively. Two important performance matrices of a switch are the insertion loss (IL) and switching extinction ratio (ER), which are given by

$$\begin{cases} IL(dB) = 10log(\frac{T_{max}}{P_0}) \\ ER(dB) = 10log(\frac{T_{max}}{T_{min}}) \end{cases} \tag{2.11}$$

where, P_0 is the output optical power.

2.2 Different types of TO phase shifter

SiP optical switches use various phase-shift mechanism to achieve on/off switching. There are two most common mechanisms for phase-shift: free-carrier plasma dispersion effect or electro-optic (EO) effect, and TO effect. Although capable of faster switching in ns range, the EO switches are unsuitable in many applications due to their inherent passive optical loss caused by high level of doping in the waveguide core. Alternatively, the high TOC of

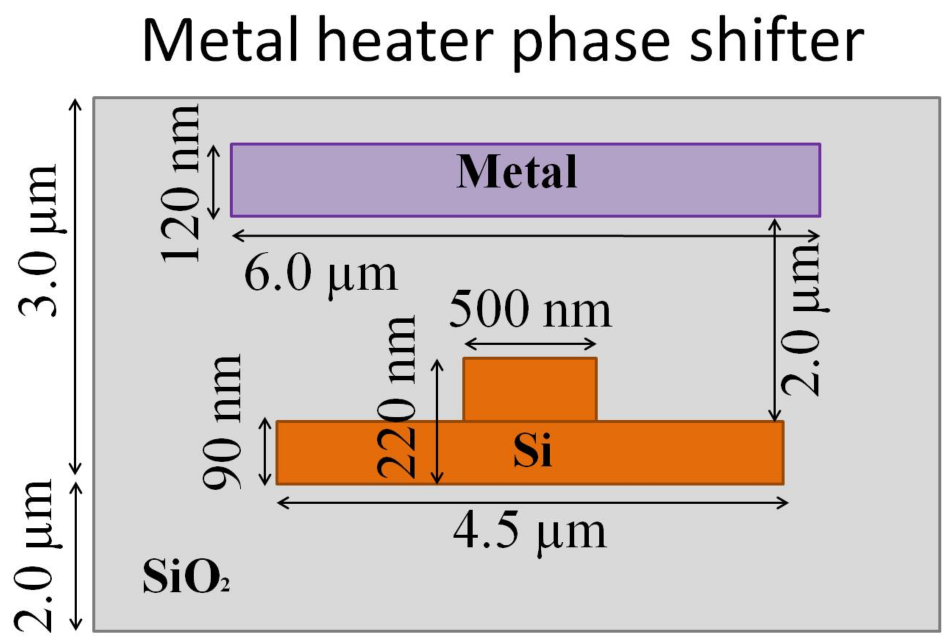

Figure 2.3 Cross-section of a metal heater phase shifter placed 2.0 μm over the silicon rib waveguide.

silicon provides good wavelength tuning efficiency of 80 pm/K, which makes resistive heaters a common option for TO phase shifters. As the works presented in this thesis are focused on TO switches, only this type of phase shifters are discussed in this section.

2.2.1 Metal film above optical waveguide

A metallic thin film is placed over the SiP waveguide to induce thermo-optic phase-shift, usually by Joule heating [57]. There are two popular methods for metal deposition: lift-off and deposition-pattern [58]. The metal is well separated from the waveguide, typically 1-2 μm, by an insulator (SiO_2) to reduce optical loss. Heat generated in the metal by ohmic heating dissipates to the substrate through the waveguide. Fig. 2.3 is an example of a cross-section for the metal heater phase shifter, where 120 nm thick and 6.0 μm wide metal film is surrounded by SiO_2 cladding 2.0 μm away from the Si waveguide. The waveguide is 500 nm $\times$ 220 nm silicon rib with 90.0 nm slab layer and 2.0 μm thick buried oxide (BOX) layer. Usually, a high resistivity and high melting point is preferred while choosing the heater material to ensure lower driving current consuming lower power, and higher operating temperature [59]. Common heater materials are tungsten, platinum, titanium alloys, etc., in the commercial SiP foundries. Due to the distance from the waveguide core, metal heaters exhibit slower switching time than the other TO phase shifters but optical loss is significantly minimized improving device IL.

2.2.2 Doped silicon alongside waveguide

For the doped silicon phase shifter placed on both sides of the waveguide core, the following design principles are maintained [60]:

1. Maximum possible overlap between the optical mode profile and temperature induced thermal profile inside waveguide core.

2. Minimum heat propagation along waveguide core.

3. Minimum optical loss.

Usually a N++/N/N++ or P++/P/P++ structure is formed by doping the silicon slab so that the heat is generated in a small region within the waveguide core. The smaller thermal conductivity of surrounding oxide than silicon core restricts heat dissipation. Sufficient

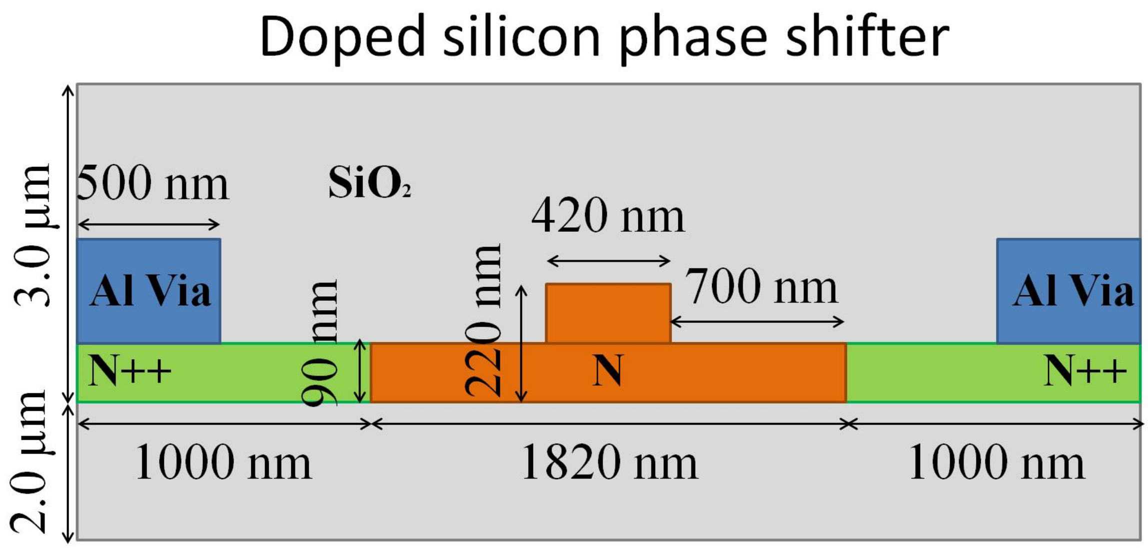

Figure 2.4 Cross-section of a doped silicon (N++ doping) phase shifter placed 700 nm away from the waveguide core.

offset is maintained between the doped region and the waveguide core reducing free-carrier induced optical loss. The direction of current flow can be controlled by proper placement of voltage and ground electrodes. If the current flows across the waveguide, the heater efficiency increases at a cost of higher optical loss. On the other hand, a parallel flow of ohmic current can significantly reduce the loss with a comparatively larger switching power. A compact (61.6 μm long) and low-loss ($\sim$ 0.23 dB) thermo-optic phase-shifter using P++/P/P++ is reported in [60], by ensuring a proper overlap of the optical mode with the p-doped silicon core. An example of the doped silicon pahse shifter is shown in Fig. 2.4.

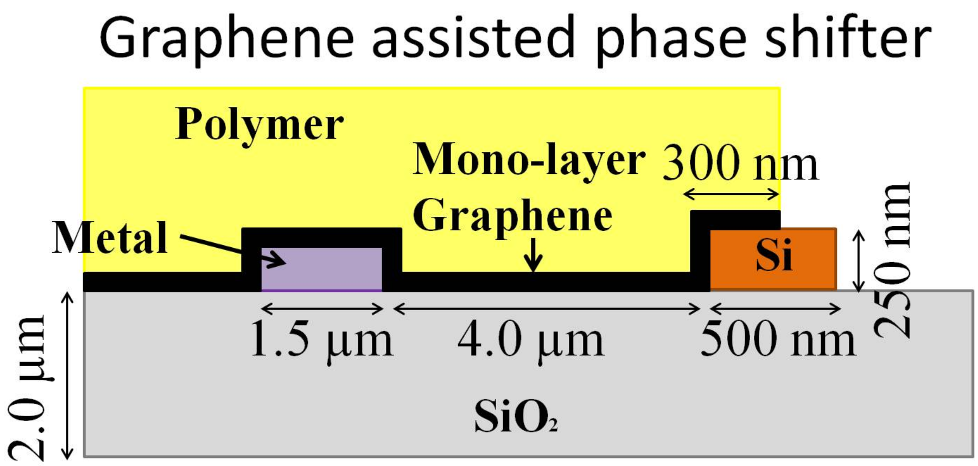

Figure 2.5 Cross-section of a graphene assisted phase shifter connecting a non-local metal heater and silicon waveguide core (image adapted from [61]).

2.2.3 Graphene assisted phase shifter

Graphene is gaining attraction in integrated TO switches for its high intrinsic thermal conductivity up to 5300 W/m.K, high carrier mobility, band-gap tunability, high optical damage threshold and excellent mechanical stability [61]. A flexible mono-layer graphene sheet of single-atom thickness is used as a transparent heat conductor from a non-local metal film to the silicon waveguide core. The chemical vapour deposition (CVD) grown graphene monolayer is transferred on to the SOI die and patterned by oxygen plasma etching. A cross-section of such a phase shifter is shown in Fig. 2.5, adapted from [61]. Due to the better thermo-electric properties of graphene than conventional metal or doped silicon, graphene assisted phase shifters exhibit faster switch response time at a lower power consumption. However, fabrication process of graphene is yet to be optimized for mass level commercial production.

2.3 SiP switch building blocks

The TO switches in SiP have been reported using a wide range of component building blocks such as, multimode interference couplers (MMIs), micro-ring resonators (MRRs), directional couplers (DCs), Y-branches (YBs), arrayed waveguide gratings (AWGs), sub-wavelength gratings (SWGs), adiabatic tapers, and so on. We extensively used tapered MMIs as a building block in our devices due to their fabrication tolerance, better wavelength insensitivity, larger switching ER and lower IL [62]. As a low-loss and efficient mode converter, asymmetric directional couplers (ADCs) have been used in the multimode switches presented in chapter 4, 5 and 6. For this reason, we discuss the design principle and applications of MMI and ADC in this section.

2.3.1 MMI coupler

MMI devices operate based on the self-imaging principle explained in [63]. This unique property of a multimode waveguide allows the input optical field to reproduce in single or multiple images at periodic distances along the waveguide length. A simple 1×1 MMI coupler is shown in Fig. 2.6 consisting of an input waveguide (port1) of width W_1, a output waveguide (port 2) of width W_2, and a multimode waveguide of width W supporting m number of guided modes. The effective refractive index of the waveguide and the cladding are n_r and n_c, respectively.

The beat length, L_π, is defined as the distance between the fundamental and the first

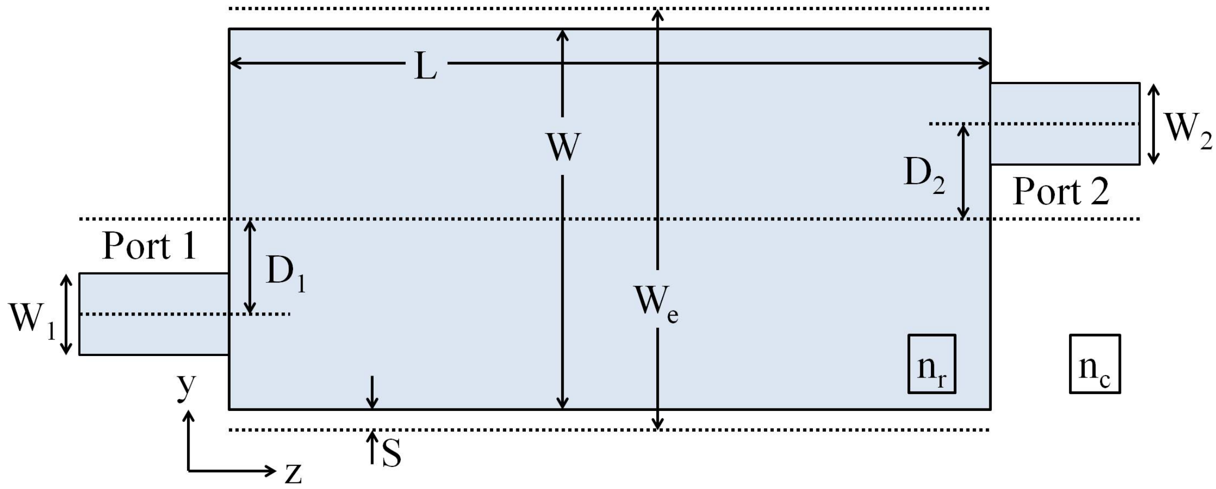

Figure 2.6 Schematic diagram of a MMI device.

order mode at the free-space wavelength λ, and is expressed as

$$L_{\pi} = \frac{\pi}{\beta_0 - \beta_1} = \frac{4 n_r {W_e}^2}{3\lambda} \tag{2.12}$$

where β_0 and β_1 are the propagation constants of fundamental and first order modes, respectively; and W_e is the effective width taking into account the Goos-Hänchen penetration depth S. In SOI waveguides, where the difference in core-cladding refractive indices is comparatively high, S is very small. So we can assume $W = W_e$, which can be expressed as

$$W_e \approx W + \frac{\lambda}{\pi}\left(\frac{n_c}{n_r}\right)^{2\sigma} \frac{1}{\sqrt{(n_r^2 - n_c^2)}} \tag{2.13}$$

where, the integer $\sigma = 0$ and $\sigma = 1$ represent TE and TM modes, respectively.

The MMI are designed following three self-imaging phenomena [63]:

1. Restricted symmetrical interference (1×N MMI): The odd mode coefficients are zero when the input is at the center of the MMI width, W.

2. Restricted paired interference (2×N MMI): The coefficients of 2nd, 5th, 8th,... modes are zero when the inputs are located at $\pm W_e/6$.

3. General interference (M×N MMI): Non-zero coefficients of all modes for arbitrary input locations.

MMI based SOI TO switches are widely used due to their broadband operation and fabrication tolerance. MMIs are used in Mach-Zehnder interferometer (MZI) configuration in polarization insensitive switches [64, 65], and in cascaded configuration to form multi output power splitter and switch [66]. Tunable MMI based switches are reported in [67, 68]. Due to the versatility of mode engineering as a function of device length, MMIs are a popular choice in SiP MDM switches [69, 70, 71, 72].

2.3.2 Directional couplers

If two guided modes in adjacent waveguides exchange power due to the physical overlap of mode wavefunctions, the modes may be coupled and the mechanism is called directional coupling [73]. The coupling coefficient of two parallel waveguides is maintained following the critical coupling condition and the coupled-mode theory [73]. The power coupled from one waveguide to the other (cross-coupled) is expressed as

$$\kappa^2 = \frac{P_{cross}}{P_0} = sin^2(C.z) \tag{2.14}$$

where P_0, $P_c ross$, C and z are input power, coupled power, coupling coefficient and coupler length. The through power, t^2, is calculated from the relation: $\kappa^2 + t^2 = 1$.

Coupling coefficient, C, is found by supermode analysis of the two coupled mode with effective refractive indices of n_1 and n_2, respectively.

$$C = \frac{\pi \Delta n}{\lambda} \tag{2.15}$$

And the cross-coupling length for full power transfer is

$$L_x = \frac{\lambda}{2\Delta n} \tag{2.16}$$

The directional couplers (DCs) are extensively used in both MRR based and MZI based SOI switches for their simple structure and compact size [74, 75]. Some variation of DCs are reported to overcome performance limitations: wide operating range is achieved using a bent DC [76], mode conversion and multiplexing is reported using asymmetric DCs [77, 78].

2.4 Mode-division-multiplexing in SOI

2.4.1 Modes in optical waveguide

In optical waveguides, mode originates from the superposition of two plane-waves propagating in opposite directions. When the electromagnetic fields of the wave components travelling in opposite to each other interfere, the resulting pattern generates a mode field [79]. For a guided even mode in a symmetric waveguide, the mode field of amplitude A at a propagation distance z has the form,

$$E_y = \frac{A}{2}[e^{+j(\kappa x - \beta z)} + e^{-j(\kappa x + \beta z)}] \tag{2.17}$$

The transverse component, κ, and the longitudinal component, z, of each plane wave continuously interfere inside the waveguide generating a standing wave pattern. Being coherent (originating from the same source), this interference pattern of the wave components is stable enough to form a mode on a specific plane.The field intensity of the mode varies with the interference minima and maxima: maximum intensity for constructive interference and minimum intensity for destructive interference.

For a given propagation constant, β, there are finite field distributions in all space inside the waveguide. These field distributions, considered as guided modes, have the general solution [79]

$$E(x, y, z) = E(x, y)e^{-j\beta z} \tag{2.18}$$

The shape and phase of a specific mode is determined from the terms $E(x, y)$ and $e^{-j\beta z}$, respectively. The main properties of the modes are as follows:

1. Each eigenvalue of β refers to a distinct guided mode inside the waveguide corresponding to a unique field distribution.
2. The number of guided mode is finite inside a waveguide of finite dimension.
3. All modes are orthogonal.
4. The degenerate modes have the same β values but unique field distributions.
5. The allowed mode inside the waveguide makes a complete set where any continuous field distribution is caused by the superposition (Eq. 2.17).

2.4.2 Number of guided modes

Fig. 2.7 is a sketch of mode propagation inside optical waveguide of refractive index n_f surrounded by a substrate of index n_s and a top cladding of index n_c. The electric and magnetic field distributions are shown for the first three quasi transverse electric (quasi-TE) and the quasi transverse magnetic (quasi-TM) modes, respectively. The number of modes in a waveguide is assumed by the relation

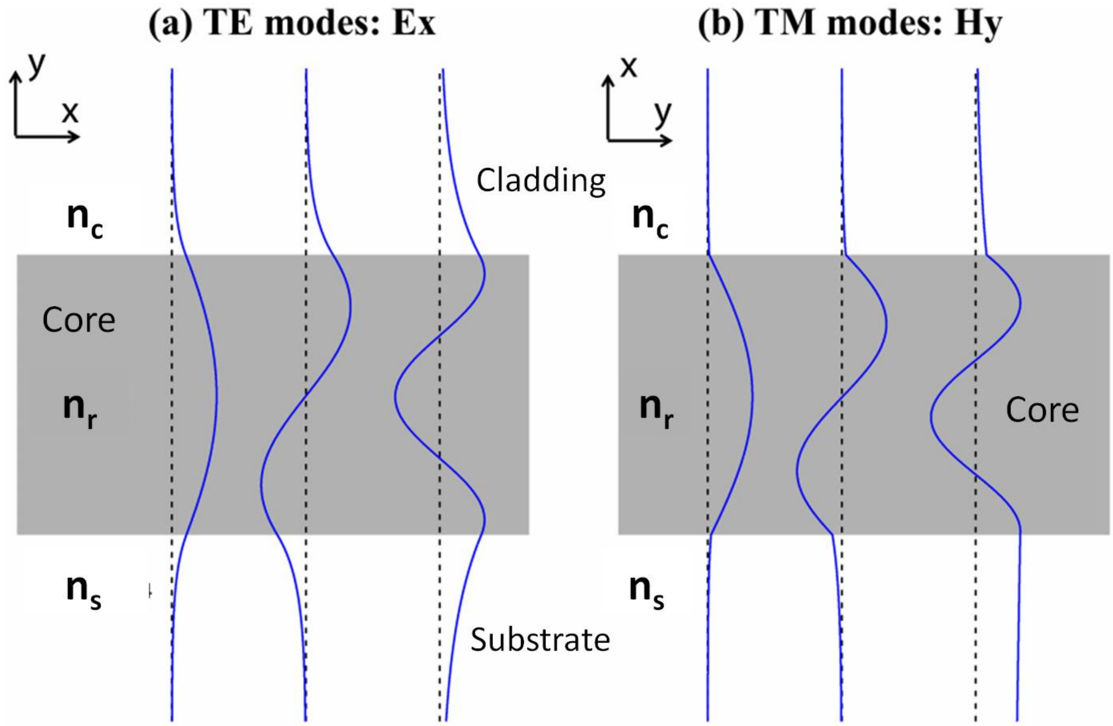

Figure 2.7 Cross-section of a waveguide showing (a) electric field profiles in TE, and (b) magnetic field profiles in TM mode propagation along z direction, perpendicular to x-y plane. (Image adapted from [80]).

$$m \approx \frac{V}{\pi} \tag{2.19}$$

where V is the normalized frequency of the waveguide. The general dispersion relation and cut-off condition for single-mode propagation in a slab waveguide is expressed in terms of the normalized frequency V, asymmetry parameter a, and normalized effective index b. If the effective refractive index of the cross-section in Fig. 2.17 is $n_{eff} = \frac{\beta}{k_0}$, these three parameters are expressed as

$$V = hk_0({n_r}^2 - {n_s}^2)^{1/2} \tag{2.20}$$

$$a = \frac{({n_s}^2 - {n_c}^2)}{({n_r}^2 - {n_s}^2)} \tag{2.21}$$

$$b = \frac{({n_{eff}}^2 - {n_s}^2)}{({n_r}^2 - {n_s}^2)} \tag{2.22}$$

where $k_0 = \frac{2\pi}{\lambda}$ is the wavenumber (magnitude of the wave vector) in vacuum. By numerically plotting the values of b as a function of V for the discrete values of a ($0 \leq a \leq \infty$), we find the single-mode cut-off condition at $b = 0$. This condition is critical to ensure single-mode propagation in a waveguide.

Mode engineering in SiP waveguides takes in to account the structural parameters (e.g., V, and n_{eff}), number of allowed modes (m) and couple-mode theory [73] for designing compact, low-loss, and high-throughput multimode devices. Mode orthogonality, which ensures simultaneous propagation of multiple guided optical modes within a structure without any overlap in their field distributions, is the basis of mode-division-multiplexing (MDM). However, inter-modal cross-coupling is not completely eliminated in practice due to fabrication non-uniformity, caused by inefficient etching and other physical processes during waveguide fabrication. For this reason, investigation for more robust, versatile and low-loss MDM SiP devices are in great demand.

2.5 Progress in MDM SiP

The dispersion curve for a silicon channel waveguide is shown in Fig. 2.8 demonstrating high birefringence and mode dispersion with waveguide width variation [81]. This allows formation, propagation and manipulation of multiple guided modes in SiP waveguides with lower excess loss and lower inter-modal crosstalk. MDM in SiP serves the same purpose as the widely used space-division-multiplexing (SDM) in optical fiber [82, 83]. In recent years, significant research effort is given towards the development of on-chip MDM links including, but not limited to, multimode channel and rib waveguides, multimode waveguide crossings, on-chip multichannel mode (de)multiplexers, and reconfigurable multimode switches.

2.5.1 Mode converter

Mode converters are reported using various components, such as symmetric and asymmetric Y-junctions, adiabatic linear and non-linear tapers, Asymmetric directional couplers (ADCs) and MMI couplers. Two 3-dB Y-splitter/combiner is joined in MZI configuration for mode conversion in InP material by applying a phase-shift by the path-length difference in the MZI arms [84]. A MMI based mode converter is proposed by Guo *et al.*, in InP [85], and by Hosseini *et al.*, in SOI platform [86]. An experimental demonstration on SiP MMI based mode conversion is reported in [87]. The ground breaking works of Dai *et al.*, on MDM SiP brought out linear adiabatic tapers based mode conversion using both single-etch and bi-level fabrications [88]. A fabrication tolerant, more compact and scalable design

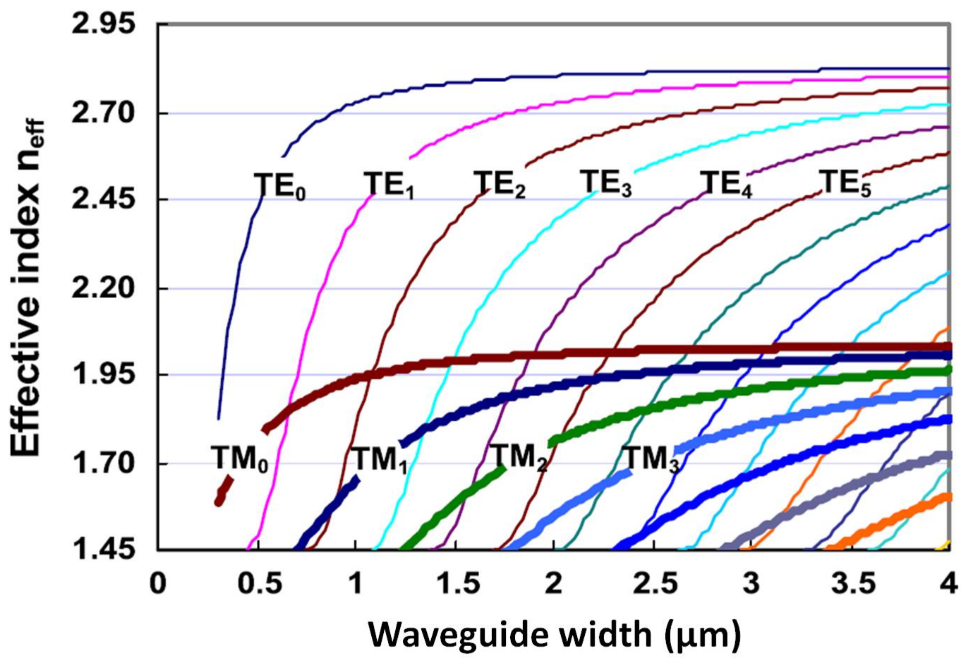

Figure 2.8 Effective refractive indices of TE and TM modes in a 220 nm thick silicon channel waveguide with SiO_2 top and buried oxide, as a function of waveguide width from 0 μm to 4.0 μm at 1550 nm wavelength. (Image adapted from [77]).

is later reported by Chen *et al.*, for arbitrary mode conversion [89]. Cascaded MMI and passive waveguide phase shifter is used for fundamental to second-order mode conversion [90]. Although these structures demonstrate low-loss and efficient conversion between first two or first three guided modes, scalability potential for higher order mode exchange is not experimentally demonstrated in most cases.

2.5.2 Mode (de)multiplexer

Multimode (de)multiplexers are one of the most important building blocks in an on-chip MDM system. Leuthold *et al.*, first proposed on-chip mode conversion and multiplexing using MMI couplers and passive phase shifters for first two TE modes [91, 72]. Several geometries were experimentally measured for both equal and unequal power splitting ratio. This concept was further investigated with better scalability in [92], and with wider tuning capability in [71]. Similar concept for mode (de)multiplexing was used in [93] in combination with PDM and WDM. We also implemented this idea of MMI based mode manipulation in our works. Dai *et al.*, first implemented ADC based mode (de)multiplexer as a potential device for WDM compatible MDM systems [77], which was also reported in [94] and [95]. The Y-junctions are a popular MDM component for their compact size, simple fabrication and straight forward application. Single and cascaded asymmetric Y-junctions are used as a mode (de)multiplexer in [96] and [97], respectively.

Different components are often combined to improve efficiency, operating range and fabrication tolerance. For example, the wavelength sensitivity of Y-junction was significantly reduced by combining it with asymmetric adiabatic couplers in [98, 99]. Similarly, Y-junction and MMI couplers are combined for compact and low-loss mode conversion in [100, 101]. Recently, a three-waveguide-coupling scalable mode (de)multiplexer is reported using MMI coupler, thermo-optic phase shifter and ADC [102]. Advanced fabrication methods are being explored for 3D (de)multiplexing of higher order modes by using vertically coupled components [103, 104]. WDM and MDM are combined demonstrating 4.35 Tb/s aggregated data transmission over 87 WDM channels using MRR and tapered directional couplers [30]. A 64-channel hybrid (de)multiplexer is reported using AWG and ADC [105]. On-chip MDM link exploiting the propagation of optical supermode using closely-spaced SOI waveguides is also reported [106, 106].

2.5.3 Mode switch

Reconfigurability is an important requirement in a SiP MDM interconnects, which is implemented by multimode switches. MDM switches are emerging as a new design alternative to the reconfigurable DWDM systems for their higher link-capacity and lower power consumption. However, as phase-tuning of higher order modes is challenging in SiP, some form of mode-manipulation is required before reconfigurable switching, such as mode decomposition, demultiplexing, and filtering.

A reconfigurable multimode switch was demonstrated for the first time by Stern *et al.*, by using MRR based WDM-MDM filters and tapered mode converters [107]. Two wavelength channels, each carrying modulated optical data over two spatial modes, were switched achieving 4×10 Gb/s aggregated bandwidth with -16.8 dB crosstalk. Y-junctions were used for mode (de)multiplexing before the active phase-tuning using a p-i-n [108] and metallic phase shifter [109] in MZI configurations. This idea of MZI based switching was further explored in [110], which exploited several single-mode MZIs merged in to few-mode waveguide in the I/O ports.

On-chip MDM switches with mode exchange operation were reported using tapered directional couplers [111], asymmetric Y-junctions [112], and MRRs [113]. In [31, 32], a 2×2 multimode switch was reported as the building block in a two-wavelength four-mode WDM-MDM matrix switch consisting of tapered ADCs, MMIs and TO phase shifters. The scalability of this device is further investigated and a general architecture for N×N multimode switch was proposed in [114]. Low-loss multimode waveguide crossings are used with MRR based mode-converters in [115] for (de)multiplexer-free reconfigurable mode switching.

We demonstrated a mode selecting switch using cascaded MMI couplers and TiN TO phase shifters in [70] and a high-speed two-mode switch in [116]. We also proposed a reconfigurable and scalable three-mode switch in [117], which was experimentally tested with 3×10 Gb/s aggregated bandwidth in [118].

2.6 Summary

In this chapter, we reviewed the theoretical background of the physical processes in SiP switches. The concept of waveguide modes and the basic principle of mode-multiplexing are also discussed. The elementary building blocks that are included in the MDM PICs, including MMIs and ADCs, are also discussed. We limit the discussion to TO phase shifters as this is our design choice for switching applications. TO switches offer lower loss and smaller footprint than electro-optic switches at a slower switching speed. However, as the switching time-constant is also limited by the arbitration time of the electronic controller, we believe that TO switches are reasonable to use in board-level reconfigurable switching and routing applications.

A brief survey on SiP MDM components presented including mode converter, mode (de)multiplexer and mode switch. As an emerging topic in SiP optical interconnects, MDM based systems are evolving at a fast rate with newer components, fabrication methods and scalability ideas. We tried to merge with this research upsurge with our works on MDM switches.

Chapter 3

Rearrangable non-blocking 4×4 Beneš switch

Optical switches with high radix may play a significant role in data centers for non-blocking routing of high-speed optical packets between servers. Optical interconnections in the zero-dispersion O-band (1260-1360 nm) are currently deployed in data centers for efficient transmission between 300 m and 2 km [35]. From their compactness, relative low-power operation, and CMOS compatibility, SOI optical switches have been an important prospect to meet the escalating bandwidth demand of data center IP traffic [34]. Albeit their slower switching time (μs range) compared to their electro-optic counterparts (ns range), SOI thermo optic switches exhibits lower optical losses enabling scalability in the number of ports with greater network topology options for non-blocking switches. SOI-based thermo-optic switches have been demonstrated using Mach-Zehnder Interferometer (MZI) [74, 119], microring resonator

[120] and multimode interferometer [121]. Thermally tuned MZI switches have been reported with relatively fast switching of a few microseconds with reasonable power and high extinction ratio. However, these switches have large footprint [53, 56] limiting their application for large port-count switch matrix. A thermo-optic phase shift is typically provided by an over-clad metal heater which requires large power consumption due to the inefficient phase shifter [74]. A more energy-efficient approach for thermo-optic phase-shift is to use doped silicon resistive heater, as reported in [119], for low-loss low-power SiP switches.

In this chapter, the performance of a thermo-optically tuned broadband 4×4 rearrangable non-blocking Beneš switch is experimentally assessed operating in the O-band (1320 nm-1380 nm). Thermal tuning is achieved with resistive elements using highly doped silicon slab parallel to the silicon rib waveguide [119]. Instead of conventional directional couplers that are more susceptible to fabrication process variation [122], wavelength insensitive phase generating couplers (PGC) are used leading to the broadband operation of the switch [123]. The dynamic switching ability is experimentally verified with transmission of 10 Gb/s optical payload signal. With crosstalk optimized switch biasing, bit-error-rate (BER) of 10^{-12} is achieved for 16 possible routing data path.

3.1 Design and fabrication

The 4×4 Beneš switch structure is shown in Fig. 3.1(a). The matrix switch consists of six 2×2 MZI switches as elementary building blocks, as shown in Fig. 3.1(b). The 2×2 switch

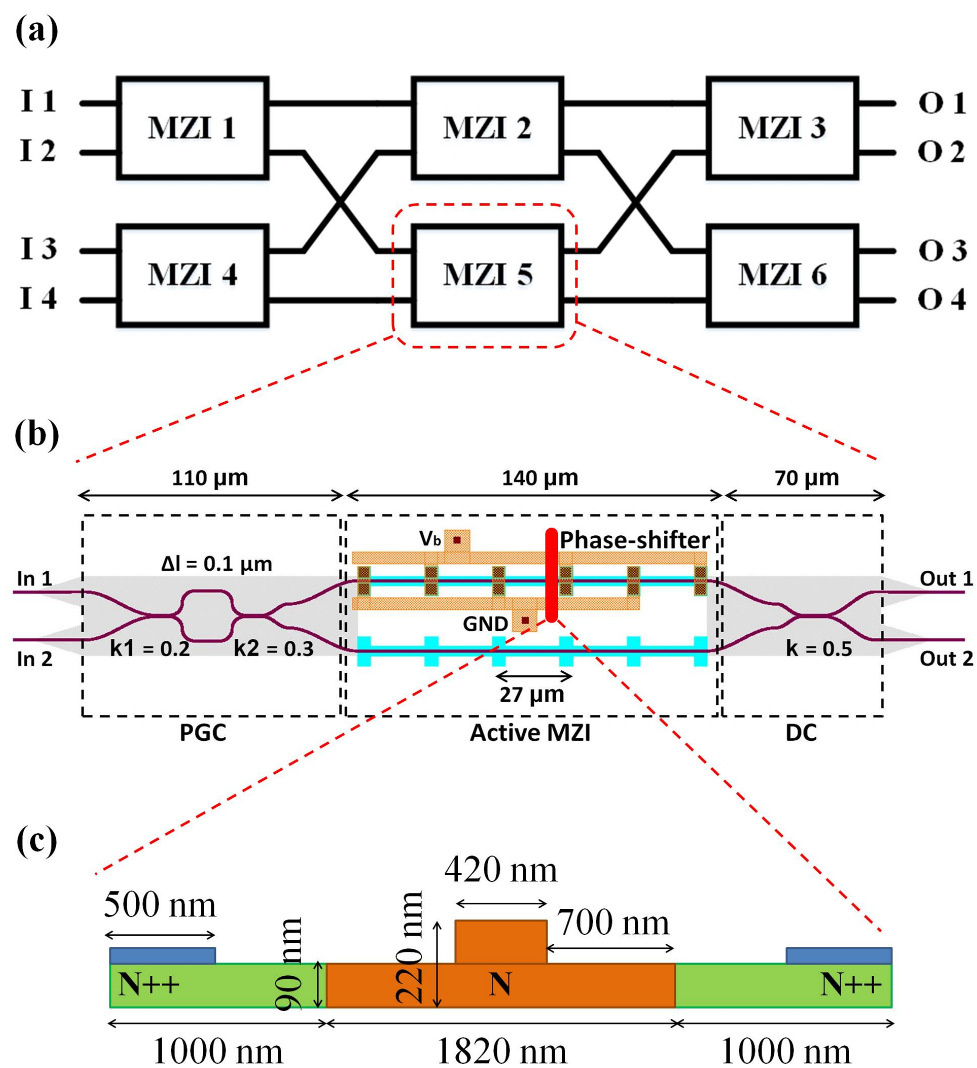

Figure 3.1 (a) Schematic of the 4×4 Beneš switch; (b) detailed layout of the 2×2 MZI with integrated thermo-optic phase shifter; (c) cross-section of the MZI arm showing the configuration of the phase shifter.

is designed using SOI ridge waveguides of 420 nm width and 220 nm height with a 90 nm thick silicon slab supporting single-mode transverse electric (TE) transmission at 1310 nm. The waveguide cross-section is shown in Fig. 3.1(c). The 2×2 MZI building block has a compact footprint of 0.0112 mm^2 (320 μm × 35 μm). The thermal phase shifter and PGC are optimized for efficient switching demonstrating low power consumption/π-phase shift with a broadband operation.

Broadband operation is achieved by adding a PGC in the input while keeping the output 3-dB coupler unchanged - a trade off between robustness and operating range (Fig. 3.1(b)). The PGC, a one-stage MZI lattice form, consists of two directional couplers of unequal coupling ratios ($\kappa 1$ and $\kappa 2$) and a small path difference (Δl). The path difference causes out-of-phase transmissions between two arms due to a small difference in propagation constants. The phase difference flattens the coupling ratio over a broad spectral range resulting in wavelength insensitive 3 dB coupler [123, 124, 125]. Numerically optimized, the coupling coefficients of the first and second directional couplers of the PGC are $\kappa 1 = 0.2$, $\kappa 2 = 0.3$, and the path length difference is $\Delta \mathrm{l} = 0.1\,\mu$m.

3.1.1 Phase shifter design

The thermo-optic phase shifter consists of a n-doped 1.0 μm wide silicon slabs, which is placed 700 nm away from the side of the 420 nm waveguide core (Fig. 3.1(c)). High concentration of doping (N++) decreases ohmic resistance leading to a low-resistance current path for resistive heating, confined by the surrounded oxide. The center of the waveguide is doped more lightly (N) to reduce optical loss in the core region. Although the phase shifter is placed in the upper arm of the MZI, both arms are identically doped to balance optical loss. Each doped resistor is 27 μm long, 1 μm wide, and each arm consists of five resistive elements. The segmented resistors in the phase shifter are connected to the bias voltage and

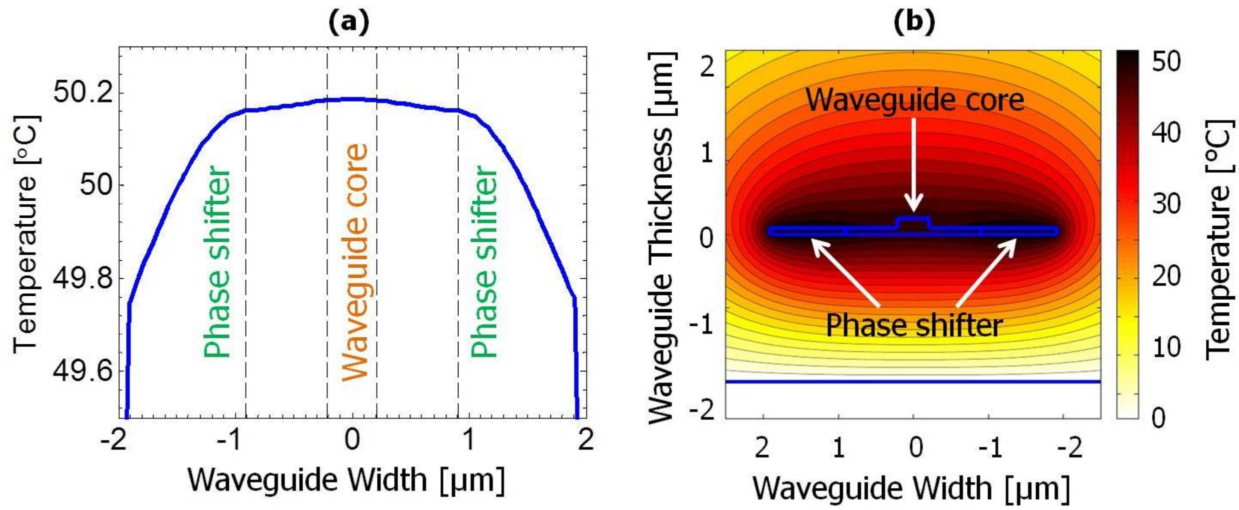

Figure 3.2 (a) Simulated 1D temperature profile as a function of waveguide width, (b) simulated 2D temperature profile of the waveguide cross-section as a function of waveguide width.

ground pads in a way that the resistors are all parallel to each other. In this configuration, the current flows parallel to the waveguide core, significantly reducing the optical loss.

The 1D and 2D temperature profiles of the waveguide cross-section as a function of waveguide width are shown in Figs. 3.2(a) and (b), respectively, simulated using the partial differential equation (PDE) tool in Matlab. A uniform temperature rise upto around 50 °C is observed with a steep temperature rise in the phase shifter regions. Proper heat dissipation inside the surrounding oxide confirms good thermal isolation between the waveguide core and the silicon substrate. The change in temperature in the waveguide core and the phase-shift are also simulated with respect to the bias voltage applied to the 2×2 MZI building block (Fig. 3.3(b)).

Doped silicon resistive phase shifter has several advantages over conventional metal heater

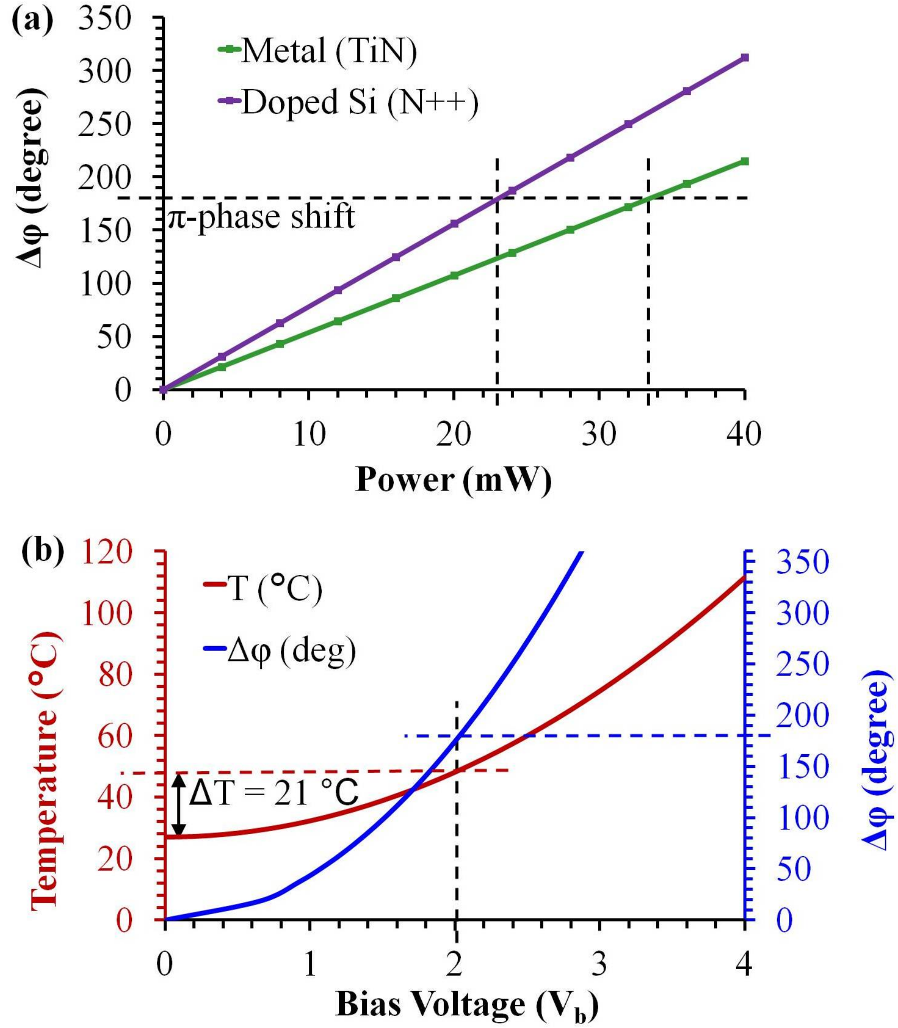

Figure 3.3 (a) Simulated phase-shift (degree) in metal (green) and doped (purple) phase shifters as a function of heater power consumption, (b) simulated temperature change (red) and phase-shift (blue) in the doped phase shifter as a function of heater bias voltage.

or carrier injection type phase-shifter [126]. As there is no p-n junction present across the waveguide core, the resistive heaters are practically immune to the optical losses associated with carrier injection heaters as no charged carrier overlaps with the optical mode inside the waveguide. Although p-n junctions offer faster phase-shift, they are long thus significantly increase footprint. On the other hand, metal heaters consume more heating power than resistive heaters to achieve the required phase-shift due to larger thermal heat capacity of most metals. The thermo-optic simulation is performed using the Heat solver of Lumerical's Device solution to compare the doped silicon heater with a TiN heater placed 2 μm above the waveguide surrounded by SiO_2 cladding. The TiN heater is 120 nm thick and has the same length as the doped silicon heater. The simulation results in Fig. 3.3(a) show that the metal heater consumes larger power (31.8 mW) to achieve π-phase shift in comparison to 21.5 mW for resistive heater. Moreover, resistive heaters are less susceptible to thermal crosstalk due to localized heating. From the fabrication point of view, TiN heaters need an additional step for mask design and lithography increasing the fabrication cost and complexity. Switching data from one output to the other is achieved at 2 V with a temperature increase of 21 °C from an initial room temperature of 27 °C at 0 V, as shown in Fig. 3.3(b). The total ohmic resistance of the phase shifter is estimated to be 170 Ω corresponding to a switching power consumption of 21.5 mW.

3.2 Fabrication and characterization

The switch was fabricated using a 248 nm deep ultra-violet (DUV) lithography by the Institute of Microelectronics (IME A*STAR), through a multi project wafer (MPW) service managed by Canadian Microelectronic Corporation (CMC) Microsystems. The fabricated chip was wire-bonded on a dual-in-line packaged gold carrier, shown in Fig. 3.4(a). A zoomed-in

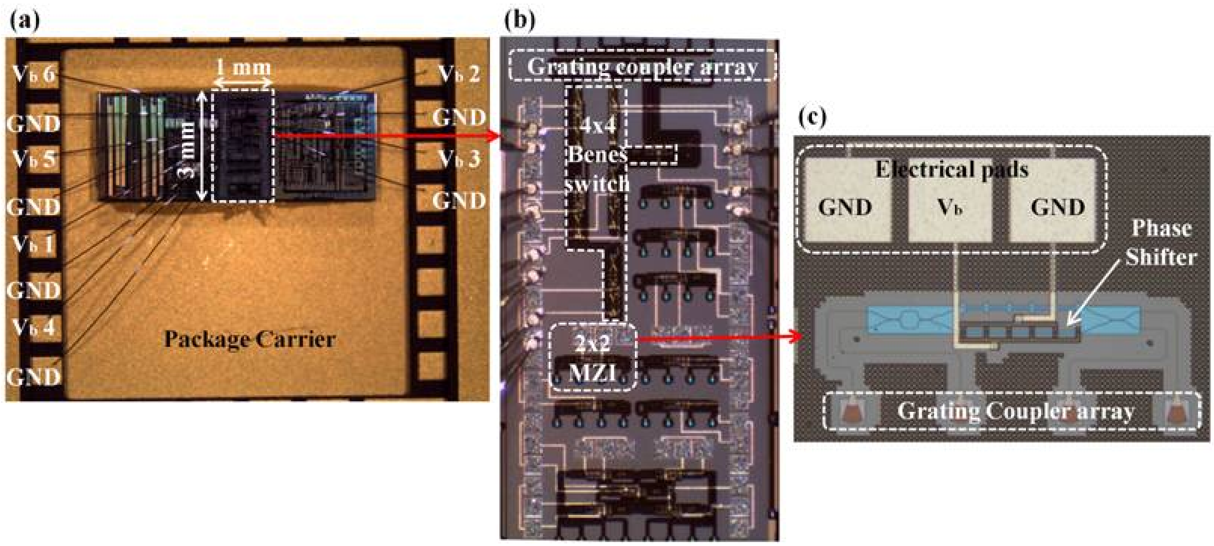

Figure 3.4 (a) Picture of the wire-bonded SOI die; (b) zoomed-in image of the switch design area in a MPW die; (c) zoomed-in of a 2×2 MZI elementary switch.

view of the 1 mm × 3 mm design area is shown in Fig. 3.4(b) and the 2×2 MZI building block in Fig. 3.4(c). The experimental test-bed is shown in Fig. 3.5. A tunable laser source ranging from 1325 nm to 1375 nm is set at an output optical power of 0 dBm (1 mW). For normalization purpose, a 12 dB fiber-to-fiber total insertion loss is measured on a short waveguide test structure with two vertical grating couplers.

The equivalent circuit diagram for the phase shifter is shown in Fig. 3.6(a). The phase shifter is segmented in to five sections such that each segment has two resistive paths in parallel. The voltage and ground connections are configured in a way that all resistors (R) are in parallel to each other. Fig. 3.6(b) is the image of the experimental measurement for the 2×2 MZI building block using two DC needle probes and a 8-fiber array. The measured total resistance of the phase shifter is 180 Ω, as shown in Fig. 3.6(c).

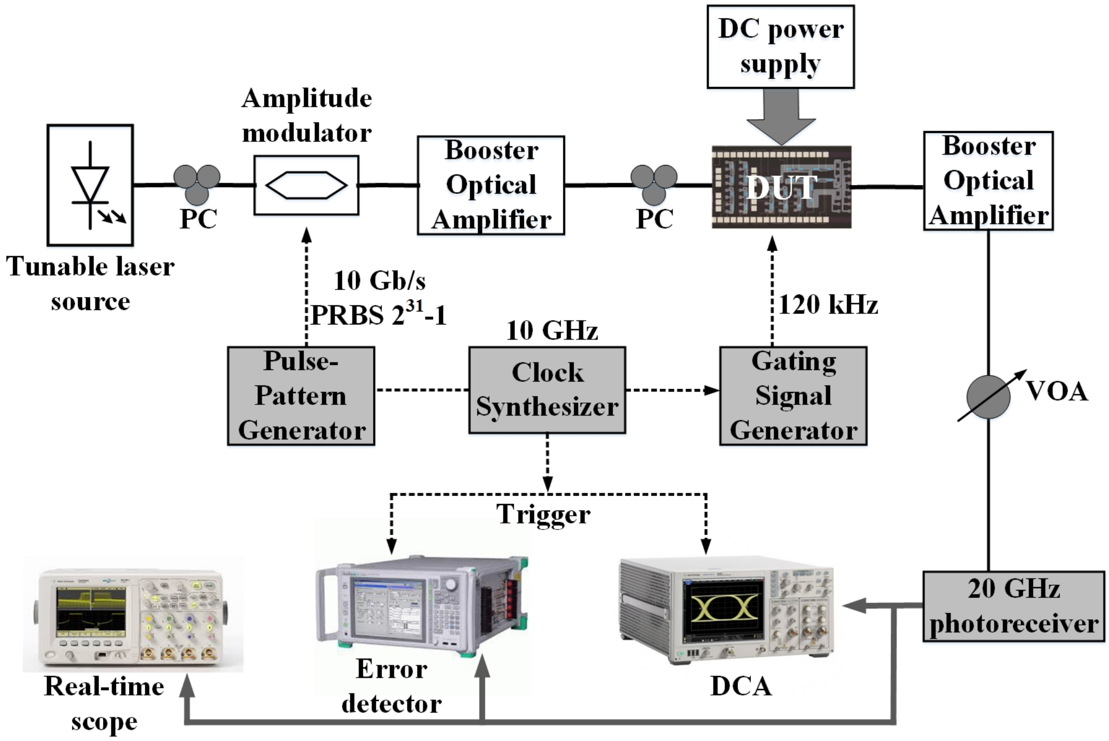

Figure 3.5 (a) Experimental test-bed for characterization where black solid and dotted lines show the optical and electrical connections, respectively. The gray lines show the electrical outputs detected by the photoreceiver.

3.2.1 Characterization of 2×2 MZI elementary switch

The 2×2 MZI elementary building block is initially characterized. The normalized transmission for the *In 1* input port as a function of heater power consumption is shown in Fig. 3.7(a) for the *bar* and the *crossbar* states. The switching ER at 1355 nm are 18.5 dB and 7.6 dB for the bar and the crossbar states, respectively. A switching voltage (V_π) of 1.2 V (P_π = 21 mW) at a bias voltage of 1 V (5 mW) switches between the ON (26 mW) and the OFF (5 mW) states, respectively. The normalized transmission as a function of wavelength from 1325 nm to 1375 nm are shown in Figs. 3.7(b) and (c) for the *In 1* and the *In 2* input ports,

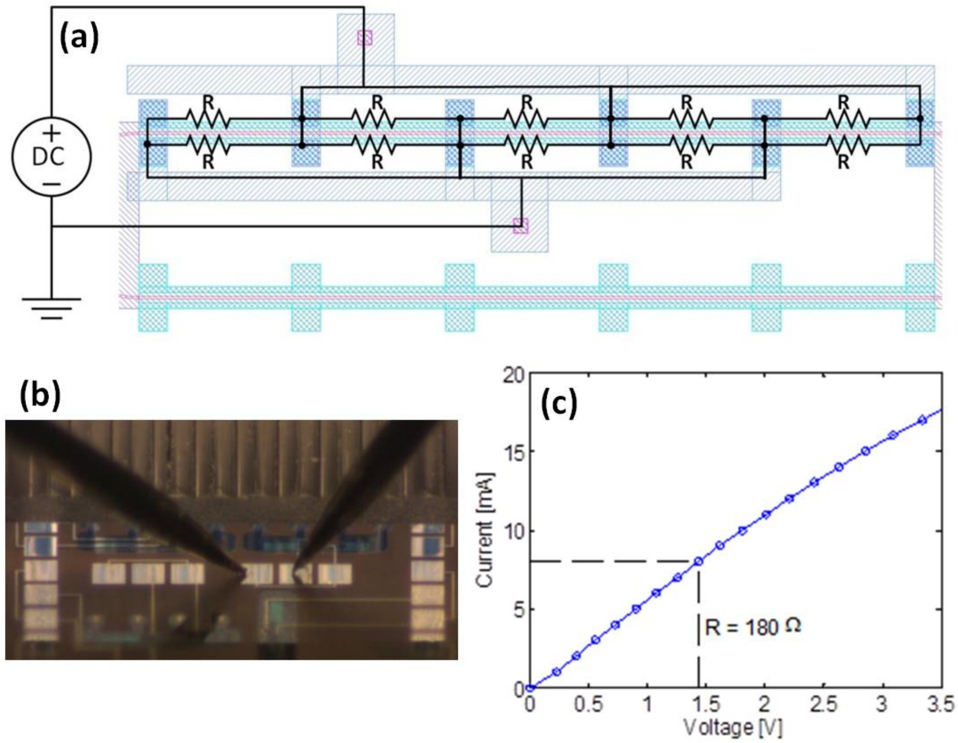

Figure 3.6 (a) Equivalent circuit diagram of the doped silicon phase shifter, shown in Fig. 3.1(b); (b) image of the DC characterization using two needle probes and a 8-fiber array; (c) measured I-V plot for the 135 μm long phase shifter.

respectively. The bar and crossbar state crosstalks are -16.5 dB and -14 dB, respectively, for the *In 1* input (Fig. 3.7(b)), and -15.0 dB and -13.5 dB, respectively, for the *In 2* input (Fig. 3.7(c)). The insertion loss of the 2×2 MZI at 1355 nm is approximately -2.5 dB for both *In 1* and *In 2* input ports. The imbalance in crosstalk is attributed to the fabrication sensitivity of the directional couplers. Due to the fabrication process variations in waveguides and directional couplers, the difference in optical path length between MZI arms shifts from the ideal value causing a leakage of optical power at the undesired output leading to large crosstalk. The crosstalk remains less than -13.5 dB in both *In 1* and *In 2* transmissions

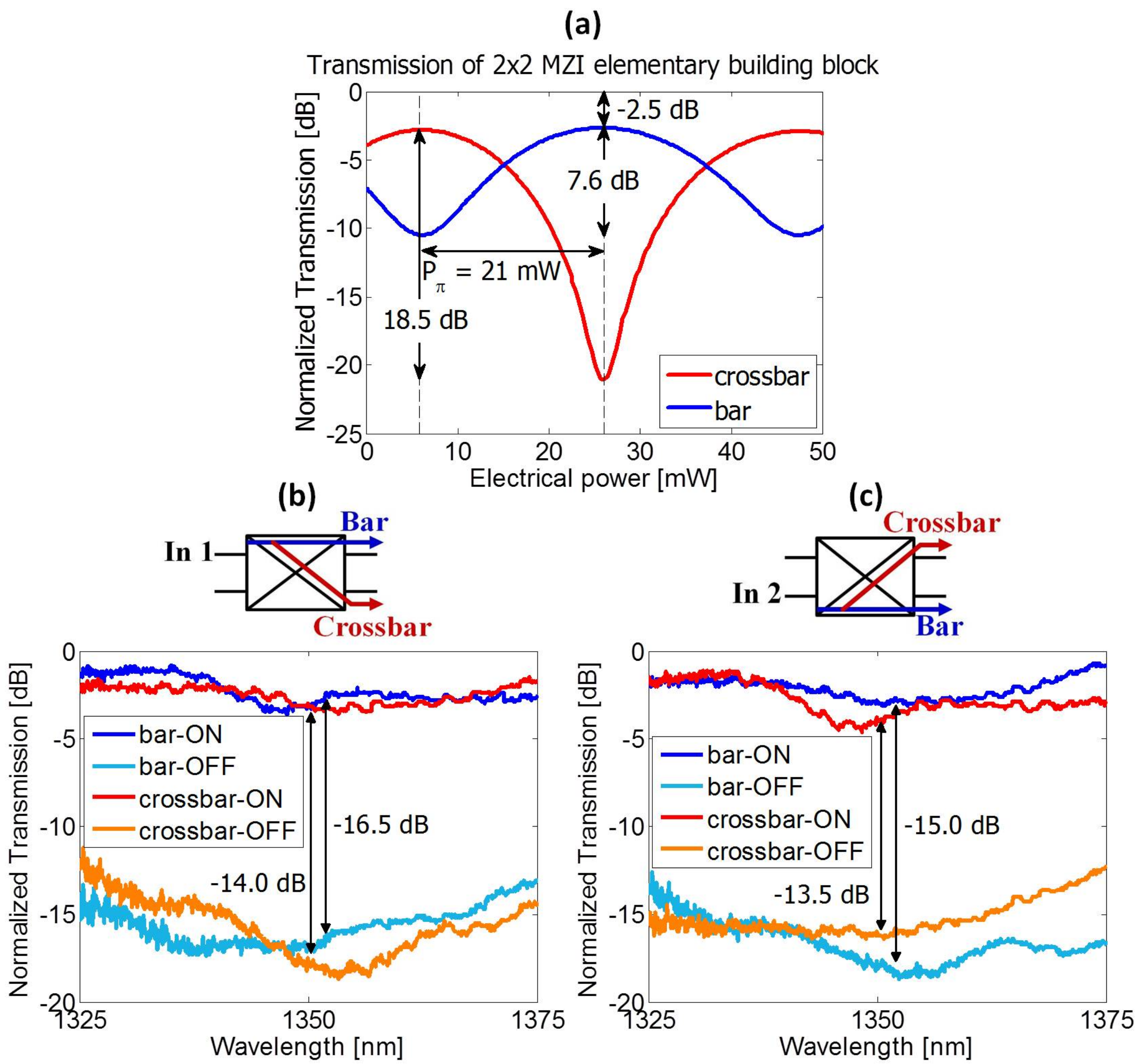

Figure 3.7 (a) Normalized optical transmission for *In1* input as a function of heater power consumption, (b) and (c) are the normalized optical transmissions of the 2×2 MZI building block when the CW optical input is in*In 1*, and *In 2*, respectively.

from 1325 nm to 1375 nm. Based on the characterization of 2×2 MZI elementary building block, and considering 3-stage routing for each I/O path, we estimate a -7.5 dB IL, 63 mW minimum power consumption, and -13 dB best case crosstalk for the 4×4 Beneš switch.

3.2.2 Characterization of 4×4 Beneš matrix switch

A subset of the 4×4 Beneš switch is characterized. The normalized optical transmissions in the *O2* output from all input ports are shown in Fig. 3.8 as a function of wavelength. The insertion losses at 1355 nm are -6.4 dB, -4.3 dB, -7.1 dB and -7.6 dB for *I1-O2*, *I2-O2*, *I3-O2* and *I4-O2* outputs, respectively. The crosstalk is less than -11 dB in all paths for a broad spectral range ($\sim$ 50 nm). The fiber-to-fiber insertion losses of 16 crosstalk optimized optical paths among 32 possible configurations are shown in Fig. 3.9, where all six MZIs of the 4×4 switch are optimally biased at 1355 nm. The IL ranges from -4.3 dB for *I2-O2* transmission up to -11.0 dB for *I1-O4* transmission. If all MZIs in the matrix are not optimally biased, their switching states cannot be properly predicted since the ON/OFF states of the idle MZIs are not precisely controlled. Consequently, a leakage of optical power occurs from the targeted input to non-targeted outputs resulting in power imbalance and crosstalk degradation [127]. As the switches consist of directional couplers, which are sensitive to process variation and thermal drift, the effective optical path length varies among the 2×2 elementary switches resulting in random phase difference between two MZI arms. Consequently, all MZI building blocks in the switch matrix must be biased in a known state to reduce this variation.

To assess the routed payload transmission performance, a 10 Gb/s NRZ PRBS31 signal is generated by a pulse pattern generator (PPG) as shown in Fig. 3.5. The optical signal is amplified by a booster optical amplifier (BOA), and a polarization controller (PC) maintains TE modes before coupling to the device under test (DUT). The input optical power to

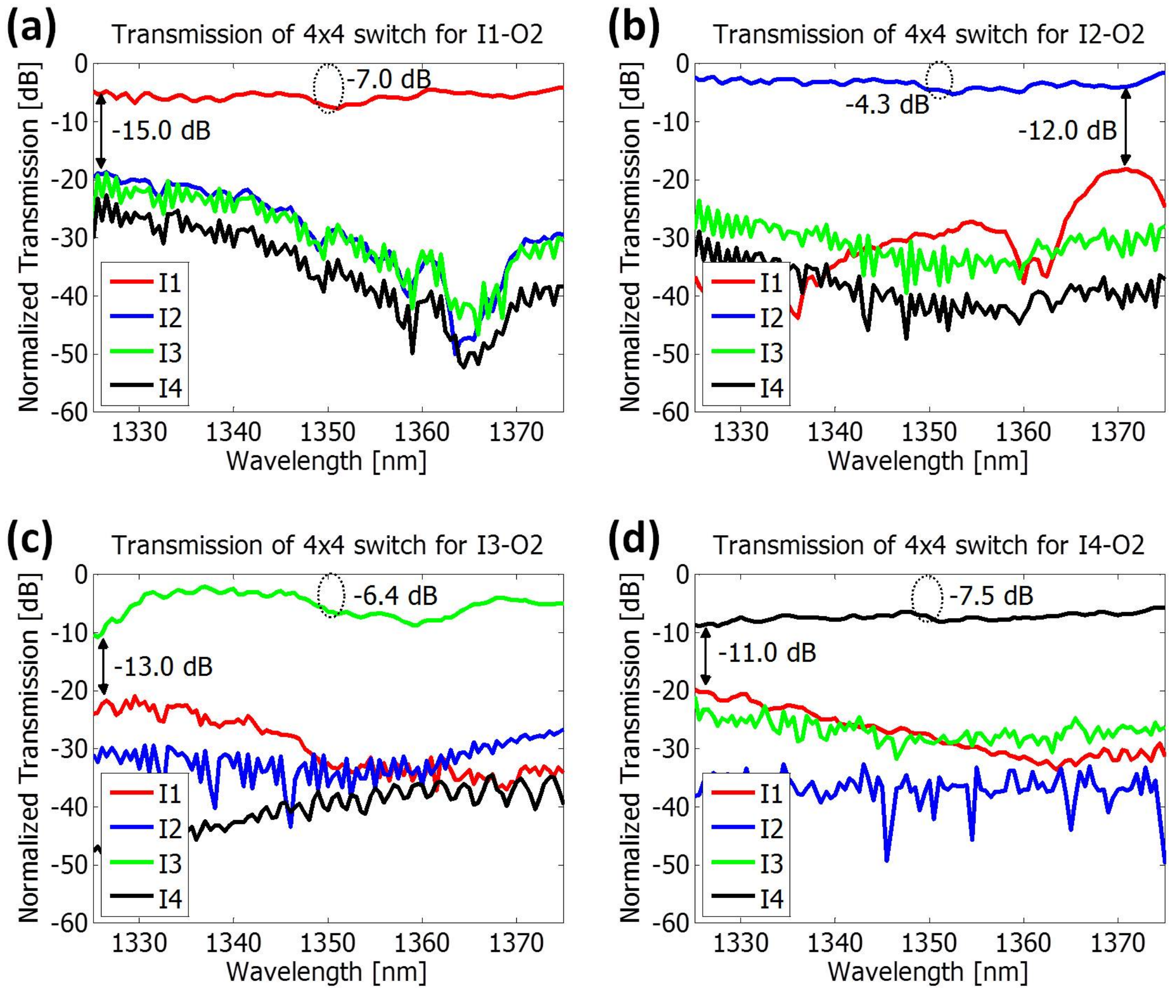

Figure 3.8 Normalized optical transmission of the 4×4 Beneš switch for the *O2* output port when the CW input is in (a) *In 1*, (b) *In 2*, (c) *In 3*, and (d) *In 4* input ports.

the DUT is 5 dBm. The optical signal at the output of the DUT is amplified by another BOA followed by a variable optical attenuator (VOA) before being detected by a 20 GHz photoreceiver. A clock synthesizer is used to provide the external clock to the PPG, the error detector, and the trigger to the digital communication analyzer (DCA) for recording the eye diagrams.

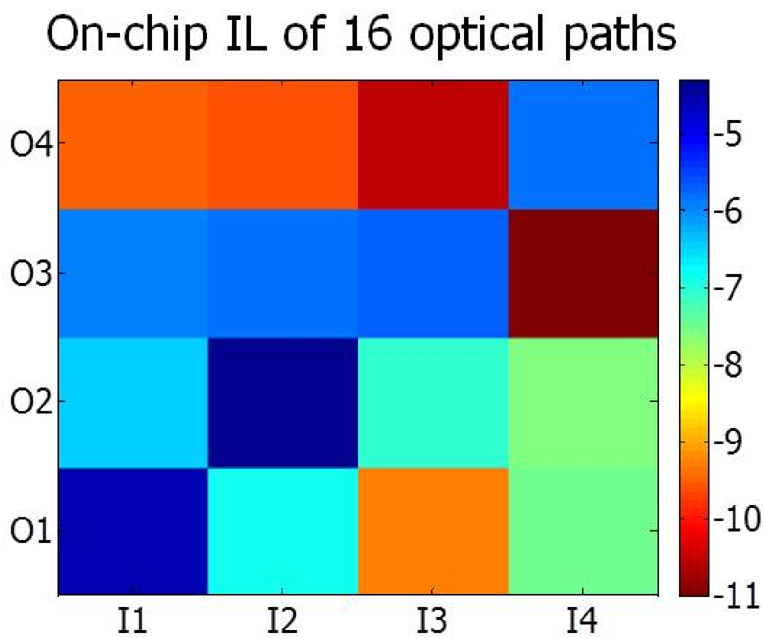

Figure 3.9 Measured on-chip IL at 1355 nm for all input ports to all output ports of the 4×4 Beneš switch.

The eye diagrams of 16 crosstalk optimized routing paths among 32 possible routing paths of the 4×4 switch are shown in Fig. 3.10. Some data paths exhibit more noise level than others due to larger insertion loss and, consequently, more ASE noise from the BOA requiring larger gain. Note that the effective optical path length varies among the MZI building blocks due to the fabrication process variation and thermal drift resulting in random phase difference between two MZI arms. Consequently, all MZI building blocks in the switch matrix are biased in a known state for any given routing path. The electrical signal-to-noise ratio (SNR) for different optical I/O channels at a BER of 10^{-12} is measured in all channels. The SNR ranges from 6.8 to 15.4. The BER power penalty is measured at output *O2* for all four inputs from the extrapolated data points. For the back-to-back (B2B) bit-error-rate

(BER) measurement, the DUT is replaced by an optical attenuator with the same loss as the routing path with the lowest loss, which is *I2-O2* (-14 dB). Fig. 3.11 shows the BER (log scale) as a function of average received optical power at 1355 nm. All channels exhibit error-free data transmission with a BER of 10^{-12}. The power penalties vary for different routing paths and are 0.8 dB, 0.1 dB, 1.9 dB and 1.6 dB for routing paths *I1-O2*, *I2-O2*, *I3-O2*, and *I4-O2*, respectively.

Although the optical responses of the 4×4 Beneš switch remain flat over 50 nm wavelength range in O-band, the small 3-dB bandwidth of the off-chip $LiNbO_3$ modulator (12 GHz or 0.96 nm) keeps it stable within a small wavelength range at room temperature (23 °C). This limits the optical bandwidth by forcing the switching experiments in a smaller wavelength span. An on-chip wavelength- and bandwidth-tunable micro-ring modulator can be used for better wavelength control to exploit the broadband nature of the switch [128].

To characterize the dynamic switching performance, an electrical square wave of 120 kHz with fall and rise times of 16 ns is applied as the gating signal at 2.1 V bias. The switching of optical packets routed through the 4×4 switch is performed by applying the square wave gating signal to MZI-3 with the optical input at *I1* and the optical output switching between outputs *O1* and *O2*. The optical path from *I1* to *O1*/*O2* is optimized by biasing all idle MZIs in their crossbar states to mitigate crosstalk [125]. Fig. 3.12(a) is the normalized transmission of all outputs for *I1* input for MZI-3 switching. The switching ER in *O1* and in *O2* are 7 dB and 20 dB, respectively. The IL of the routing path is -6.4 dB at 1355 nm. The crosstalk in the bar (*O1*) and crossbar (*O2*) states are -22 dB and -5.6 dB, respectively at 2.1 V and

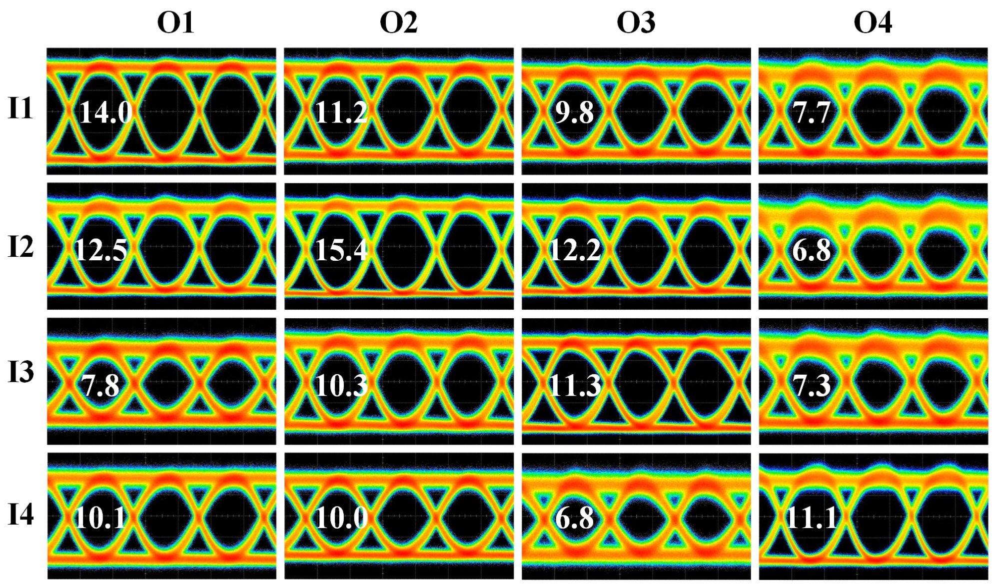

Figure 3.10 Eye diagrams with corresponding electrical SNRs in all output ports of the 4×4 Beneš switch for 10 Gb/s NRZ PRBS-31 data transmission. The input optical power is fixed at 5 dBm at 1355 nm

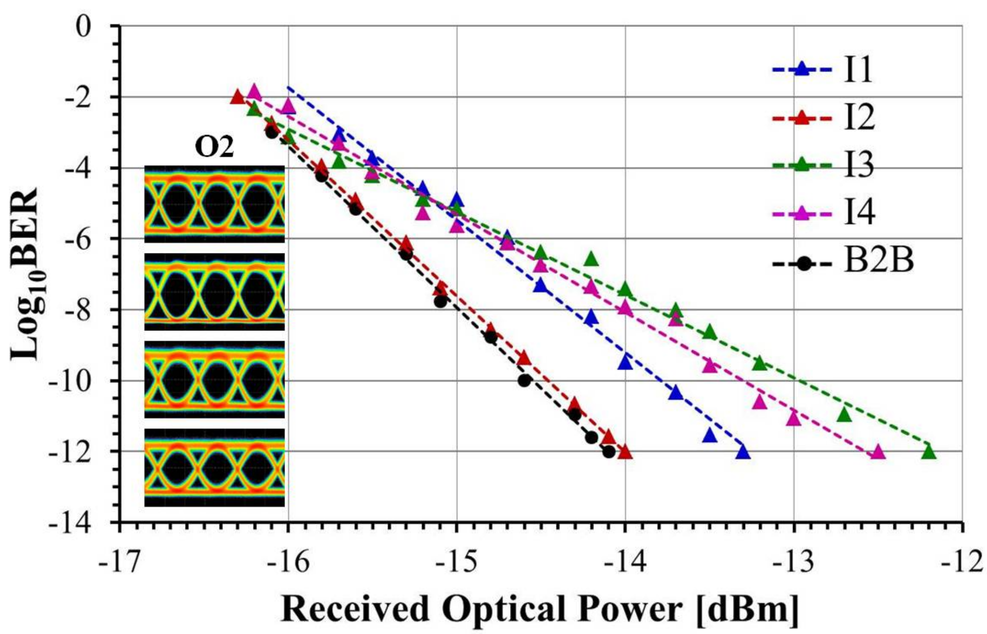

Figure 3.11 Measured BER at *O2* output port as a function of average received optical power for all four input ports. The B2B configuration is set for the lowest IL path i.e., *I2*-*O2* transmission.

0.9 V, respectively. The static switching response of MZI-3 is shown in Fig. 3.12(b) for *I1-O2* transmission. The measured rise and fall times (10 % to 90 %) of the 2×2 switch are 1.6 μs and 2.0 μs, respectively. Fig. 3.12(c) shows the dynamic switching performance of the 4×4 switch. The rise and fall times for *O1* are 1.8 μs and 2.4 μs, respectively, and for *O2* are 2.2 μs and 1.9 μs, respectively. Due to the high bar state crosstalk (-7.6 dB) of MZI-3, the optical power leakage from MZI-1 via MZI-5 may couple back to MZI-3's *O2* port increasing the crosstalk while the payload is transmitted through *O1.* This high level of crosstalk of -5.6 dB at 1.0 V in Fig. 3.12(a) is a concern for a large port-count matrix switch and when multiple channels are operating at the same time as it may degrade signal integrity.

3.3 Discussion

The efficient switching and low-loss advantages offered by the designed switch matrix lead to scalability potential for the higher radix switch implementation. From the measured power consumptions of the 2×2 MZI building blocks and taking into account that all MZIs are biased into a known state mitigating crosstalk, the maximum total power consumption for a given N×N Beneš switch matrix can be estimated. In Fig. 3.13, the maximum power consumption (P_{max}) for the 4×4 switch is estimated to be 154.5 mW following the equation: $P_{max} = (\frac{P_{total}}{N_{path}}) \times S$, where P_{total} is the power consumption for a given routing path, N_{path} is the number of switch in a routing path, and S is the total number of switch in the given N×N switch matrix. It is noteworthy that for a power consumption optimized switch setting, all

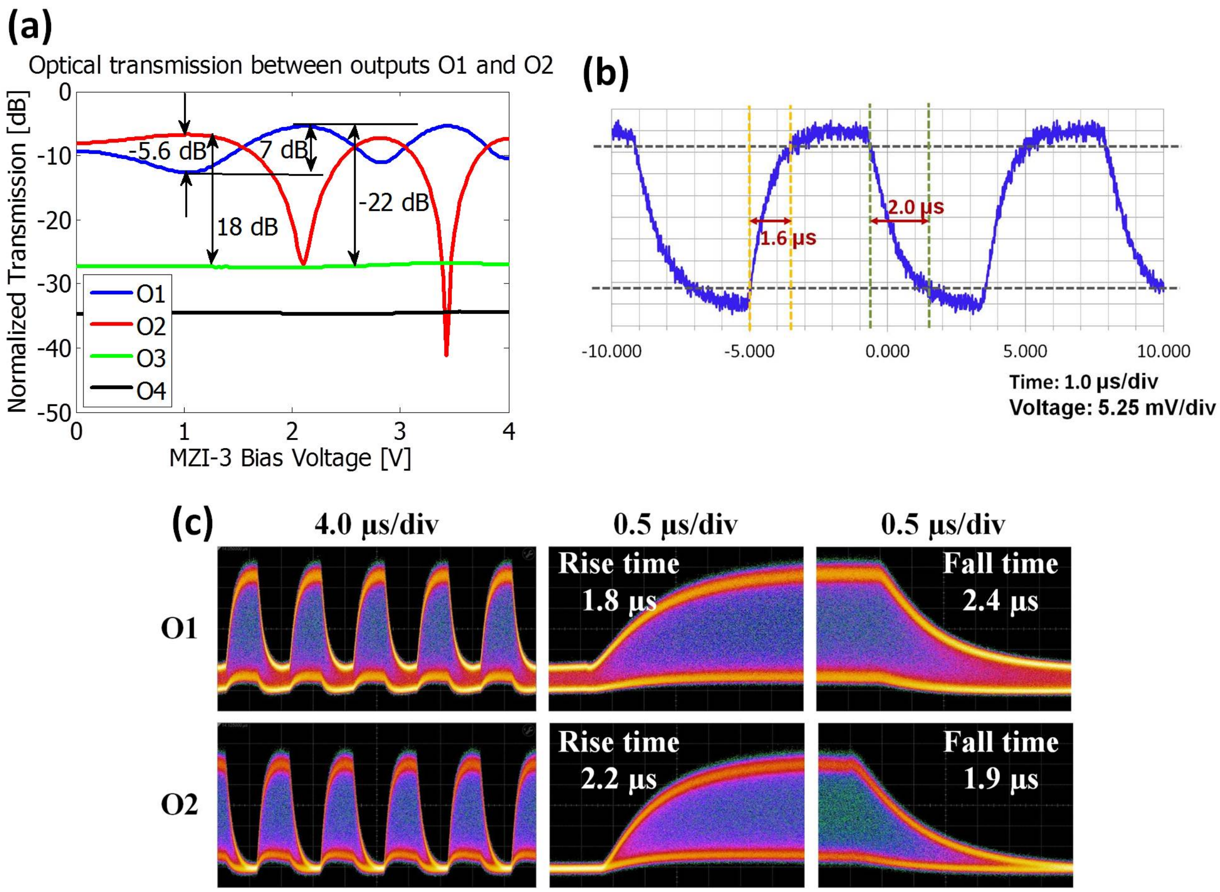

Figure 3.12 (a) Normalized optical transmission in all four output ports as a function of MZI-3 bias voltage for the *I2* input; (b) measured static switching response for *I2*-*O2* transmission; and (c) dynamic switching response between *O1* and *O2* output ports corresponding to the transmission shown in (a).

idle MZIs are expected to be tuned at their lowest power bias points. However for greater crosstalk immunity, idle MZIs may be biased at higher voltages. P_{max} is estimated here for the latter case.

The footprint area of the 4×4 switch is estimated to be $0.1536\,\mathrm{mm}^2$, calculated from the area of a 2×2 building block ($0.0112\,\mathrm{mm}^2$) and the area of two $100\,\mu$m pitched $80\,\mu\mathrm{m}^2$ electrical pads ($0.0144\,\mathrm{mm}^2$) for the signal and ground connections required to drive a single

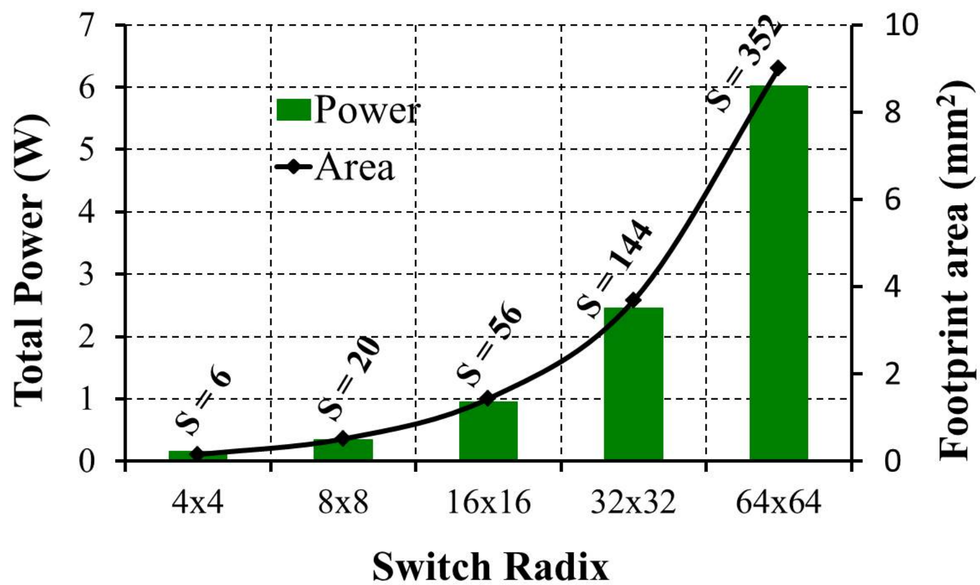

Figure 3.13 Estimated total power of N×N O-band SOI thermo-optic Beneš switches with corresponding footprint areas.

2×2 switch. As the switch radix scales up, the footprint area and the maximum total power consumption increases exponentially. However, the average power consumption per switch for a crosstalk optimized channel ($\frac{P_{total}}{N_{path}}$) remains constant at 25.75 mW. Hence, optimal tuning of MZI bias voltages for efficient performance of higher radix thermo-optic matrix switches can be ensured. The number of switches also increases exponentially following the equation: $S = Nlog_2N - \frac{N}{2}$. Hence, an exponential rise of the insertion loss is expected in larger matrices. Considering -2.5 dB IL per MZI from Figs. 3.7(a), the total IL is estimated to be -15 dB in a 4×4 matrix which can be detrimental for the transmission of optical data packets in larger matrices. However, the worst case IL for a crosstalk optimized channel is -11 dB (Fig. 3.9) in the 4×4 switch ($S = 6$) with an estimated -1.8 dB IL per MZI.

The IL can be reduced by on-chip gain integration using flip-chip bonded semiconductor optical amplifiers (SOAs) as in [129], where the fiber-to-chip coupling loss for a 4×4 strictly non-blocking Beneš switch is compensated with a -15 dB crosstalk over the full C-band. However, a large power consumption of 620 mW and a large footprint area of 8.2 mm × 2.2 mm are required to achieve strictly non-blocking switching (12 switching elements). The integration of the SOAs by flip-chip bonding, and the electronic drivers by wire-bonding impose additional challenges of optical alignment, cost and complexities of post-processing, and packaging. The wavelength dependence and fabrication sensitivity of the passive optical components, such as directional coupler, can be reduced by wavelength tunable directional couplers using resistive micro-heater as in the resistive phase shifter. However, this additional tuning power will eventually increase the overall power consumption. A better alternative is to use MMI couplers for more fabrication tolerance leading to higher ER and lower crosstalk [130]. The switch performance affected by the fabrication sensitivity, *i.e.*, crosstalk and extinction ratio, can be adjusted and optimized by tuning the DC splitting ratio and MZI bias voltages.

3.4 Summary

In this chapter, we presented a fully functional thermo-optically tuned 4×4 Beneš switch matrix in O-band for optical interconnects in data centers. The 4×4 matrix consists of compact and broadband 2×2 MZI building blocks enabling broadband operation over a 45 nm wavelength range with 21 mW switching power. Rise and fall times range from 1.8 μs to 2.4 μs in the 4×4 Beneš switch while switching between two output ports. The switch performance is optimized by bias tuning the MZIs at fixed known states. The IL of the 4×4 switch ranges from -4.6 dB to -11.0 dB among the 16 optimized I/O channels. The characterization of a subset of the switch's 32 possible I/O combination exhibits -11.0 dB worst case crosstalk at 1355 nm. Open eye in all output ports confirms error-free data transmission at 10^{-12} BER with less than 1.9 dB BER power penalty with respect to the B2B configuration. Distortion-free transmission of high-speed optical data packet through dynamic switching demonstrates the switch's potentials for WDM data communication.

Chapter 4

Reconfigurable multimode (de)multiplexer/switch

In this chapter, we present a novel silicon photonics mode-division-multiplexing device, which can (de)multiplex and switch on-chip mixed mode signals for simultaneous transmission and switching of multiple high-speed optical data. The reconfigurable and scalable (de)multiplexer/switch (RMDS) is used as the building block in a mode demultiplexer, and also in a mode switch. The proof-of-concept device can concurrently transmit and switch high speed optical data over the fundamental and the first order quasi-transverse electric (quasi-TE) modes. The quasi-TE0 and quasi-TE1 modes are launched using only one C-band laser (from 1500 nm to 1600 nm) improving the energy efficiency. Parallel data transmission is confirmed by the simultaneous transmission of two individual non-return-to-zero (NRZ) data packets at 10 Gb/s. For mode demultiplexing, a mode combiner stage is needed after the RMDS to retrieve the input TE0 and TE1 modes. This mode combiner is replaced by a MMI-based mode switch MMI in an on-chip mode-selecting switch (MSS) comprising of cascaded MMI couplers and thermo-optic phase shifters. The mode decomposer MMI, or the RMDS, is the most critical component providing the required modal separation and channel crosstalk. As the propagation and manipulation of different eigenmodes in a waveguide is critically related to the dimension of the photonic components, which makes it difficult to manipulate different mode orders in the same structure, the quasi-TE1 mode is decomposed to its fundamental (^{0}TE1) components before processing. Distortion free data transmission is demonstrated for $2{\times}10$ Gb/s aggregated bandwidth with a bit-error-rate (BER) of 10^{-12} and <2.8 dB power penalty while simultaneously transmitting two data channels. The results presented in this chapter are published in [69] and [70].

4.1 Design and working principle

The 3D schematic of the proposed RMDS is shown in Fig. 4.1. The RMDS is a $1{\times}3$ MMI coupler consisting of a multimode input port (port1) and three single-mode output ports (port2, port3, and port4). For the individual-mode transmission, either the fundamental (quasi-TE0) or the first-order (quasi-TE1) mode is launched at port1. The input TE0 mode is mapped onto port3 as ^{0}TE0 with a smaller mode-field diameter (MFD). The input TE1 mode is decomposed into two fundamental mode components of equal amplitudes but with opposite phases. These mode components are mapped to port2 and port4 as ^{0}TE1. For the multimode transmission, both the TE0 and the TE1 modes are launched simultaneously at port1 and separated at the output ports into their fundamental mode components. The ^{0}TE0 component from TE0 mode is mapped to port3, and the ^{0}TE1 components from TE1 mode are mapped to port2 and port4.

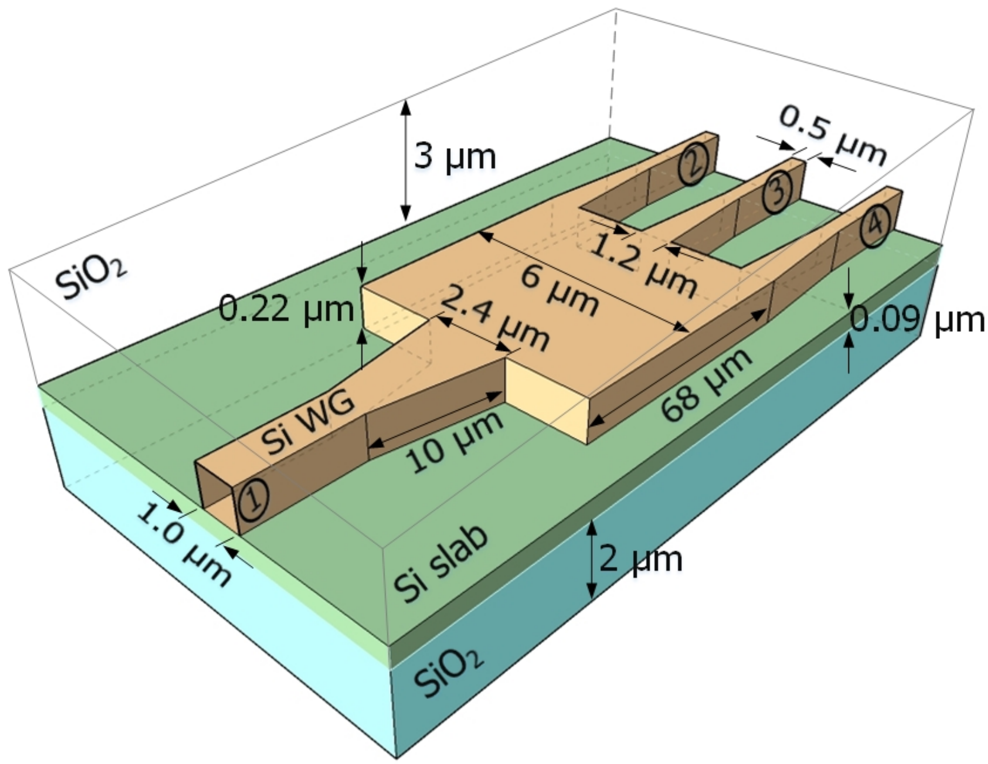

Figure 4.1 Schematic of the RMDS in 3D view with input port1 and outputs port2, port3, and port4.

A 220 nm thick SOI waveguide core with a 90 nm thick silicon slab is used for guiding and propagating the optical signal. The waveguides are buried in between a 2 μm thick buried oxide layer and a 3 μm thick top oxide cladding layer. The cross-section of the waveguide is shown in Fig. 4.2(a). A commercial simulation tool from Lumerical is used for modeling the effective refractive indices of the first four quasi-TE modes (TE0, TE1, TE2,

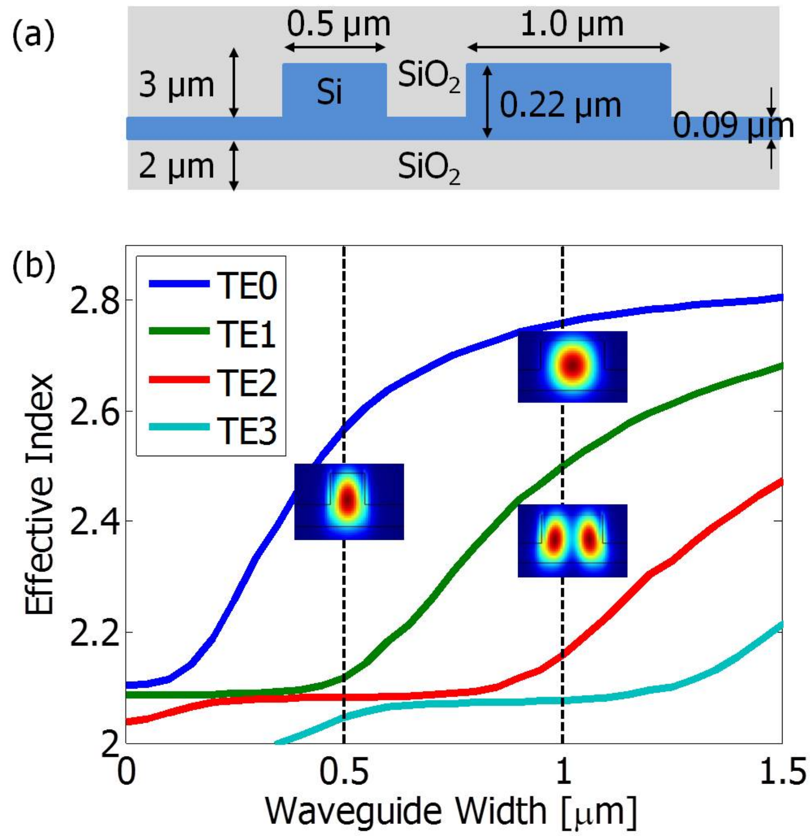

Figure 4.2 (a) Cross section of the waveguide showing the dimensions for single-mode (0.5 μm) and multimode (1.0 μm) propagation (figure not drawn to scale), (b) simulated effective refractive indices for the first four TE modes.

and TE3) as a function of waveguide widths, as shown in Fig. 4.2(b). The cutoff widths of the access waveguides for the single-mode (TE0) and the multimode (TE0+TE1) transmissions are 0.5 μm and 0.8 μm, respectively. The effective refractive index is less sensitive to the waveguide width variation for a wider waveguide resulting in greater robustness against process variation. For this reason, the width of the multimode waveguide is optimized to be 1.0 μm.

In the MZI based devices, a small imbalance in the power coupling ratios between the

MMI's output ports contributes to large degradation in the crosstalk. Wider waveguide widths make MMI couplers more viable against fabrication process variations compared to adiabatic directional couplers. Hence, MMI couplers exhibit lower coupling power imbalance leading to higher extinction ratio (>25 dB) and lower crosstalk [62]. In addition, the lengths of adiabatic couplers increase with the number of modes, which challenges the scalability to greater number of modes.

For a fixed MMI width of 6 μm, the estimated beat length, L_π, is calculated for the first two lowest order modes numerically using the following equation [131]

$$L_\pi = \frac{\pi}{\beta_0 - \beta_1} = \frac{4n_{eff}{W^2}_m}{3\lambda_0} \tag{4.1}$$

where β_0 and β_1 are the propagation constants of the fundamental and the first-order modes ($\beta = 2\pi n_{eff}/\lambda_0$), n_{eff} is the effective refractive index, W_m is the MMI width, and λ_0 is the design wavelength. The beat length is calculated to be 90 μm at λ_0=1550 nm. The input/output locations of the MMI coupler are also calculated by using the analytical equations in [63]. Like a mode filter with 100 % mode conversion efficiency, the RMDS maps the symmetric (TE0) and the asymmetric (TE1) modes to the different output waveguides. For the symmetric mode, we applied the theory of symmetric interference, where the input that is launched at the center of the MMI forms the M-th N-fold image at a distance, L_{MMI}, defined by [71].

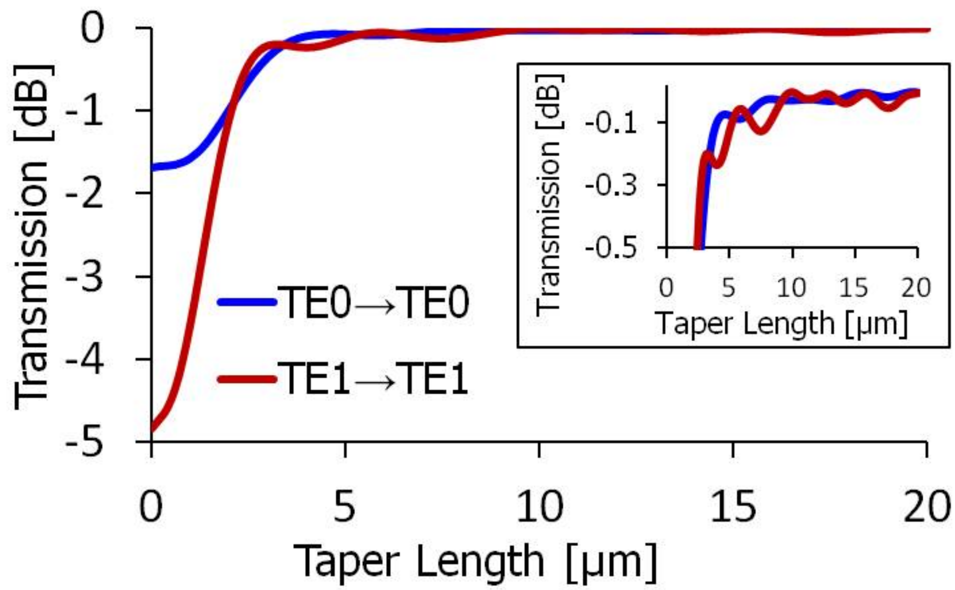

Figure 4.3 Simulated optical transmission of TE0 and TE1 modes in the input taper of the RMDS as a function of taper length. The inset is the zoomed-in of the peak optical powers.

$$Ł_{MMI} = \frac{M}{4N}(3L_{\pi}) \tag{4.2}$$

The principle of general interference is applied for the asymmetric mode which satisfies the length, L_{MMI}, as long as the single-mode input waveguide is not positioned at the center of the MMI [72]. Considering the wider multimode input waveguide (1.0 μm wide) as two single mode waveguides (0.5 μm wide) placed next to each other, this condition is satisfied. To obtain the first ($M = 1$) single image ($N = 1$), the MMI length (L_{MMI}) becomes $\frac{3}{4}L_{\pi}$.

Optical reflection and scattering losses at the input and output ends are minimized by adding 10 μm long tapers, which allow more than 98 % transmissions of both TE0 and TE1 modes satisfying adiabatic condition [132]. The normalized transmission of the TE0 and the TE1 modes at the input taper (port1) of the RMDS is shown in Fig. 4.3, confirming adiabatic transmission of both modes. The inset is the zoomed-in of the peak transmission. The length of the RMDS is optimized by the fully vectorial and bi-directional eigenmode expansion model. The simulated transmission as a function of MMI length is shown in Fig. 4.4 for a 0 dBm Gaussian beam optical input at 1550 nm.

There are three scenarios when the input optical signal is launched at port1 of the RMDS:

1. Single-mode (TE0) transmission: maximum power in port3 with minimum power in both port2 and port4.

2. Single-mode (TE1) transmission: maximum power in both port2 and port4 with minimum power in port3.

3. Multimode (TE0+TE1) transmission: maximum power in all of port2, port3, and port4.

From Fig. 4.4, these conditions are satisfied for an RMDS length of 68 μm when the TE0-to-port3 transmission, and both TE1-to-port2 and TE1-to-port4 transmissions are maximum, and the TE0-to-port4 transmission is minimum. It is observed in Fig. 4.4 that TE0 transmissions at port2 and port4 are sensitive to MMI length. Although MMI′s are more tolerant to fabrication process variation than single mode (0.5 μm wide) waveguides, a small change in the MMI dimension can result in large crosstalk between port3 and port2 or between port3 and port4. As $\pm$10 nm change in dimension can be expected from the fabrication

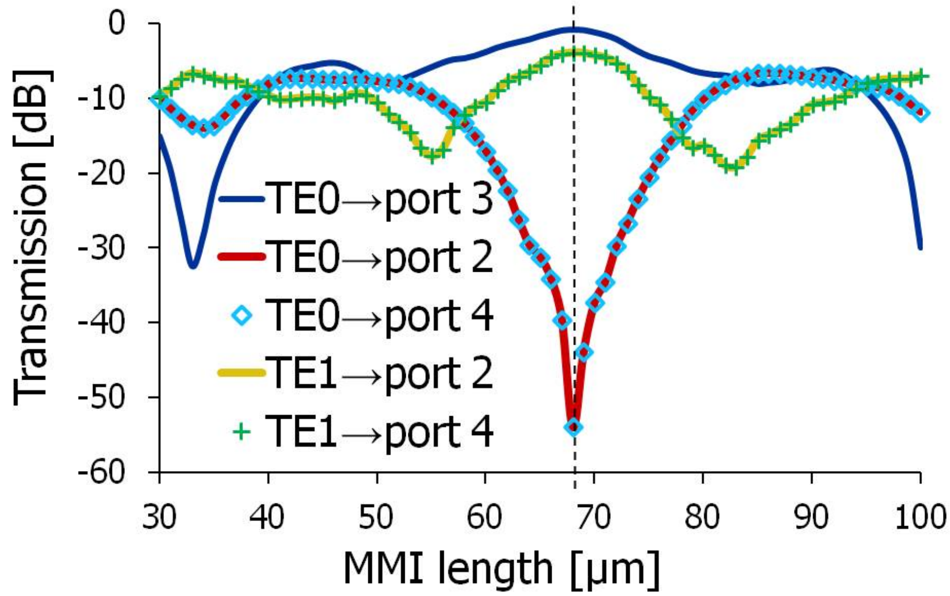

Figure 4.4 Simulated optical power of TE0 and TE1 mode components as a function of the length of the RMDS at 1550 nm wavelength. The TE1→port3 transmission exhibits negligible transmittance (<-250.0 dB) IL hence not shown.

error [122], the crosstalk between port3 and port2 for TE0 transmission is estimated within ±20 nm range, and shown in Fig. 4.5 as a function of RMDS length and width variations. The initial length and width are 68 μm and 6 μm, respectively, representing 0 μm variation. Negligible change in crosstalk is observed with length variation. However, crosstalk increases from -39.4 dB to -31.7 dB with the width variation, although remains <-31 dB within this range. The crosstalk decreases when the width variation leads to smaller waveguide core. As a narrower MMI can accommodate less number of modes than a wider MMI, the inter-modal cross-coupling between overlapping modes is less likely to occur in a narrower MMI resulting in lower crosstalk.

The simulated scattering matrix (S-matrix) including all possible input/output combina-

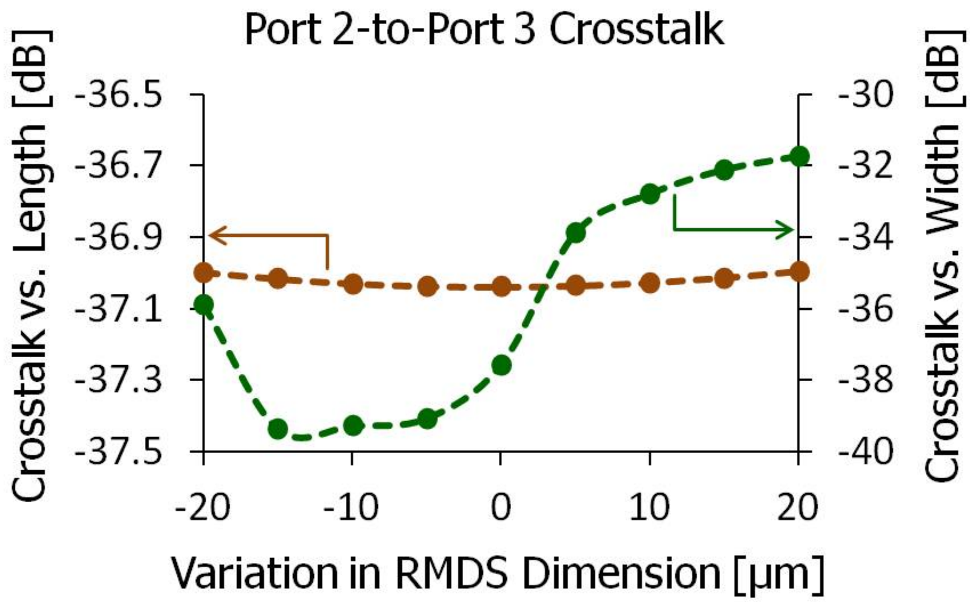

Figure 4.5 Simulated crosstalk between port2 and port3 as a function of the variation of RMDS dimensions (length and width) for TE0 transmission. The initial length and width representing 0 μm variation are 68 μm and 6 μm, respectively.

tions of all mode components for a 68 μm long RMDS is shown in Fig. 4.6 when a multimode (TE0+TE1) optical signal of 0 dBm (1 mW) input power is launched at port1. The power leakage at port2 and port4 from the TE0 input is comparatively higher (-53 dBm) than the leakage at port3 from the TE1 input (-190 dBm). Although the simulation accounts for multiple reflection events, it does not take into account the scattering losses from waveguide side-wall roughness and uneven waveguide surfaces leading to these unrealistic values of leakage power. However, these simulation results remain valuable in providing information on relative crosstalk among the output ports. As the beam divergence of a propagating Gaussian beam is inversely proportional to the beam radius at its launching point [133], the

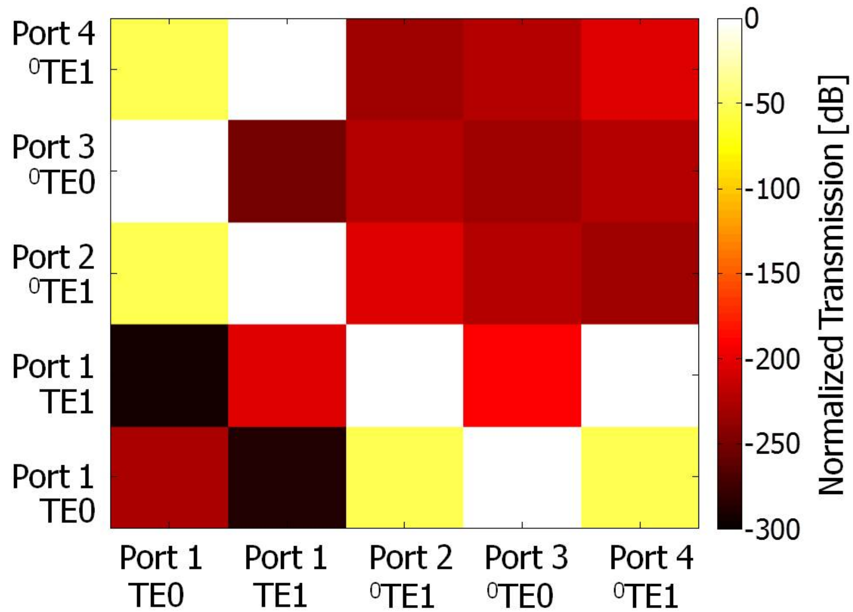

Figure 4.6 Simulated optical S-matrix of the 68 μm long RMDS for the transmission of TE0 and TE1 mode components.

higher leakage at port2 and port4 may result from the higher MFD of the TE0 mode than that of TE1 mode at port3. Very small back reflection (10^{-2} dB) is expected at each port leading to small optical return loss. Note that higher order quasi-TE (e.g., TE2, TE3, etc.) and quasi-TM (e.g., TM0, TM1, etc.) modes are not considered in the simulation, assuming little inter-modal power leakage from these modes. In reality, these unexpected modes affect the net transmission at each output port. This will be discussed in the next section. As the RMDS is demonstrated as a proof-of-concept device using TE0 and TE1 modes, we will limit our discussion to TE0 and TE1 modes.

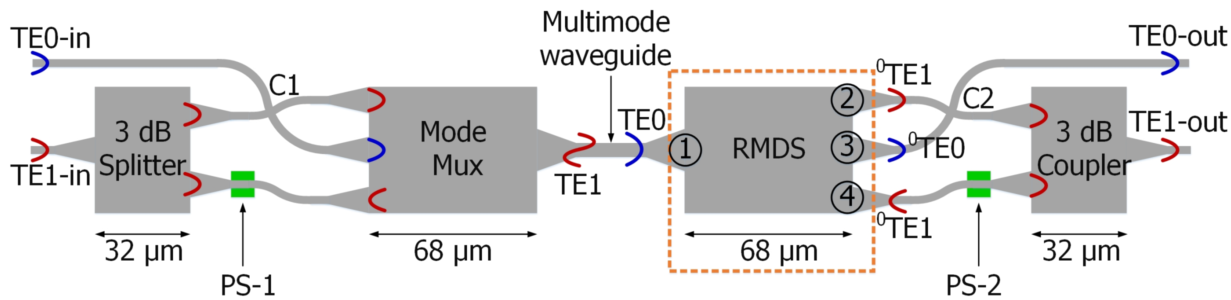

Figure 4.7 Schematic of the mode demultiplexer. The electric fields and the optical transmissions of the RMDS delimited by the orange box, is shown in Fig. 4.8.

4.2 Mode demultiplexing

The mode demultiplexer (MD) requires four cascaded MMIs (a 3-dB splitter, a mode multiplexer, the RMDS, and a 3-dB coupler), and two resistive heater phase shifters (PS-1 and PS-2), as shown in Fig. 4.7. The phase shifters are used for tuning the relative phases of the ^{0}TE1 components for multiplexing and demultiplexing the TE1 mode to and from the multimode waveguide, respectively. Note that the transmission of the TE0 mode does not require a phase-shift. Each phase shifter is 250 μm long consisting of highly N-doped (N++) silicon slab placed 700 nm away from the lightly doped waveguide core. The detailed design of the phase shifter is discussed in chapter 3.

4.2.1 Design and working principle

As a mode multiplexer and a mode demultiplexer are identical devices with opposite input/output direction, a single bi-directional component can be designed for both multiplexing and demultiplexing operations. The simulated electrical fields in the RMDS are shown in Figs. 4.8(a), (c) and (e) for the individual-mode transmission of TE0 mode, individual-mode transmission of TE1 mode, and dual-mode transmission (TE0+TE1) mode, respectively. The net optical transmissions from 1500 nm to 1600 nm corresponding to each mode are shown in Figs. 8(b), (d) and (f), respectively.

For the individual-mode transmission, either the *TE0-in* or the *TE1-in* input ports (Fig. 4.7) are used for the transmission of the TE0 mode or the TE1 mode, respectively. For the TE0 transmission, the input light is coupled to the middle input port of the mode multiplexer and mapped to its multimode output port with a larger MFD. The RMDS maps this beam to its port3 output port as ^{0}TE0, shown in Fig. 8(a), without any decomposition to retrieve the original optical signal at the TE0 out output port. A -29.0 dB crosstalk is estimated at 1550 nm with -1.5 dB insertion loss (IL), as shown in Fig. 4.8(b). This crosstalk is higher than that of Figs. 4.4 and 4.6, where only TE0 and TE1 modes are considered for the length optimization. However, in reality, higher order quasi-TE and quasi-TM modes may cause power leakage and inter-mode cross-coupling resulting in crosstalk degradation.

For the TE1 transmission (*TE1-in*), the 3-dB splitter separates the optical input into two fundamental mode components with the same phase as the original input signal, corresponding to a phase-shift of $\Delta\phi = 0$. As the two mode components of a TE1 mode are out-of-phase by π rad, a phase-shift of $\Delta\phi = \pi$ is applied to one of the mode components by thermo-optically tuning the PS-1 phase shifter. These two π-phase-shifted components are coupled to the upper and the lower input ports of the mode multiplexer and mapped as TE1

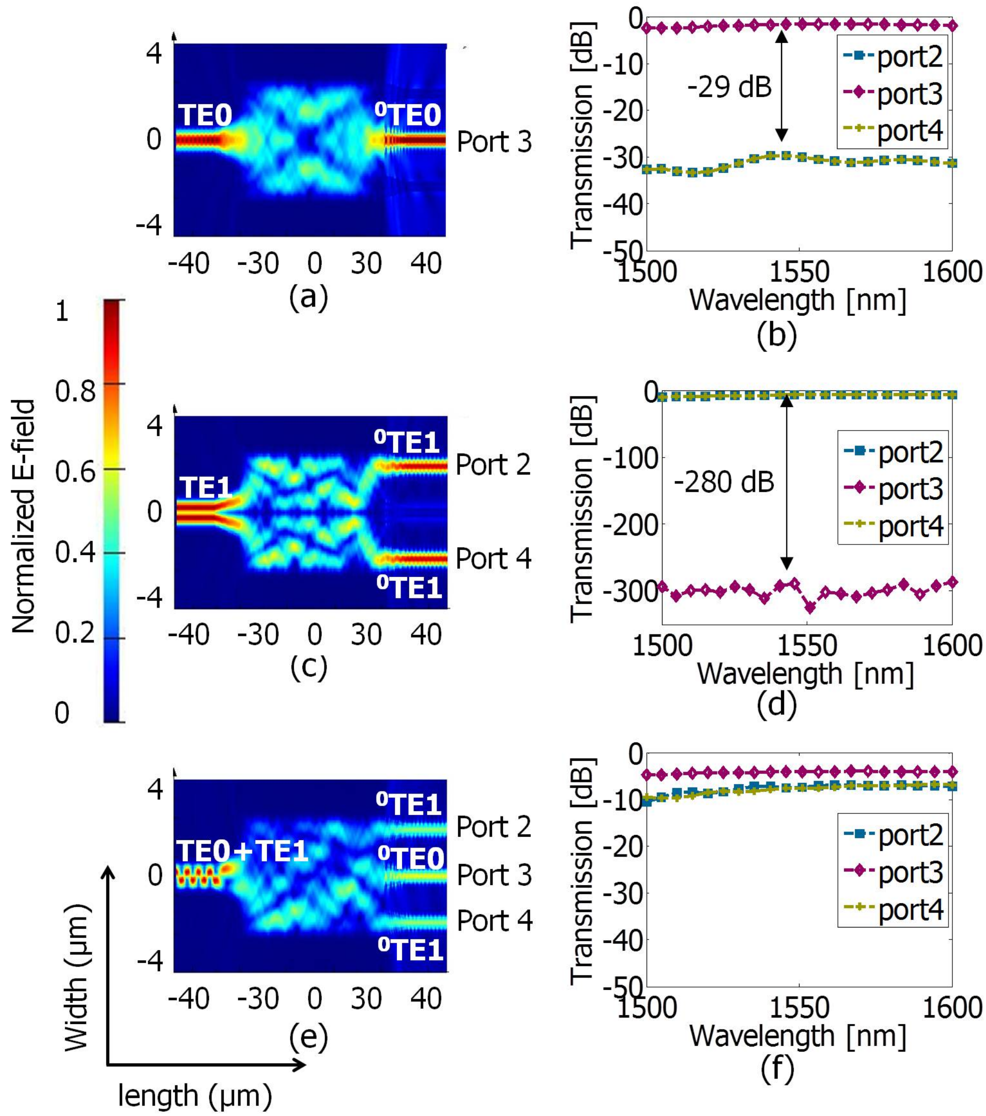

Figure 4.8 Simulated electric fields (left) and optical transmissions (right) of the RMDS, marked by the orange box in Fig. 4.7. The top (a, b), middle (c, d) and bottom (e, f) images represent the individual-mode TE0, individual-mode TE1, and dual-mode (TE0+TE1) transmissions.

mode to its multimode output port. The RMDS then decomposes these two mode components as ^{0}TE1 at its port2 and port4 output ports, as shown in Fig. 4.8(c). These two mode components are phase-matched by the PS-2 phase shifter, recombined by the 3-dB coupler, and retrieved at the *TE1-out* output port with simulation results estimating insignificant crosstalk (<-280 dB) and an IL ranging from -6.3 dB to -9.0 dB in C-band (1500 nm-1600 nm), as shown in Fig. 4.8(d).

For dual-mode transmission, the CW input from a single laser is power divided by an off-chip 50/50 power splitter to simultaneously couple two optical signals to both the *TE0-in* and the *TE1-in* input ports. The RMDS decomposes the multimode (TE0+TE1) signal and maps the ^{0}TE0 component to port3, and the two ^{0}TE1 components to port2 and port4, respectively (Fig. 4.8(e)). The simulated IL obtained are -7.3 dB, -4.0 dB and -7.5 dB at port2, port3 and port4, respectively, as shown in Fig. 4.8(f). The degradation in IL may arise from the inter-modal cross-coupling between the TE0 and the TE1 modes while propagating through the multimode waveguide. This may cause a power leakage in the net transmission of the corresponding modes at the output ports.

The MD was fabricated using a 193 nm deep ultraviolet (DUV) lithography at the Institute of Microelectronics (A*STAR IME), through a multi-project wafer (MPW) service managed by Canadian Microelectronic Corporation (CMC) Microsystems. The optical microscope image of the fabricated chip is shown in Fig. 4.9(a). Although two waveguide crossings at C1 and C2 are shown in the schematic in Fig. 4.7, these crossings are removed in the design layout by unfolding the input and output waveguides, and routing them around the grating coupler array to reduce inter-mode cross-coupling. Indeed, this modification in the device layout increases the total device footprint which can be reduced by using a low-loss waveguide crossing. Fig. 4.9(b) is a zoomed-in view of the fabricated RMDS, which is

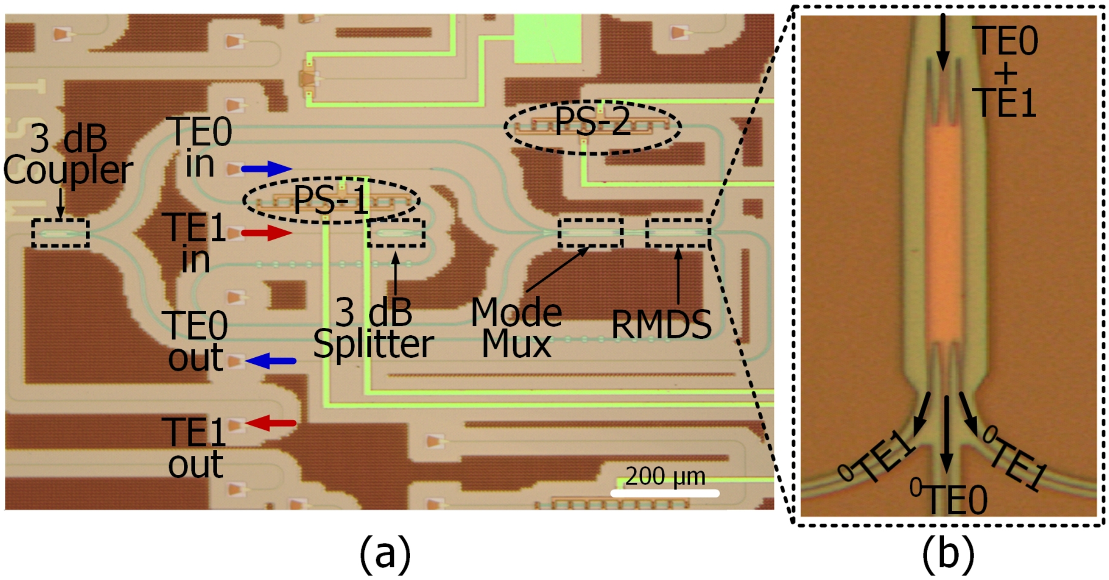

Figure 4.9 (a) Optical micrograph of the fabricated chip of the mode demultiplexer using the RMDS; (b) zoomed-in optical micrograph of the RMDS.

designed as a 3×3 MMI coupler using the principle of general interference but fabricated as a 1×3 MMI, where 30 μm long tapers are added at the unused ports to reduce the reflection loss.

4.2.2 Experimental results

The experimental setup to validate the fabricated chip is shown in Fig. 4.10. First, the MD is characterized with a CW optical signal using a tunable laser source (Yenista Tunics T100R). On-chip surface grating couplers with a 3-dB bandwidth of 47 nm at 1550 nm vertically couple the continuous wave (CW) optical signal at the fundamental TE mode from the laser through a fiber array. The polarization of the broadband optical signal is maintained at TE polarization by a polarization controller of 0.5 dB IL. This is necessary to remove

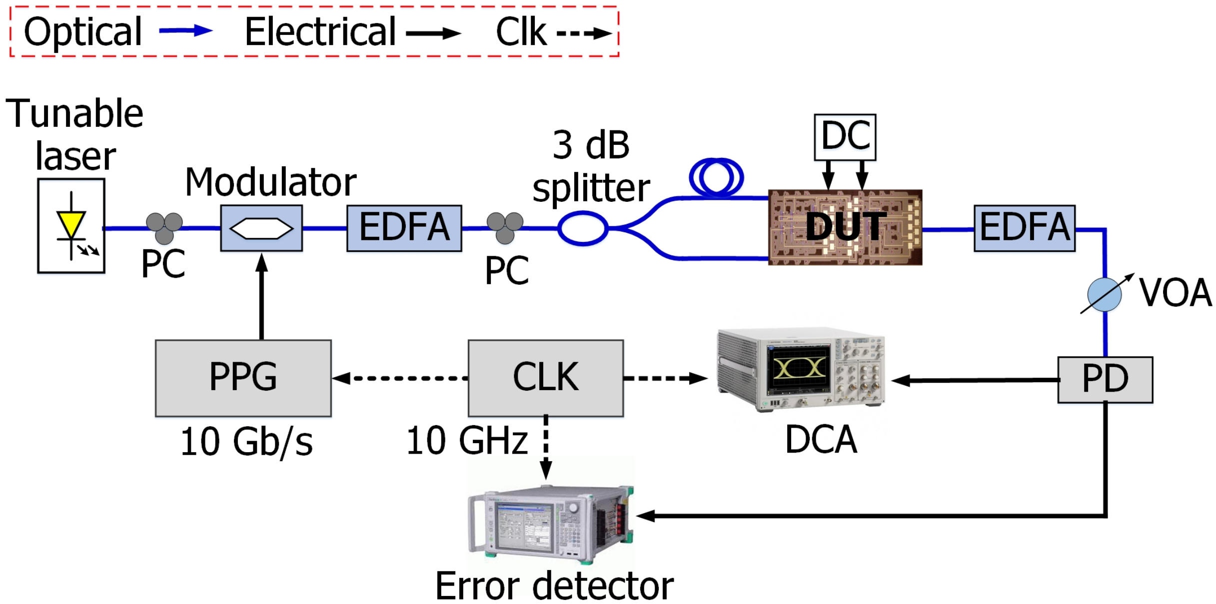

Figure 4.10 Experimental setup for the mode demultiplexer measurement. The optical and the electrical connections are shown as blue and black lines, respectively. EDFA: Erbium doped fiber amplifier, PC: polarization controller, DUT: device under test, VOA: Variable optical attenuator, PD: photodetector, DCA: digital communication analyzer, PPG: Programmable pattern generator, CLK: clock synthesizer. The DCA and error detector are not connected at the same time to the photodetector.

the polarization dependent loss caused by the polarization sensitivity of the GCs. For the individual-mode measurement, the input power is 0 dBm. For the dual-mode measurement, the optical input power is increased to 3 dBm to compensate for the 50/50 splitter. The decorrelation of two channels is performed through an SMF-28 fiber delay line providing 480 bit delay between the two propagating channels (>16-bit minimum walk-off requirement [134]). A short waveguide connecting two vertical grating couplers is used as a reference structure for the fiber-to-fiber insertion loss (IL) measured to be -10.5 dB at 1550 nm. The optical transmissions are normalized to the IL of this reference waveguide.

The optical transmissions as a function of wavelength for both individual-mode and dual-mode are shown in Fig. 4.11. For the individual-mode transmission at 1550 nm (Fig. 4.11(a)), the IL for the TE0 mode (*TE0-in*→*TE0-out*) is -2.2 dB, and for the TE1 mode (*TE1-in*→*TE1-out*), it is -6.0 dB. As the TE1 mode propagates with a lower effective refractive index than the TE0 mode (Fig. 4.2), it is likely that the corresponding TE1 optical beam is less confined inside the multimode waveguide with a longer evanescent tail being outside the waveguide core. This may lead to higher IL for the TE1 mode. The crosstalks for the TE0 transmission (*TE0-in*→*TE1-out*) is less than -21.0 dB and that for TE1 transmission (*TE1-in*→*TE0-out*) is less than -20.0 dB over 100 nm wavelength range. For the dual-mode transmission (Fig. 4.11(b)), the TE0 and TE1 modes exhibit -5.5 dB and -7.3 dB IL, respectively. The higher IL in the multimode transmission indicates inter-modal cross-coupling between TE0 and TE1 modes, and possibly modal leakage of the higher order quasi-TE (e.g., TE2, TE3) and quasi-TM (e.g., TM0, TM1) modes. Although the effective refractive indices of these modes are very small (<1.95 for the strip waveguide as reported in [77]) resulting in negligible optical power transmission, these undesired modes may cause the leakage of optical power from the dominant TE0 and TE1 modes leading to higher loss.

For payload data transmission, a 10 Gb/s NRZ PRBS31 signal is generated by an Anritsu MP 1800A programmable pattern generator (PPG). A modulated and amplified optical input signal is coupled to the device under test (DUT) in quasi-TE polarization, maintained by a polarization controller (PC). The output is detected by a 20 GHz photodetector (PD) of -18 dB sensitivity. For the back-to-back (B2B) BER measurement, reported in Figs. 4.13(a)

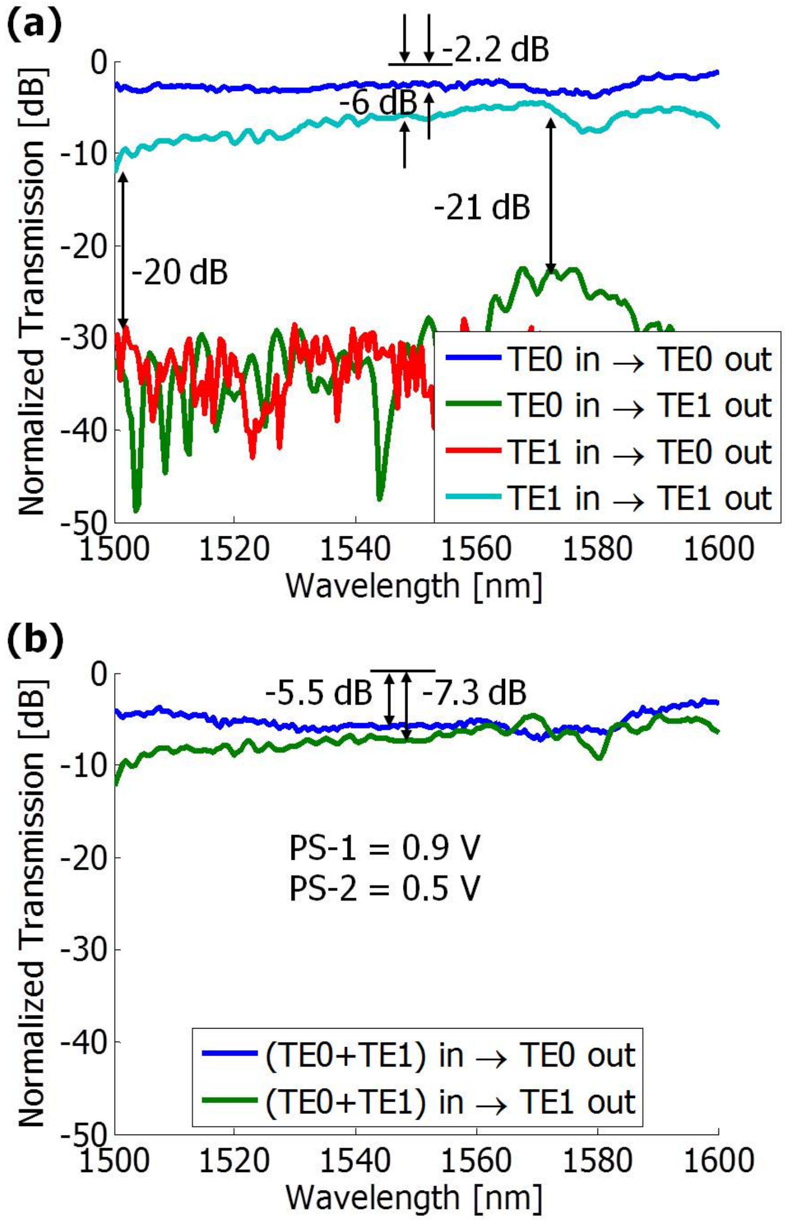

Figure 4.11 Normalized optical transmissions for (a) individual-mode and (b) dual-mode of the mode demultiplexer (MD) as a function of wavelength.

and (b), the DUT is replaced by an optical attenuator (VOA) with the corresponding loss of the TE0-out transmission in both cases. An Anritsu 20 GHz signal generator is used as the clock synthesizer to provide the external clock to the PPG and the error detector, and

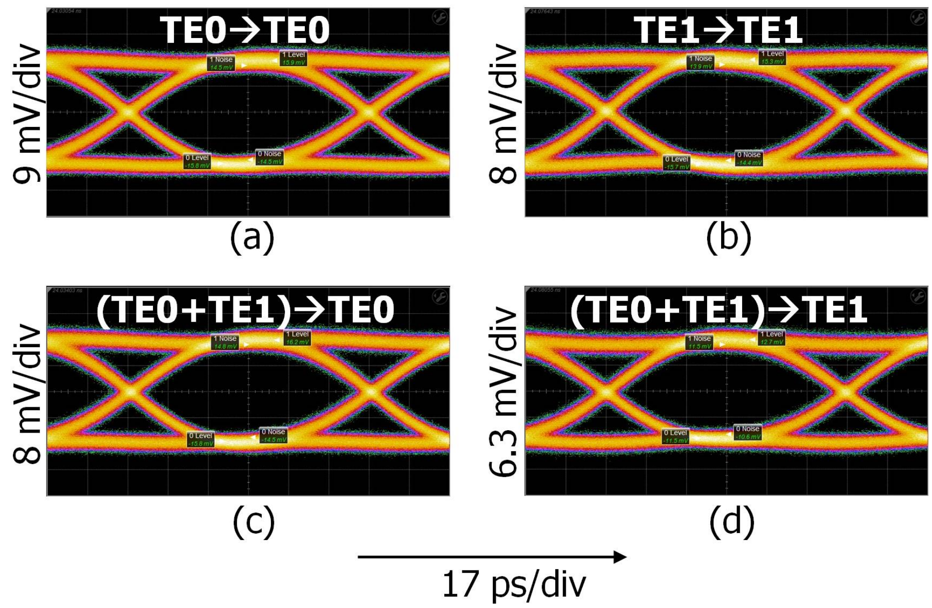

Figure 4.12 Recorded eye diagram of the mode demultiplexer for the individual-mode (top) and dual-mode (bottom) inputs.

the trigger to the Agilent 86100C digital communication analyzer (DCA) for recording eye diagrams. The eye diagrams in Figs. 4.12(a) and (b) are recorded for the individual-mode inputs in the TE0 (*TE0-in*→*TE0-out*) and the TE1 (*TE1-in*→*TE1-out*) transmissions, respectively. For the dual-mode input (TE0+TE1), the optical payload is transmitted simultaneously over both TE0 and TE1 modes and the eye diagrams are recorded at the *TE0-out* and *TE1-out* output ports, shown in Figs. 4.12(c) and (d), respectively. Clear and open eyes are observed in all channels demonstrating distortion-free high-speed data transmission for both TE0 and TE1 modes.

The measured BER as a function of the average received optical power is shown in Fig. 4.13(a) for the individual-mode and in Fig. 4.13(b) for the dual-mode transmissions along with the back-to-back (B2B) conditions in both cases. A BER of 10^{-12} is observed

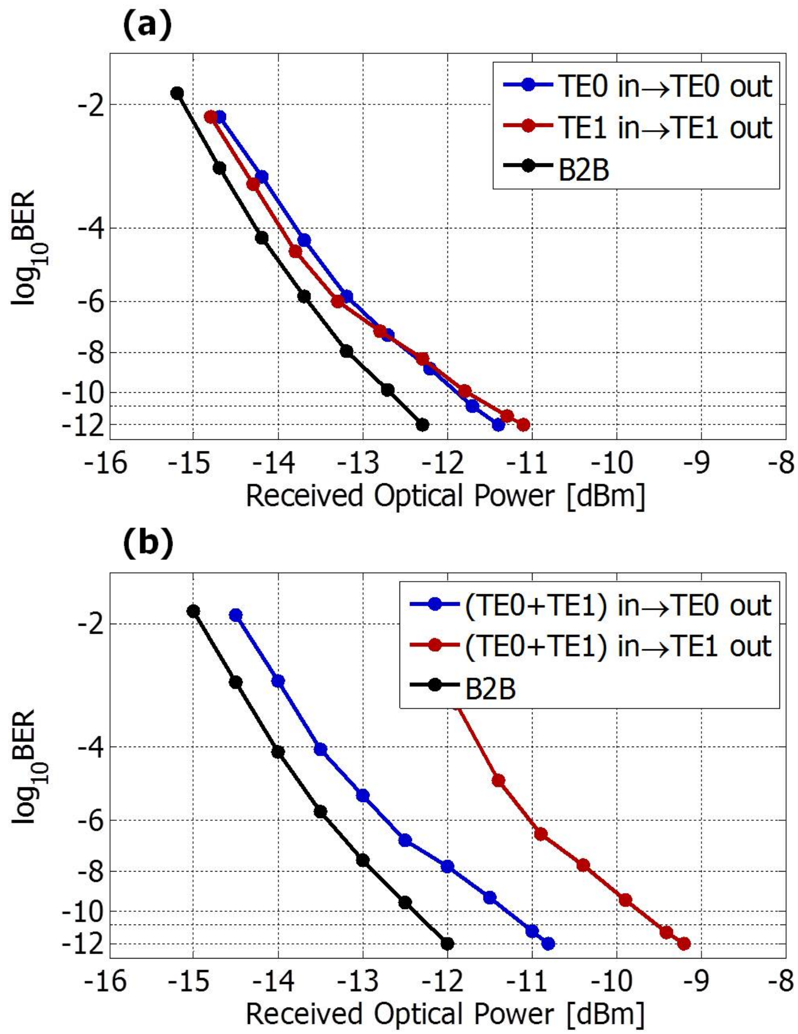

Figure 4.13 Measured BER (log-scale) of the demultiplexer for (a) individual-mode and (b) dual-mode transmissions as a function of average optical power (dBm), received by a 20 GHz photoreceiver of -18 dB sensitivity and 0.8 A/W responsivity.

for all channels at an aggregated data rate of 2×10 Gb/s demonstrating error free data transmission. The power penalties in the individual-mode transmission (Fig. 4.11(a)) are 0.9 dB and 1.1 dB in the *TE0-out* and the *TE1-out* output ports, respectively. The cascaded MMI structures are likely causing greater inter-modal cross-coupling to higher-order modes

(TE2 and higher) resulting in BER power penalties. In dual-model transmission, the power penalties are 1.2 dB for the TE0 mode and 2.8 dB for the TE1 mode. The increase in BER power penalties is assumed to be the effect of higher order inter-modal cross-coupling and associated increase in IL in the multimode transmission as reported in Fig. 4.11(b). Note that no optical filter is used in the experiment as the filter adds -2.0 dB insertion loss without significant improvement of electrical SNR and eye-quality. This situation results in higher ASE noise in the photoreceiver which impacts the power penalty.

4.3 Mode switching

The RMDS is used in a mode selecting switch (MSS) consisting of cascaded MMI couplers and thermo-optic phase shifters for the fundamental and first-order transverse electric (TE) modes. The design is more robust against inter-modal crosstalk than conventional switches are, as no mode pre-processing, such as (de)multiplexing is required. Scalability can be achieved by varying the widths and lengths of the MMIs to map higher-order modes at the output ports and adding more phase-shift stages. Dynamic switching ability is experimentally verified with transmission of 10 Gb/s non-return-to-zero (NRZ) data packets, and bit error rate (BER) of 10^{-12} is achieved in all switching channels.

4.3.1 Design and working principle

The MSS is a 1×3 switch, as shown in Fig. 4.14(a), where the fundamental TE0 mode at the input port is mapped to the middle output port as is (TE0), and the first-order TE1 mode is

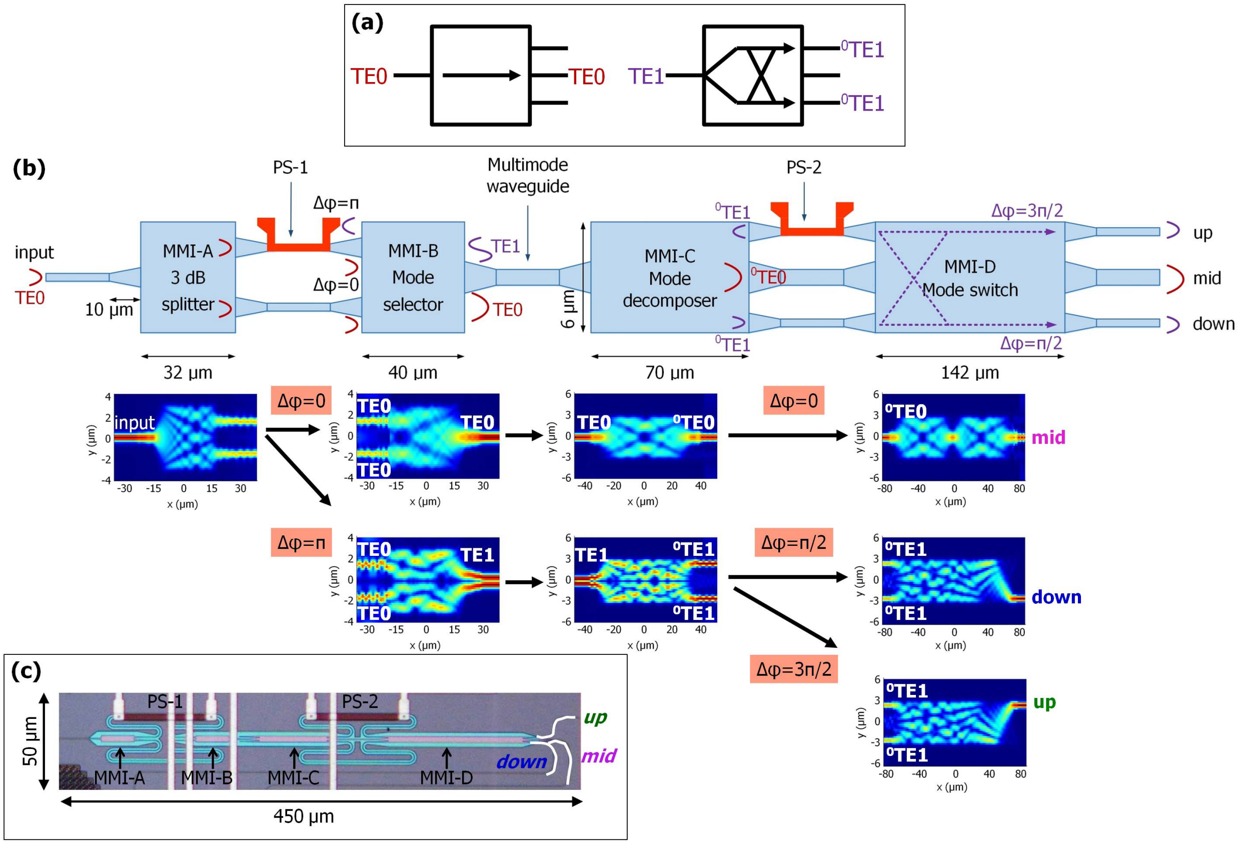

Figure 4.14 (a) Conceptual diagram of the 1×3 MSS, (b) schematic of the MSS and corresponding electric field propagation in respective MMIs under different phase shifter biases, (c) an optical microscope image of the fabricated MSS.

switched between the upper and the lower output ports after decomposing to its fundamental mode components (^{0}TE1). The MSS is designed using 220 nm SOI ridge waveguide with a 90 nm thick silicon slab supporting quasi-TE mode transmission at 1550 nm. The waveguide cross-section is shown in Fig. 4.2(a). The waveguide widths for the TE0 and the TE1 modes are the same as MD (Fig. 4.2(b)).

A schematic of the mode switch is shown in Fig. 4.14(b). The MSS also consists of four cascaded MMIs and two phase shifters (PS-1 and PS-2). Among the two phase shifters, PS-1 is tuned for selecting either the TE0 or the TE1 mode. The second phase shifter (PS-2) is tuned for spatially switching the modes among the three output ports of the mode switch MMI. Although the RMDS was designed for 70 μm length in the MSS, we later optimized the length to be 68 μm for better modal separation and less crosstalk in MD (Fig. 4.7). Indeed, this small difference in length was compensated by tuning the PS-2 phase shifter. The MSS was fabricated using the same service as for the MD. An optical microscopic image of the fabricated chip is shown in Fig. 4.14(c) with a footprint area of 450 μm $\times$ 50 μm. The footprint area is reduced by folding the waveguides with 7 μm bends forming a Mach-Zehnder interferometer (MZI) of 243 μm long arms.

The optical fields in the MSS for different phase-shift conditions are shown under the corresponding MMIs. The TE0 optical input is vertically coupled from a fiber array to the on-chip 500 nm wide single-mode waveguide by surface grating couplers with a 3 dB bandwidth of 47 nm operating at 1550 nm. The input optical beam is power-divided by MMI-A (3 dB power splitter) and is coupled to MMI-B's input ports with a phase-shift ($\Delta\phi_1$) provided by PS-1. The output beams of MMI-A undergo constructive ($\Delta\phi_1 = 0$) or destructive ($\Delta\phi_1 = \pi$) interference resulting in TE0 or TE1 modes, respectively, at the output port of MMI-B. The MMI-B output is tapered down to the 1000 nm width accommodating the TE1 mode. Thus MMI-B selects between TE0 and TE1 modes for the input of MMI-C. If TE0 is selected, MMI-C acting as a mode decomposer maps the mode field, as is, to its middle output as ^{0}TE0 without any decomposition but with a larger MFD which appears at the *mid* output of

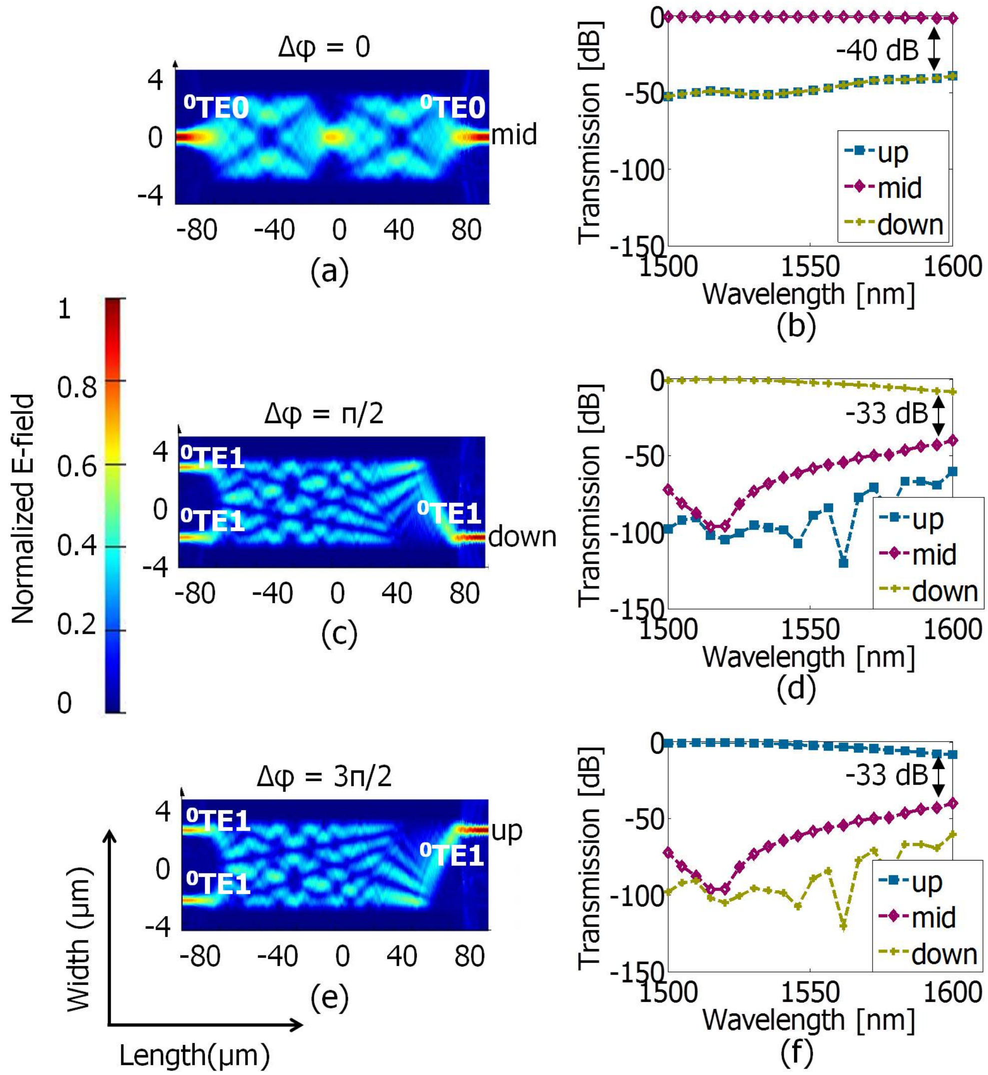

Figure 4.15 Simulated electric fields (left) and optical transmissions (right) of the mode switch MMI, marked by an orange line in Fig. 14. The *mid* (a, b) output corresponds to TE0 ($\Delta\phi = 0$) transmission. The *down* (c, d) and *up* (e, f) outputs correspond to TE1 transmissions for $\Delta\phi = \pi/2$ and $\Delta\phi = 3\pi/2$ phase-shifts.

the MSS. If TE1 in selected, MMI-C decomposes the mode fields into two fundamental mode components as ^{0}TE1 which are π-out-of-phase with each other. These mode components are recombined in MMI-D after a phase-shift applied by the PS-2 phase shifter. The ^{0}TE1 mode fields at the upper and the lower inputs of MMI-D are $\pi/2$ out-of-phase. The recombined ${}^{0}\text{TE1}_{\pi/2}$ is mapped to the *down* output for $\Delta\phi_2 = \pi/2$ and ${}^{0}\text{TE1}_{3\pi/2}$ mode is mapped to the *up* output for $\Delta\phi_2 = 3\pi/2$. The simulated electric fields of the mode switch MMI for three different phase-shift conditions of the PS-2 are shown in Figs. 4.15(a), (c) and (e), for the *mid*, *down*, and *up* output ports, respectively. The corresponding simulated transmissions are shown in Figs. 4.15(b), (d) and (f), respectively. In Fig. 4.15(b) (*mid* output), less than -40 dB crosstalk is estimated with -0.2 dB IL at 1550 nm. For the spatial switching of TE1 mode components, the estimated crosstalk is less than -33 dB and the IL at 1550 nm is -2.0 dB for both down and up output ports, as shown in Figs. 4.15(d) and (f), respectively.

4.3.2 Experimental results

The experimental test-bed for MSS measurement is shown in Fig. 4.16. A tunable laser source (Yenista Tunics T100R) with an output optical power of 0 dBm (1 mW) is used as the continuous wave (CW) source. A short SOI waveguide test structure connected by two vertical grating couplers with a measured fiber-to-fiber insertion loss of -10 dB at 1550 nm is used for normalizing the optical transmission results.

The optical transmissions at 1563 nm normalized to the waveguide test structure as a function of the bias voltages of PS-1 and PS-2 are shown in Figs. 4.17(a) (b), respectively. For the PS-1 phase shifter, a switching voltage (V_π) of 2.1 V switches between TE0 and TE1 modes denoted as 'TE0' (0 V; 0 mW) and 'TE1' (2.1 V; 23.3 mW) states, respectively, in Fig. 4.17(a). The 'TE0' and 'TE1' states exhibit -24.0 dB and -17.5 dB worst crosstalks,

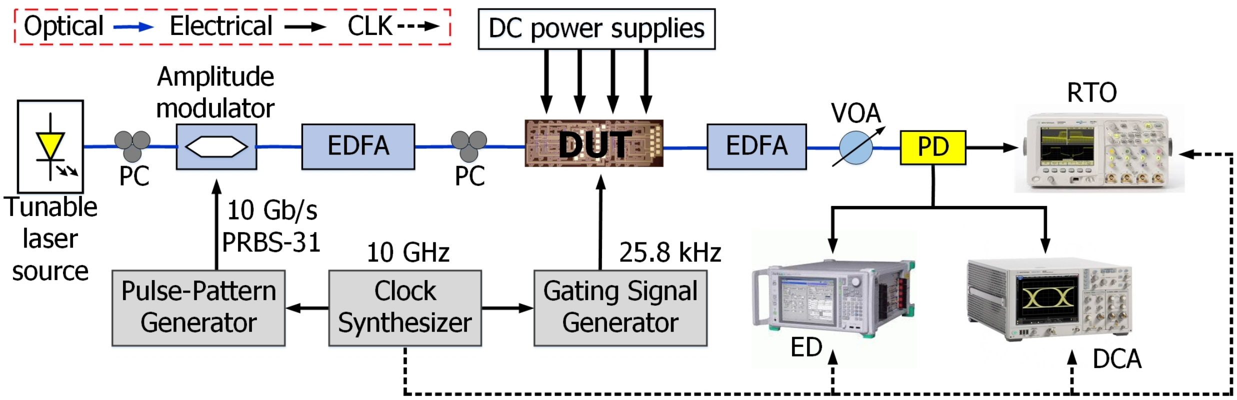

Figure 4.16 Experimental test-bed for the MSS characterization. The blue and black solid lines represent the optical and electrical signals, respectively. The black dotted line represents the clock signal. EDFA: Erbium doped fiber amplifier, PC: polarization controller, DUT: device under test, VOA: variable optical attenuator, PD: photodetector, PPG: programmable pattern generator, RTO: real-time oscilloscope, DCA: digital communication analyzer, ED: error detector.

respectively. The switching extinction ratio (ER) is 32.3 dB for the *mid* output. The insertion losses (ILs) at 'TE0' and 'TE1' states are -1.9 dB and -13.3 dB respectively. As the MSS does not consist of any mode-multiplexing stage as in [135], the input optical signal is coupled through a single surface grating coupler, designed for quasi-TE0 mode coupling, in 'TE0'state. The quasi-TE0 mode is then converted into a quasi-TE1 mode in 'TE1' state. The higher IL in 'TE1' state is caused by the phase shifter in the PS-1, used for achieving a destructive interference between the TE0 components at the output arms of MMI-A.

For the TE1 mode, the PS-2 phase shifter is activated only for 'TE1' state to switch the ^{0}TE1 mode components between the *up* and *down* output ports, as shown in Fig. 4.17(b). A switching voltage of 1.6 V is required to switch between the *down* (2.6 V; 30.0 mW) and *up* (4.2 V; 75.6 mW) output ports where the *mid* output remains non-responsive to the PS-2

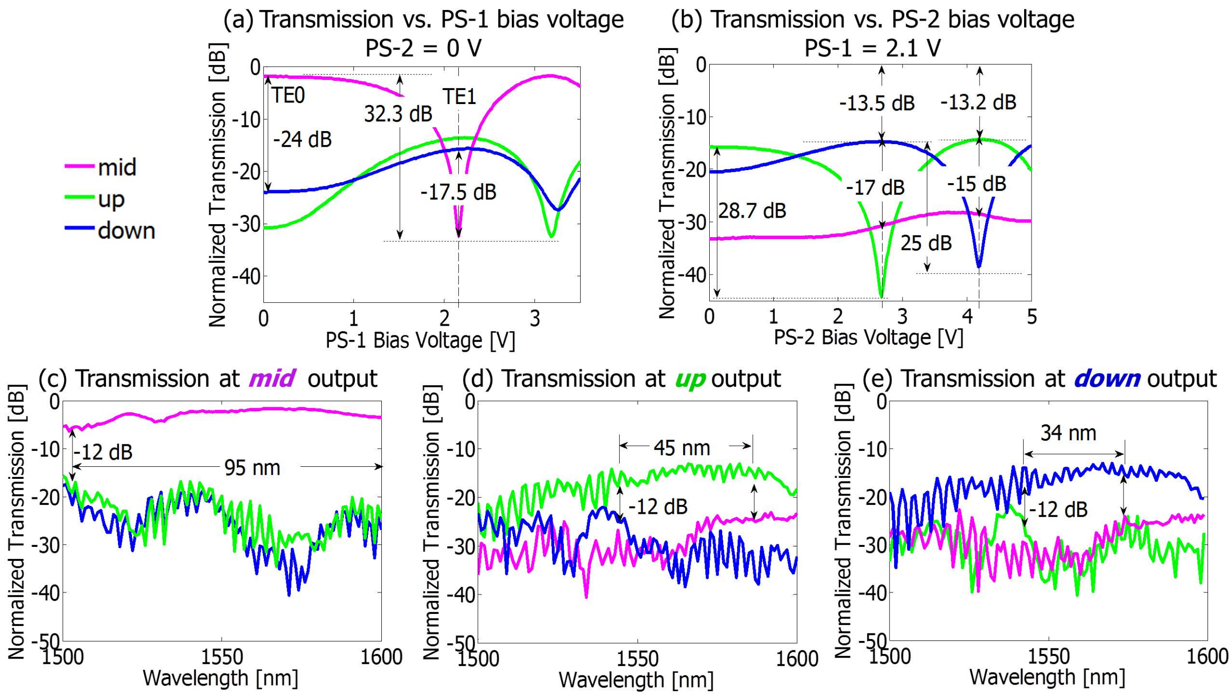

Figure 4.17 Normalized transmission as a function of (a) PS-1, and (b) PS-2 bias voltages. Normalized transmission as a function of wavelength in (c) *mid*, (d) *up*, and (e) *down* output ports.

bias. The ERs are 28.7 dB and 25.0 dB, and the worst crosstalks are -15.0 dB and -17.0 dB in *up* and *down* output ports, respectively. The ILs for the *up* and *down* outputs are -13.2 dB and -13.5 dB, respectively. The imbalance in ER and crosstalk is attributed to the possible misalignment of the fiber array simultaneously collecting the optical signals at the two output ports.

Figs. 4.17(c-e) are the normalized optical transmissions at the *mid*, *up* and *down* output ports as a function of wavelength from 1500 nm to 1600 nm. The *mid* output port exhibits less than -12 dB crosstalk for a 95 nm wavelength range (PS-1 = 0 V; PS-2 = 0 V). However, for the *down* and the *up* output ports, the bandwidth is limited to 34 nm and 45 nm, respectively, for the same crosstalk. The bandwidth limitation can be attributed to the difference in effective optical path lengths (ΔL) in the two arms of the Mach-Zehnder interferometer (MZI) structure due to fabrication variation. A periodic fluctuation is observed at the *down* and *up* output ports in Figs. 4.17(d) and (e), respectively, due to the constructive and destructive interference between the propagating waves in the two output arms of MMI-A. The measured free-spectral range (FSR) of this fluctuation is ∼2.5 nm which matches the calculated FSR ($FSR = \lambda^2/n_g L$) for a balanced MZI of 243 μm long arm with a group index of 3.92 at 1550 nm wavelength as comprised by MMI-A, MMI-B and PS-1. For switching higher order modes (*i.e.*, TE2 and TE3), MMI-A can be designed for more output ports, each associated with a PS, which increases the footprint of the MSS by ∼30 % per mode order without a significant performance degradation. For example, a 1×4 MMI based wavelength switch is reported in [66] with -1.7 dB IL, >11.48 dB ER and <-11.38 dB crosstalk.

To characterize the dynamic switching performance, an electrical square wave at 25.8 kHz with fall and rise times of 15.0 ns is applied to the MSS as the gating signal for PS-1 with a peak-to-peak voltage of 2.1 V. Fig. 4.18(a) shows the switching between TE0 and TE1 modes at the *mid*, *up* and *down* output ports, respectively, in response to the gating signal when PS-2 = 4.2 V. The measured rise and fall times of the TE0 mode (*mid* output) are 10.7 μs and 10.9 μs, respectively. For the TE1 mode, the fall and rise times at the *up* output port are 10.6 μs and 10.7 μs, respectively. The fall and rise times at the *down* output port are 10.9 μs and 10.6 μs, respectively.

For the switching performance on payload data, a 10 Gb/s NRZ PRBS31 signal is gen-

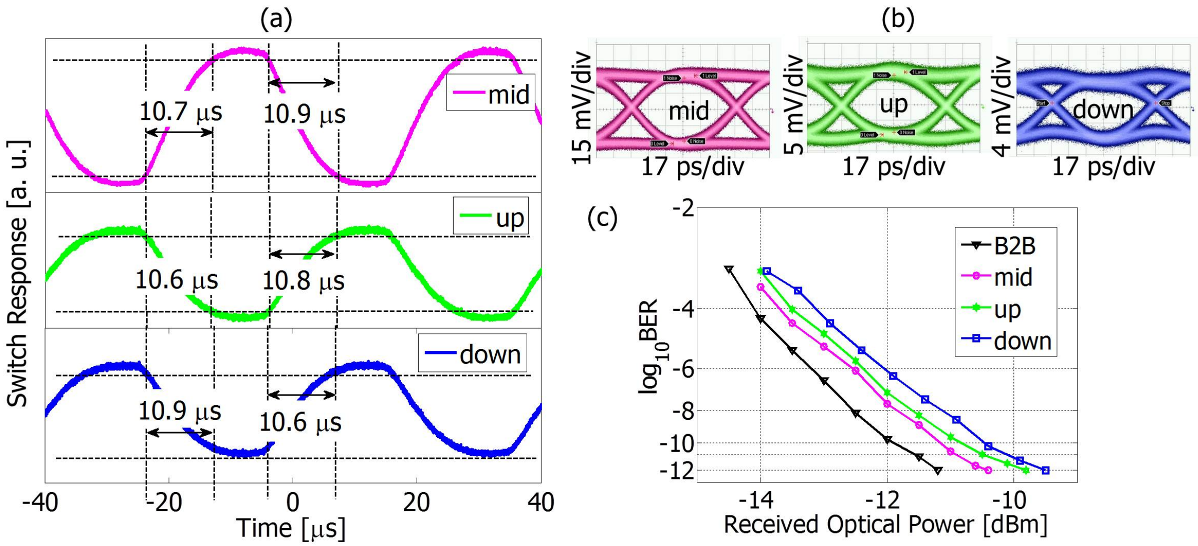

Figure 4.18 (a) Dynamic mode switching between TE0 (*mid* output port) and TE1 (*up* and *down* output ports) modes, (b) Eye diagrams in *mid*, *up* and *down* output ports recorded for 10 Gb/s PRBS31 optical data, (c) BER as a function of average received optical power at the PD in B2B configuration with respect to the *mid* output ports and in all three output ports while switching.

erated by an Anritsu MP 1800A programmable pattern generator (PPG) (Fig. 4.16). The optical signal, modulated by a $LiNbO_3$ amplitude modulator of 12 GHz of 3-dB bandwidth, is amplified by an erbium doped fiber amplifier (EDFA). A polarization controller (PC) maintains TE modes before coupling to the device under test (DUT). The input optical power to the DUT is fixed at 5 dBm. The optical signal at the output of the DUT is amplified by another EDFA followed by a variable optical attenuator (VOA) before being detected by a 20 GHz photodetector (PD) and recorded by a real-time oscilloscope (RTO). For the back-to-back (B2B) bit-error-rate (BER) measurement, reported in Fig. 4.18(c), the DUT is replaced by an optical attenuator with the same loss as the *mid* output. A clock synthesizer (Anritsu 20 GHz signal generator) is used to provide the external clock to the PPG, the error detector, and the trigger to the Agilent 86100C digital communication analyzer (DCA) for recording the eye diagrams. The eye diagrams recorded in all three switching output channels are shown in Fig. 4.18(b). Clear and open eyes are observed in all channels demonstrating distortion free high speed data transmission for both TE0 and TE1 modes. The measured BER by the error detector (ED) as a function of average received optical power at the PD are reported in Fig. 4.18(c) for all three output ports and for the B2B condition. A BER of 10^{-12} at a data rate of 10 Gb/s demonstrates error-free transmission. The power penalties for the *mid*, *up* and *down* output ports with respect to the B2B are 0.8 dB, 1.4 dB and 1.7 dB, respectively. These penalties can be attributed to the higher mode manipulation in the cascaded MMI structures and cross-coupling to higher order modes (TE2 and higher). Although the responsivity of the photoreceiver is stable over the full C-band (1500 nm - 1600 nm), the 3-dB bandwidth of the off-chip $LiNbO_3$ modulator is small (12 GHz at 1550 nm). The wavelength sensitivity of the TE1 mode may increase the BER power penalty as the operating wavelength changes. This limitation can be overcome by using an on-chip wavelength- and bandwidth-tunable micro-ring modulator [128].

4.4 On-chip power budget

The experimental results are summarized in Table 4.1 for both the MD and the MSS. The higher IL of -13.5 dB for the TE1 mode in the MSS is due to the destructive interference, applied by the PS-1 phase shifter, between two input arms of the mode selector MMI

Table 4.1 Experimental results of the mode (de)multiplexer (MD) and the mode selecting switch (MSS) using RMDS as the building block

Parameter	MD				MSS		
Transmission	Individual-mode		Dual-mode		TE0	TE1	
Mode	TE0	TE1	TE0	TE1	mid	down	up
IL (dB)	-21.0	-20.0	—	—	-24.0	-17.0	-15.0
Crosstalk (dB)	-6.0	-2.0	-5.5	-7.3	-1.9	-13.5	-13.2
Operating range (nm)	100	100	100	100	95	34	45
Switching time (μs)	—	—	—	—	10.9	10.9	10.8
Electrical power (mW)	0.13	14.7	12.3	12.3	13.6	64.5	123.0
BER power penalty (dB)	0.9	1.1	1.2	2.8	0.8	1.7	1.4

(Fig. 4.14(a)). This is required to cancel the TE0 mode, and select TE1 mode for switching. The 10.9 μs switching time can be further improved to 1.8 μs by using resistive heater phase shifter [117]. The electrical power consumption of the MSS is higher due to the lower thermo-optic tuning efficiency of the TiN heater as measured to be 35.5 mW/π compared to that of resistive heater of 21 mW/π [136]. Although the TE1 output of the dual-mode transmission in the MD exhibits higher BER power penalty of 2.8 dB, it is sufficient for a good eye opening as shown in Fig. 4.12(d), and comparable to the reported value in [31].

To estimate the overall on-chip power consumption of an MDM link, we consider the dual-mode transmission of the MD. The on-chip optical power of the laser was measured to be 10.8 dBm (12 mW), excluding the wall-plug efficiency. Considering a reported 3 mW receiver power including a hybrid integrated Ge-on-Si photodetector of -17 dB sensitivity, 0.8 mW electrical power and 3 mW thermal tuning power of a MRR based silicon modulator

Table 4.2 Estimated power budget for the proposed on-chip RMDS based multimode link in dual-mode transmission at 2×10 Gb/s

Link component	Electrical Power (mW)	Optical Loss (dB)
Laser	12.0	—
Modulator	3.8	-7.0
Fiber-to-GC coupling	—	-11.0
RMDS (dual-mode)	12.3	-7.3
Photo receiver	3.0	—
Total	31.1	-25.3
Energy efficiency	1.55 pJ/bit	

of -7 dB IL [137] and a measured 12.3 mW thermal-tuning power of the MD, the estimated total power consumption of the link is 31.1 mW at 2×10 Gb/s aggregated data rate. This corresponds to an on-chip energy efficiency of 1.55 pJ/bit, which is less than the reported estimated efficiency of 1.9 pJ/bit [16]. Intuitively, the efficiency of any device is expected to be as high as possible for better performance. However, energy efficiency in data centers is measured by the amount of energy required to transmit a single data bit, hence a lower value is expected [138, 139]. The optical link budget is shown in Table 4.2 for this link.

The RMDS can be scaled up to accommodate higher order quasi-TE (e.g., TE2, TE3, etc.) modes by carefully designing its width and length for mapping higher order modes. As each mode component will require some amount of phase-shift for switching and maintaining sufficient crosstalk between demultiplexed signals, the number of phase shifters will increase the total footprint. To compensate a probable increase in the BER power penalty caused by the higher inter-modal cross-coupling of the higher order modes, efficient and low-power phase shifters are required. Indeed, an experimental verification is needed to determine the plausible mode numbers for a scalable RMDS.

4.5 Summary

This chapter presented a reconfigurable multimode demultiplexer/switch (RMDS) as a building block for MDM silicon photonic (de)multiplexers and switches. The novel device that can be reconfigured performs both mode (de)multiplexing and mode switching of high speed optical data. An aggregated bandwidth of $2\times10\,\mathrm{Gb/s}$ is achieved at 10^{-12} BER with less than $2.8\,\mathrm{dB}$ power penalty. The RMDS can be scaled up for higher order mode transmission by engineering the length and the width of the MMI with more output ports and phase shifter stages. A multimode optical link using the RMDS is proposed with an estimated $1.55\,\mathrm{pJ/bit}$ energy efficiency. The RMDS can be used as a building block for the deployment of high capacity optical links in short-reach interconnects allowing the parallel transmission and switching of multiple independent data packets for a potential improvement in the energy/bit performance. The proposed MSS can be used for simultaneously (de)multiplexing and switching the optical data stream in a switch matrix, where the transmission of multiple independent optical data packets through a single optical link can improve the scalability and bandwidth capacity.

Chapter 5

Scalable multimode switch for energy-efficient MDM systems

In this chapter, we present a reconfigurable and scalable multimode switch (SMS) using cascaded MMI couplers and titanium/tungsten (Ti/W) metal heater phase shifters operating in the C-band. Simultaneous transmission and switching of two parallel data channels over two transverse electric (TE) modes i.e., TE0 and TE1, is demonstrated. A similar design is reported in [93] consisting of cascaded MMIs and passive waveguide phase shifters for WDM-MDM and WDM-PDM conversion, but without reconfigurable switching. We discussed the design and experimental validation of the reconfigurable mode (de)multiplexer/switch (RMDS) in chapter 4. This RMDS is optimized with a larger length, as discussed in section 4.4, and used to design the SMS for higher order TE modes, i.e., TE0, TE1, and TE2 enabling path-reconfigurable switching among three single-mode output ports. The same device can be used for switching either 2-mode (TE0 and TE1) or 3-mode (TE0, TE1, and TE2) switching offering footprint efficiency. As a proof-of-concept demonstration, a 2-mode switch for the fundamental and the first order quasi-TE modes is experimentally measured. The quasi-TE0 and quasi-TE1 modes are launched using only one C-band tunable laser (from 1520 nm to 1580 nm) improving the energy efficiency. The 2-mode SMS exhibits -6.5 dB insertion loss (IL) in bar state and -7.3 dB IL in cross state with a worst-case switching extinction ratio (ER) of 17.7 dB in individual-mode switching. Dynamic switching between two 10 Gb/s nonreturn-to-zero (NRZ) data packets confirms a switching time of less than 9.8 μs with an average heater power of 64.8 mW. Less than -7.0 dB IL and greater than 12.0 dB ER are observed in dual-mode switching. Clear and open eye diagrams are recorded at 10 Gb/s confirming distortion free data transmission with 2×10 Gb/s aggregated bandwidth. The scalability analysis estimates a projected -9.0 dB IL and an average 193.0 mW thermal tuning power for a 6-mode switch (i.e. TE0, TE1, TE2, TE3, TE4 and TE5) saving up to 63% energy compared to a single-mode switch. The proposed SMS can be potentially used in the high-throughput energy-efficient photonics switching. Some results presented in this chapter are published in [140] and [141].

5.1 Design and working principle

The schematic of the proposed scalable multimode switch (SMS) is shown in Fig. 5.1 with simplified block diagrams of a 2-mode switch and a 3-mode switch. The 2-mode switch

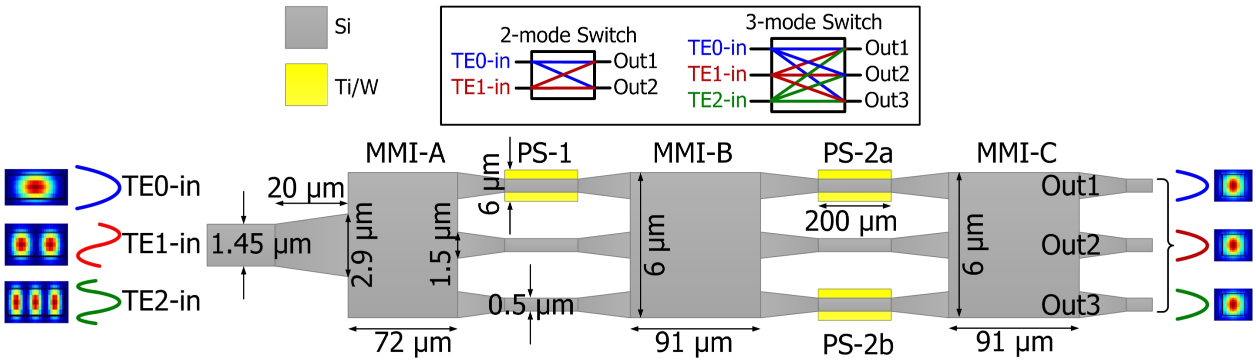

Figure 5.1 Schematic of the scalable multimode switch (SMS) with three multimode inputs denoted as *TE0-in*, *TE1-in* and *TE2-in*; and three single-mode outputs, denoted as *Out1*, *Out2* and *Out3*. The block diagrams of a 2-mode switch and a 3-mode switch are shown on top.

can switch *TE0-in* and *TE1-in* input modes between *Out1* and *Out2* output ports. In the 3-mode switch, each of the first three TE modes (i.e. TE0, TE1 and TE2) can be switched among three output ports: *Out1*, *Out2* and *Out3*. The SMS consists of three cascaded MMIs (MMI-A, MMI-B and MMI-C) and three metal heater phase shifters (PS-1, PS2a and PS-2b). The waveguide cross-section is shown in Fig. 5.2(a). The waveguide widths for single-mode and multimode propagations are optimized by eigenmode simulation using a commercial CAD tool (Lumerical Mode solution). The widths for TE0, TE1 and TE2 mode propagations are chosen to be 0.5 μm, 1.0 μm and 1.45 μm, respectively, optimized by finite difference eigenmode (FDE) simulation, as shown in Fig. 5.2(b).

5.1.1 Working principle

First three TE modes are multiplexed using a broadband ADC based mode multiplexer, designed following [140]. The multiplexed mixed-mode signal propagates through the mul-

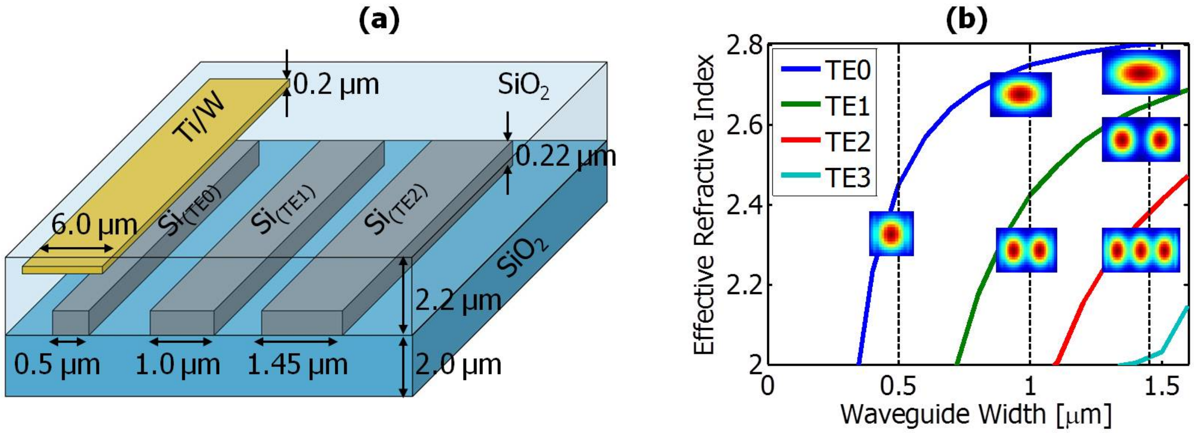

Figure 5.2 (a) Cross-section of the single-mode (TE0), and multimode (TE1, and TE2) waveguides with Ti/W metal heater phase shifter. The heater is placed 2.0 μm over the single-mode waveguide; (b) simulated effective refractive indices for the first four TE modes showing the simulated electric field for each mode.

timode waveguide and coupled to the input port of MMI-A, which is the reconfigurable multimode demultiplexer/switch (RMDS) consisting of a 72 μm long 1×3 MMI coupler, designed using the mechanism of symmetric interference. We discussed the design and working principle of the RMDS in chapter 4. The input port of the MMI-A has a 2.9 μm wide and 20 μm long taper for the multimode transmission to adiabatically couple TE0, TE1 and TE2 modes to the MMI-A. As MMI-A and the RMDS are designed using the same methodologies, and they operate following the same self-imaging pronciple, we expect a similar fabrication tolerance for the both components, as studied in chapter 4, and hence not repeated here. All I/O ports of the MMI-B and MMI-C have 1.5 μm wide and 20 μm long linear tapers for single-mode transmission. These tapers minimize the optical return losses at each step. The widths of the MMIs are fixed at 6 μm. The lengths of MMI-B and MMI-C are optimized by a fully vectorial and bi-directional eigenmode expansion model, and are chosen to be 91 μm. MMI-B and MMI-C are identically designed with equal widths and lengths, based on the principle of 120° optical hybrid [142]. They form a Mach-Zehnder Interferometer (MZI) enabling reconfigurable switching among the *Out1*, *Out2* and *Out3* single-mode output ports. As MZI based integrated switches need precise control over the power coupling ratios between the coupler's output ports, fabrication tolerant and broadband MMI couplers are a better choice than the ADC and the Y-junction leading to higher extinction ratio (>25.0 dB) and lower crosstalk [62]. The self-imaging principle of the MMI coupler [63] allows conversion, tuning and low-loss propagation of multiple guided modes using a single set of photonic components reducing footprint and power consumption. The detail design methodology of the MMIs is reported in [70]. Each metal heater phase shifter is 6 μm wide and 200 μm long consisting of 200 nm thick thin film of Ti/W alloy, as shown in Fig. 5.5(e) of the following section, of 4 Ω/sq sheet resistance.

5.1.2 Design of the mode decomposer MMI

Fig. 5.3 shows the simulated electric fields in MMI-A and MMI-B for three input modes. The input TE0 mode (*TE0-in*) is mapped onto the middle output port of MMI-A with a smaller mode field diameter (MFD), as shown in Fig. 5.3(a), due to the smaller widths of the taper and the waveguide at the output ports. To mitigate the complexities of manipulating different mode orders in the same structure, the higher order TE modes are decomposed to their fundamental components before phase-tuning and propagating through the device.

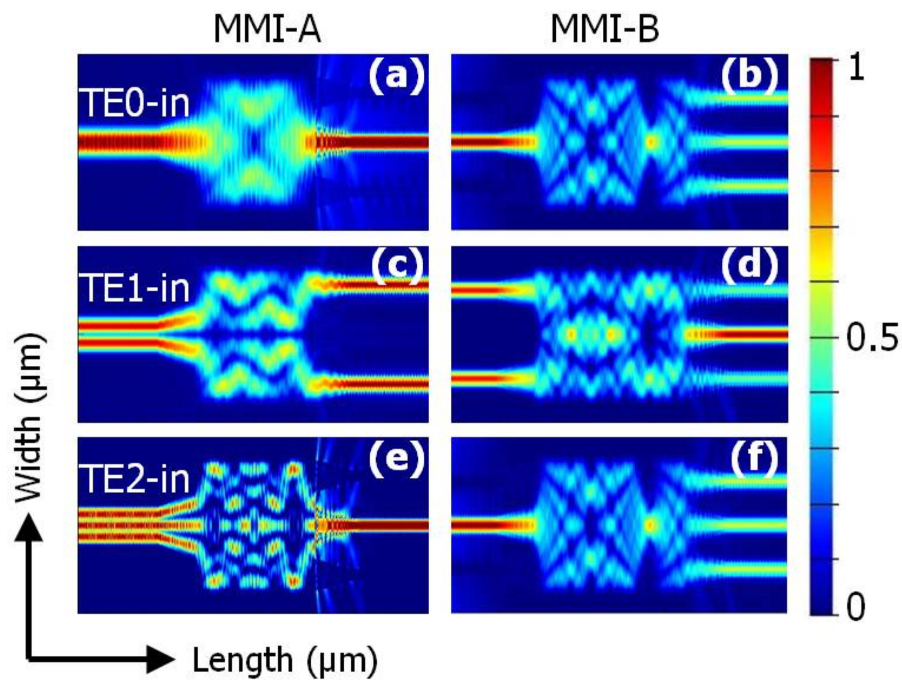

Figure 5.3 Simulated electric fields of the MMI-A (left) and MMI-B (right) at 1550 nm. The top (a, b), middle (c, d) and bottom (e, f) images represent the propagation of TE0, TE1 and TE2 modes, respectively.

The fundamental components of the *TE1-in* input mode are mapped to the upper and the lower output ports with a π-phase shift (Fig. 5.3(c)). The TE2 mode input (*TE2-in*) is converted to the fundamental mode with a 66% conversion efficiency, and then mapped to the middle output port of MMI-A (Fig. 5.3(e)). The reason for the lower conversion efficiency is explained by the odd/even mode-parity [89]. In a 1×3 symmetric interference based MMI, like MMI-A, the input even modes (i.e. TE0 and TE2) reproduce themselves in the middle output port with 100% theoretical efficiency. However, the odd modes (i.e., TE1 and TE3) are converted into lower order modes and equally divided in the upper and the lower output ports [92, 143]. Thus, the input *TE1-in* mode is divided into TE0 components, as shown in

Fig. 5.3(c).

As the input *TE2-in* mode is not converted to its fundamental components in MMI-A's middle output port, phase-tuning of this higher order mode requires a mode insensitive phase shifter which adds complexity to the device and increases the inter-modal crosstalk, hence this scheme is avoided. An additional mode converter efficiently performs the TE2→ TE0 conversion but, at the same time, filters out the input TE0 mode [144]. A longer device formed by cascaded MMIs and passive phase shifters can potentially improve the conversion efficiency, as proposed in [90], but significantly increase the device length. Moreover, this device is not capable of mode (de)multiplexing. As a design trade-off, the length of MMI-A is optimized such that the odd/even parity is discontinued at the output end for the *TE2-in* input mode resulting in a lower TE2→TE0 conversion efficiency at the cost of an increased IL in the switching output ports. A small phase-shift, applied by the PS-1 phase shifter, is required for precise control of the decomposed components of *TE1-in* and *TE2-in* input modes. The fundamental components of *TE0-in*, *TE1-in* and *TE2-in* modes are coupled to the input ports of MMI-B as shown in Figs. 5.3(b), (d) and (f), respectively. MMI-B, being a 120° optical hybrid, causes a $2\pi/3$ phase difference between each output ports. The incoming light is equally distributed among the output ports of MMI-B for the *TE0-in* and the *TE2-in* modes. The imbalance in power splitting observed in the *TE1-in* mode (Fig. 5.3(d)) is compensated by the PS-2a and PS-2b phase shifters by an additional phase-shift of 0-2.5 V, which also tune the relative phases of the MMI-B outputs before coupling them onto MMI-C.

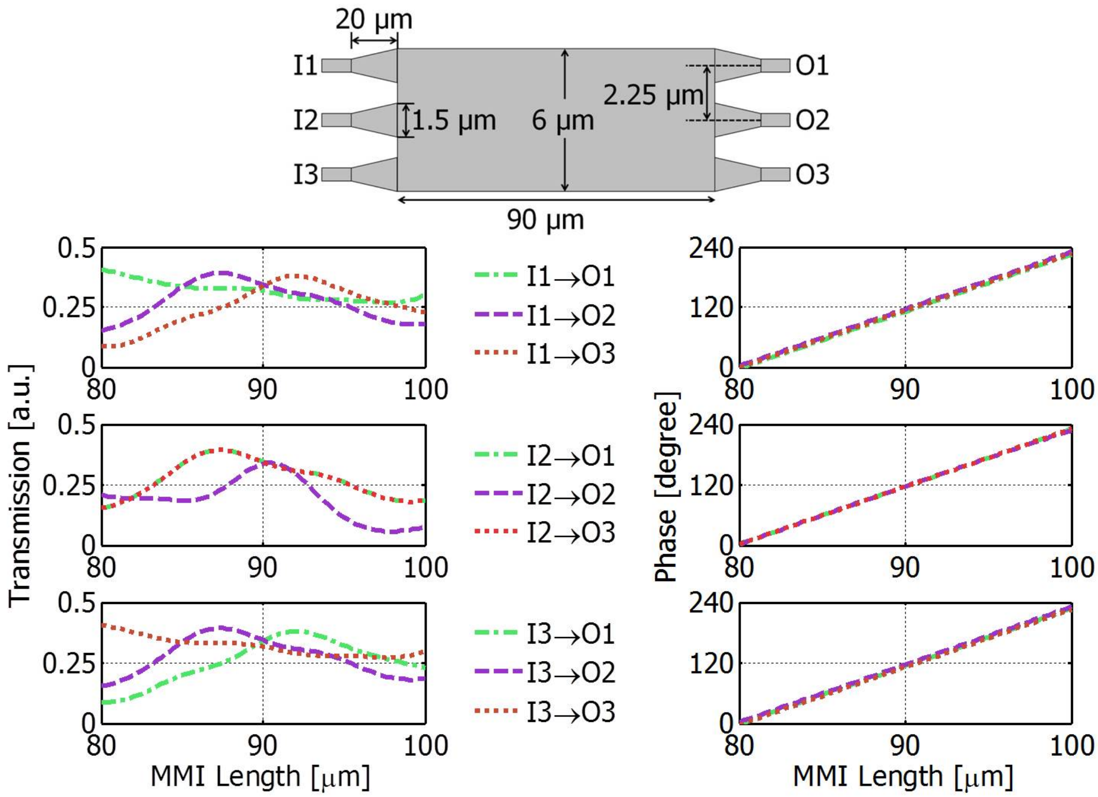

Figure 5.4 Simulated optical transmission (left) and relative phase difference in the output ports of the 120° optical hybrid (MMI-B and MMI-C) as a function of MMI length. The 2D schematic of the MMI is shown above the transmission plot.

5.1.3 Design of the 120° optical hybrid

MMI-B and MMI-C are identically designed to operate as a 120° optical hybrid [142], where each of the output ports (O1, O2, and O3) receives one-third of the input optical power from any of the input ports (I1, I2, and I3). According to the principle of general interference, the optical phases of a N×N MMI are determined by Fourier analysis in [63] and can be expressed as

$$\varphi_{rs} = \frac{\pi}{4N}(s-1)(2N+r-s)+\pi \qquad \text{for r+s even} \tag{5.1}$$

$$\varphi_{rs} = \frac{\pi}{4N}(r+s-1)(2N-r-s+1) \qquad \text{for r+s odd} \tag{5.2}$$

where $r = 1, 2, \ldots, N$ corresponds to the input port number for a bottom-up position, and $s = 1, 2, \ldots, N$ is the output port number following a top-down position. For a 3×3 MMI ($N = 3$), the phase-difference between the output ports is $2\pi/3$ for any input port, which satisfies the condition of a 120° hybrid. For a given beat length, $L_\pi = \dfrac{\pi}{(\beta_0 - \beta_1)}$, the length of this MMI to form the M-th P-fold image is calculated using the following equation, where M represents the order of self-image and P represents the number of self-image of the input light:

$$L_{MMI} = \frac{M}{P}(3L_\pi) \tag{5.3}$$

For a 6.0 μm width and 89.1 μm estimated beat length, the first ($M = 1$) three-fold ($P = 3$) image appears at approximately 89.1 μm away from the input location. A length sweep of MMI-B using Lumerical's eigenmode expansion (EME) simulation estimates the optimal length to be 90.0 μm to achieve 33% power splitting and 120° relative phase-shift in each output port regardless of the input ports, as shown in Fig. 5.4. The length and width of the tapers, and the locations of the input/output ports are also optimized using EME simulation with a 20 nm uniform mesh in all cases.

5.1.4 Design of the switching MMI

The MZI formed by MMI-B and MMI-C provides reconfigurable switching of the three input modes. The simulated electric fields in MMI-C for switching among *Out1*, *Out2*, and *Out3* output ports are shown in Figs. 5.5(a), (c) and (e), respectively. The corresponding calculated optical transmissions as a function of wavelengths are shown in Figs. 5.5(b), (d) and (f), respectively. A relative phase-shift of $2\pi/3$ is required between the PS-2a and the PS-2b phase shifters to enable reconfigurable switching. For the *Out1* transmission, the phase-shifts at PS-2a and PS-2b are set to $2\pi/3$ and 0, respectively. When the switching output appears at the *Out2* port, PS-2a $= 2\pi/3$ and PS-2b $= -2\pi/3$. Finally, for the *Out3* transmission, the phase-shifts at PS-2a and PS-2b are 0 and $2\pi/3$, respectively. The calculated insertion losses (IL) range between -0.7 dB to -1.8 dB within 1500 nm to 1600 nm wavelength range for all three output ports. The estimated crosstalk is less than -29.0 dB in all cases. The operation principle of the dual-mode (*TE0+TE1-in*) transmission is reported in section 4.2.1.

5.2 SMS fabrication and characterization

The SMS is fabricated through Applied Nanotools Inc. using a SOI wafer of 220 nm thick silicon device layer, 2.0 μm buried-oxide (BOX) layer, and 675 μm silicon handle layer [145]. The device is patterned using a 100 keV electron-beam-lithography (EBL), followed by an

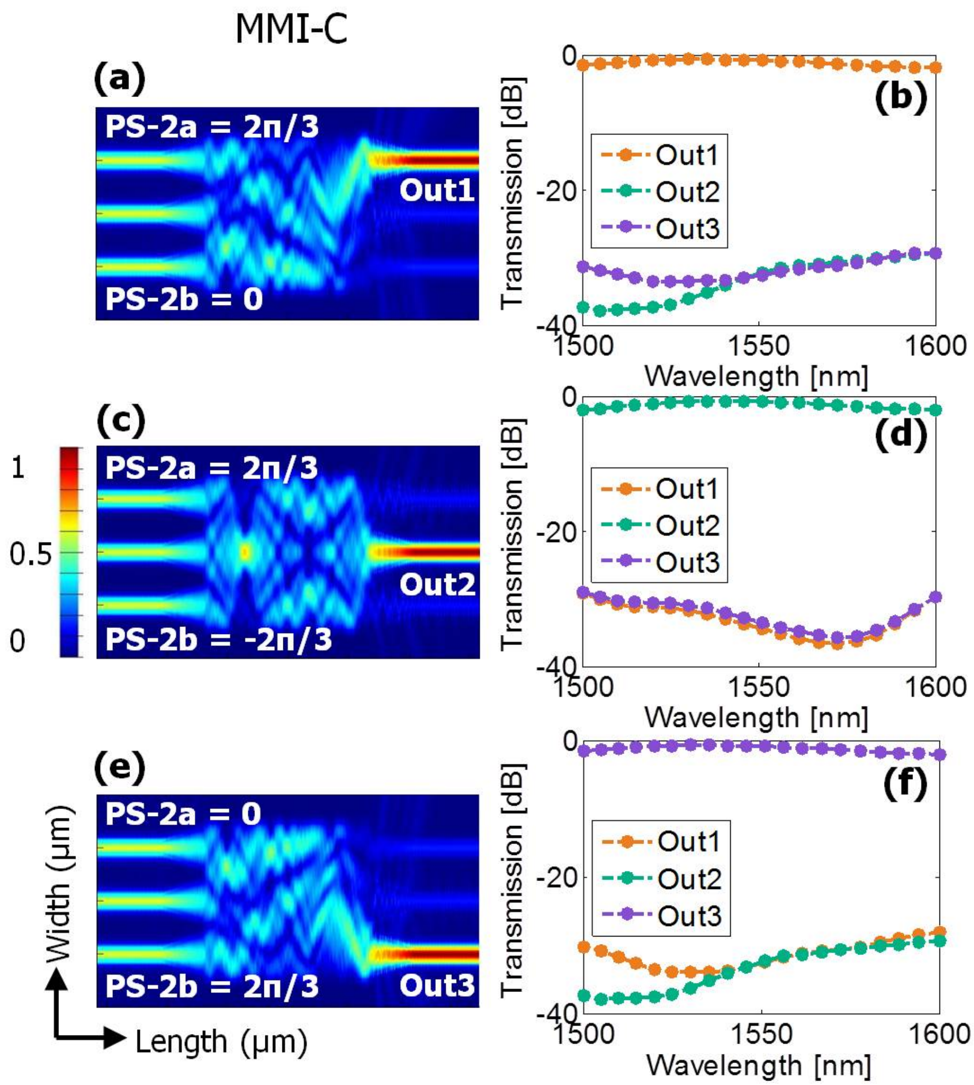

Figure 5.5 Simulated electric fields at 1550 nm (left) and calculated optical transmission as a function of wavelength (right) in MMI-C. The top (a, b), middle (c, d), and bottom (e, f) images represent optical transmissions in *Out1*, *Out2* and *Out3* output ports, respectively.

inductively coupled plasma-induced reactive ion etching (ICP-RIE) process. Then, a 2.2 μm silicon dioxide (SiO_2) is deposited using chemical vapor deposition (CVD) to protect and isolate the silicon device layer. On top of this oxide layer, 200 nm thin film of Ti/W alloy is deposited as high-resistance heater and 300 nm thin film of aluminum is deposited for the

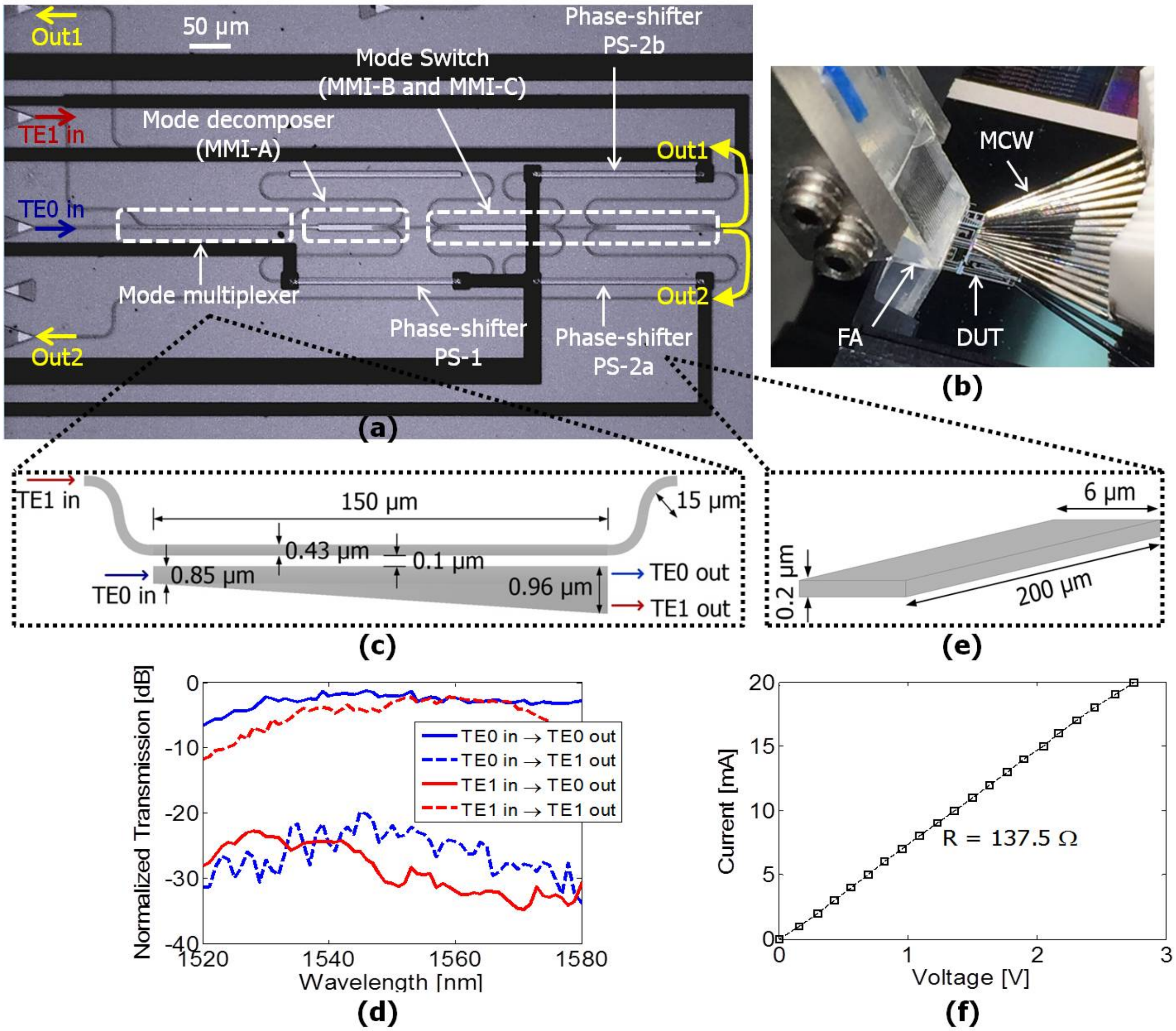

Figure 5.6 (a) Optical micrograph of the fabricated chip of the 2-mode SMS; (b) experimental test bed of the DC measurement showing a vertically coupled 8-fiber array (FA), a 15-pin multi-contact wedge (MCW) DC probe, and the silicon photonics SMS device under test (DUT); (c) schematic (top view) of the ADC based 2-mode multiplexer; (d) normalized optical transmission of the 2-mode multiplexer as a function of wavelength; (e) 3D schematic of the Ti/W metal heater phase shifter; and (f) measured current-voltage characteristic curve of the phase shifter

electrical routing using electron-beam evaporation. After metallization, a 300 nm SiO_2 layer is deposited as a protective layer for the heaters, which is etched away over the aluminum pads for electrical probing. A subset of the proposed SMS (Fig. 5.2) enabling reconfigurable switching of TE0 and TE1 modes between two output channels is experimentally measured. Simultaneous 2-mode switching between two parallel high-speed optical signals is also demonstrated. The characterization results of the 3-mode switch (3MS) are presented in chapter 6. An optical micrograph of the fabricated chip for the 2-mode switch is shown in Fig. 5.6(a). As the 2-mode switch needs only two output ports, the middle output port of the 3-mode switch (*Out2* in Fig. 5.2) is tapered down, and the upper and the lower output ports are denoted as *Out1* and *Out2*, respectively, as shown in Fig. 5.6(a).

Fig. 5.6(b) is an image of the experimental test bed showing a vertically coupled 8-fiber array (FA), a 15-port multi-contact wedge (MCW) DC probe, and the SOI device under test (DUT). The continuous wave (CW) optical input from a tunable C-band laser is polarization controlled for quasi-TE mode transmission, and then coupled to the DUT through surface grating couplers (GCs) of -6.5 dB fiber-to-chip coupling loss per GC. Heater bias voltages are applied from tunable DC power supplies, and the optical output power is measured by a power meter. An ADC based 2-mode multiplexer, shown in Fig. 5.6(c), is used for multiplexing the TE0 and the TE1 modes. The CW response of the 2-mode multiplexer is first measured. The normalized optical transmission of this mode-multiplexer as a function of wavelength is shown in Fig. 5.6(d). The broadband mode-multiplexer exhibits -1.8 dB IL and -22.0 dB crosstalk for the TE0 mode, and -2.7 dB IL and -30.8 dB crosstalk for the TE1 mode,

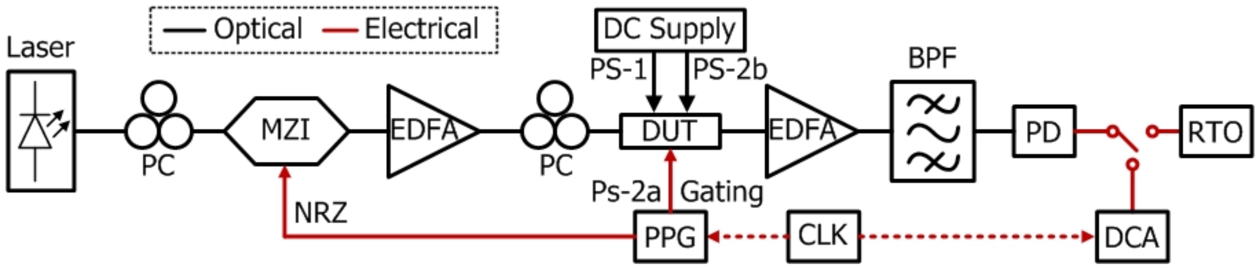

Figure 5.7 Experimental setup for the scalable multimode switch (SMS) measurement. The optical and electrical connections are shown as black and red lines, respectively. PC: polarization controller, MZI: Mach-Zehnder interferometer, EDFA: Erbium doped fiber amplifier, DUT: device under test, BPF: band-pass filter, PD: photodetector, RTO: real-time oscilloscope, DCA: digital communication analyzer, CLK: clock synthesizer, PPG: programmable pattern generator, NRZ: non-return-to-zero data signal.

respectively, within 1520 nm to 1580 nm wavelength range. The lower propagation constant ($\beta = 2\pi n_{eff}/\lambda$) of the TE1 mode due to the lower effective refractive index inside the channel waveguide is attributed to the higher IL for the TE1 mode. The electrical resistance of the phase shifter is measured on a 200 μm $\times$ 6 μm heater test structure (Fig. 5.6(e)), and shown in Fig. 5.6(f). The measured resistance is 137.5 Ω at room temperature.

For payload data transmission validation, the CW optical input from the laser is modulated by a 10 Gb/s NRZ PRBS31 signal, generated by a programmable pattern generator (PPG), shown in Fig. 5.7. The modulated and amplified signal is transmitted to the device under test (DUT), and then detected by a 46 GHz off-chip photoreceiver with a responsivity of 0.7 A/W after filtering out any out-of-band noise. The switch responses are recorded in real-time using a 350 MHz real-time oscilloscope (RTO) while recording the eye diagrams using a digital communication analyzer (DCA), which is synchronously triggered with the PPG by a 20 GHz clock synthesizer (CLK). A 18.6 kHz electrical square wave gating signal

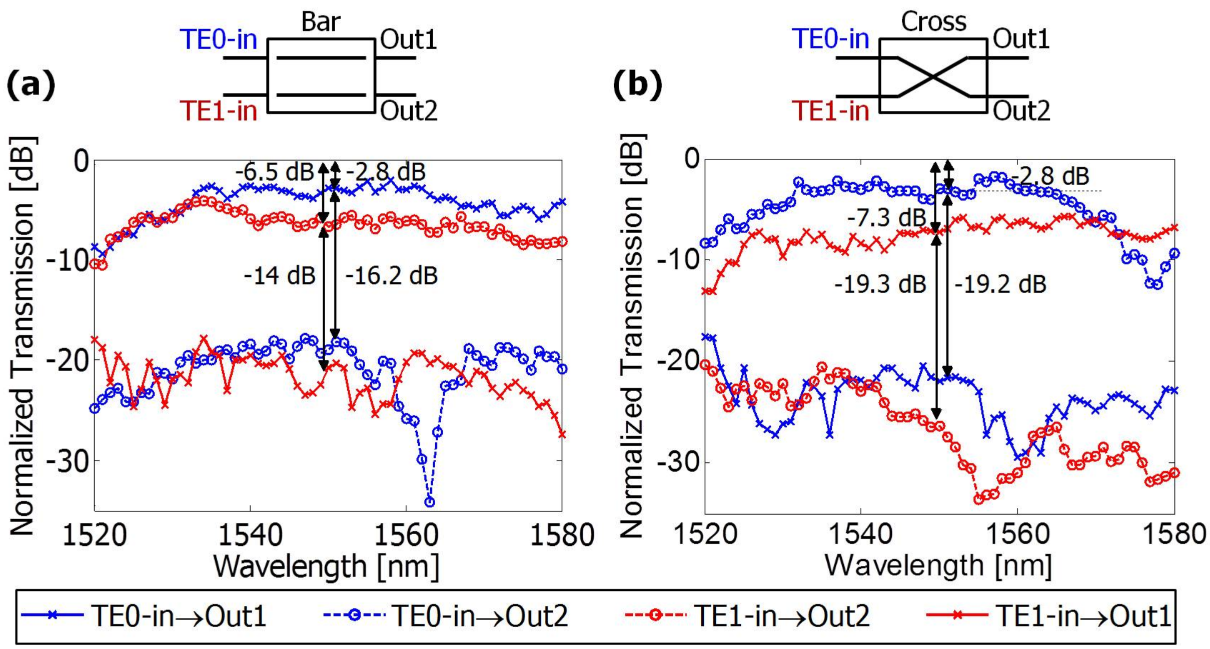

Figure 5.8 Normalized optical transmission of the SMS for the *TE0-in* and the *TE1-in* input modes in the (a) bar state and in the (b) cross state as a function of wavelength.

of 16 ns fall and rise time is applied to the PS-2a phase shifter, with the PS-1 and PS-2b phase shifters biased at fixed voltages to achieve the lowest IL in the transmitting channel.

5.2.1 Individual-mode switching

The normalized optical transmissions as a function of wavelength are shown in Fig. 5.8(a) for the bar state and in Fig. 5.8(b) for the cross state. In the bar state (Fig. 5.8(a)), the measured IL at 1550 nm are -2.8 dB for the TE0 input (*TE0-in*) and -6.5 dB for the TE1 input (*TE1-in*). The crosstalks are -16.2 dB and -14.0 dB for the *TE0-in* and the *TE1-in* inputs, respectively. In the cross state (Fig. 5.8(b)), the ILs in *TE0-in* and *TE1-in* inputs are -2.8 dB and -7.3 dB, respectively; and the crosstalks are -19.3 dB and -19.3 dB, respectively.

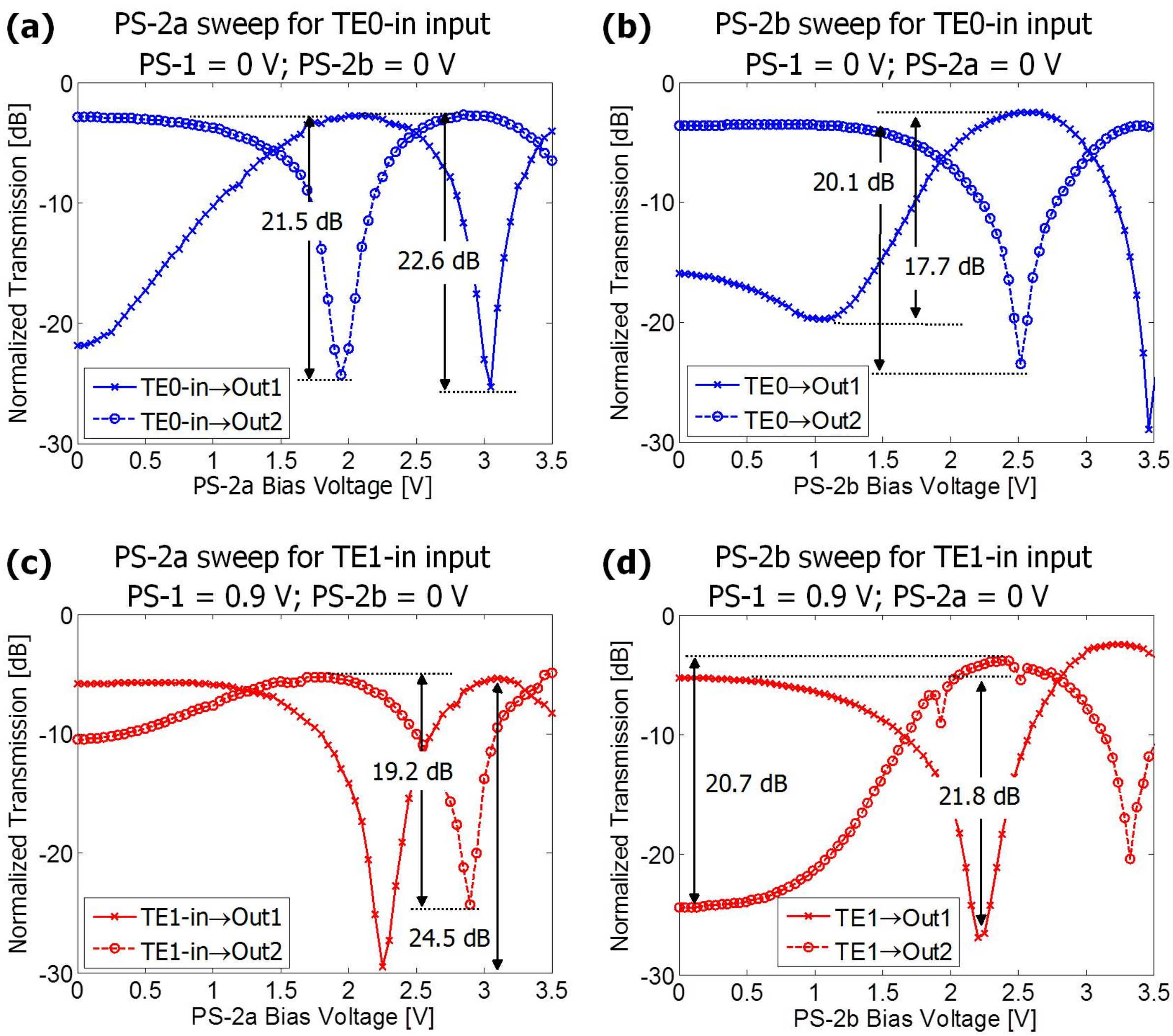

Figure 5.9 Normalized optical transmission of the SMS for *TE0-in* input as a function of (a) PS-2a and (b) PS-2b bias voltages from 0 V to 3.5 V when PS-1 = 0 V; (e) and (f) are the normalized transmission for *TE1-in* input as a function of PS-2a and PS-2b bias voltages, respectively, from 0 V to 3.5 V when PS-1 = 2.2 V.

These values include the IL and crosstalk of the 2-mode multiplexer, reported in Fig. 5.6(d). As different waveguide modes have different effective indices, and the thermo-optic phase-shift is a function of effective index of the individual modes, the phase-tuning of each mode requires different bias voltage in the heaters. The bias optimization of the PS-2a and the PS-2b phase shifters at 1560 nm from 0 V to 3.5 V are shown in Fig. 5.9(a-b) for the *TE0-in* input and in Fig. 5.9(c-d) for the *TE1-in* input, respectively. As the *TE0-in* input is not affected by the PS-1 phase shifter, this bias is fixed at 0 V. However, a 2.2 V bias is required in the PS-1 phase shifter for the phase matching of two fundamental components of the *TE1-in* input mode. The minimum switching ER for the *TE0-in* and the *TE1-in* inputs are 17.7 dB and 19.2 dB, respectively.

The switching responses for the *TE0-in* and *TE1-in* inputs are shown in Figs. 5.10(a) and (b), respectively. The *TE0-in* transmission exhibits 9.5 μs rise time and 7.4 μs fall time for the bar state (*TE0*$\rightarrow$*Out1*), and 9.8 μs rise time and 9.6 μs fall time for the cross state (*TE0*$\rightarrow$*Out2*). For the *TE1-in* transmission (Fig. 5.10(b)), the rise and fall times in the bar state (*TE1*$\rightarrow$*Out2*) are 7.0 μs and 8.3 μs, respectively. In the cross state (*TE1*$\rightarrow$*Out1*), the rise and fall times are 7.4 μs and 9.6 μs, respectively. Dynamic switching responses with payload data transmissions are shown next to each corresponding channel. The corresponding eye diagrams with measured electrical signal-to-noise ratios (SNRs) are shown next to each switching response. Open eyes are observed in all cases confirming the signal integrity with distortion free high-speed data transmission.

5.2.2 Dual-mode switching

The operation principle and experimental demonstration of simultaneous dual-mode transmission in an MMI based mode (de)multiplexer is discussed in section 4.2.1. For the recon-

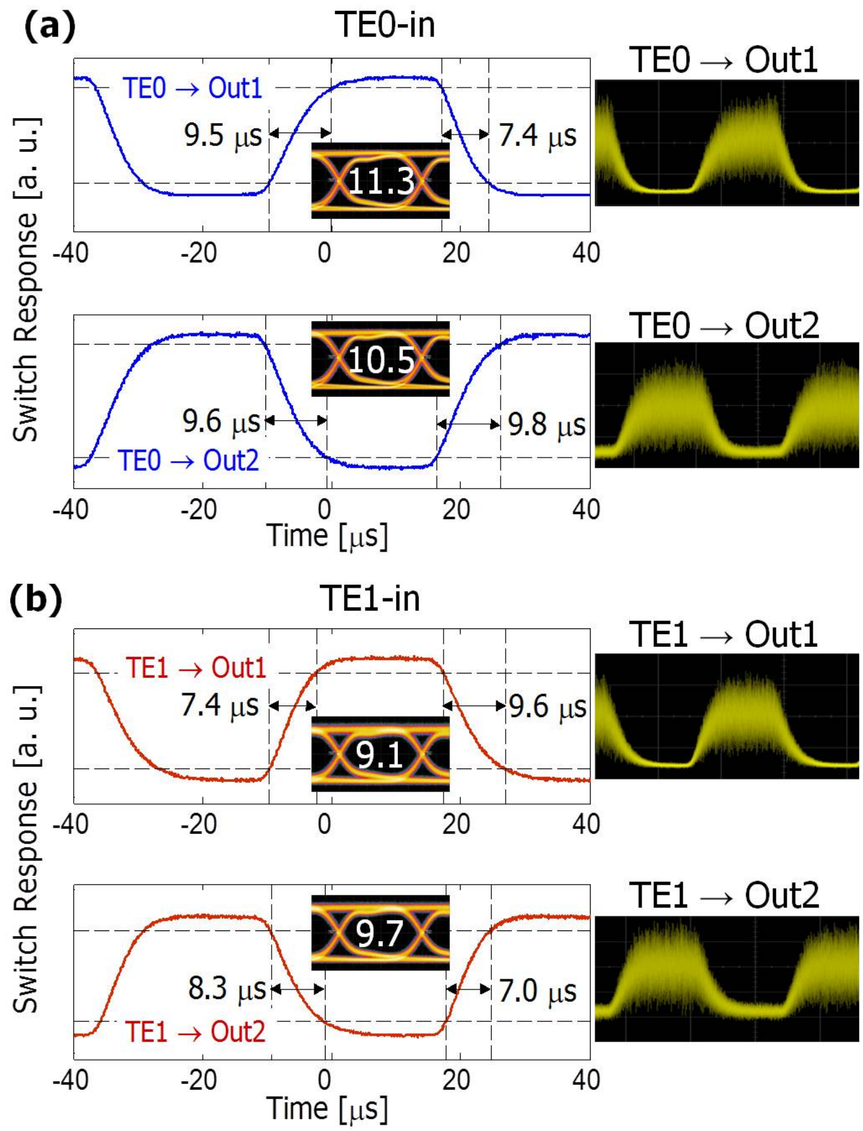

Figure 5.10 Measured on-off-keying switching of the MSS for the (a) *TE0-in*, and (b) *TE1-in* input modes at 1560 nm, showing the static (left) and the dynamic (right) responses. Insets of the static responses show the measured eye diagrams with the electrical SNRs.

figurable switching of two simultaneous TE modes (*TE0+TE1-in*), the PS-1 phase shifter is optimized so that the combined light beam of the *TE1-in* mode components always appear in the middle output port of MMI-B (Fig. 5.3(d)), and the power divided light beams from the *TE0-in* mode appear in the upper and the lower input ports of MMI-B. As each output beam is $2\pi/3$ out-of-phase with each other, by ensuring proper phase control using PS-2a and PS-2b phase shifters, dual-mode switching is achieved in the output of MMI-C. Although the ADC based mode multiplexer (Fig. 5.6(c)) can provide <-20 dB crosstalk over a large wavelength range (1520 nm-1580 nm) for individual-mode switching, the operating range reduces below 12 nm for the dual-mode transmission with a large (>-10 dB) crosstalk. However, the MMI based mode multiplexer, which is presented in section 4.2 [69], provides broadband response and sufficient crosstalk for simultaneous 2-mode switching. For this reason, the dual-mode (*TE0+TE1-in*) characterization is done using a MMI based mode multiplexer followed by the SMS of Fig. 5.2, with an additional 16.5 mW power consumption due to the phase tuning in the mode multiplexer. As the switching section i.e., SMS is the same in both structures, this modification does not limit the functionality of the SMS for dual-mode switching. Indeed, a design improvement is required for the ADC based mode multiplexer to demonstrate broadband and low crosstalk dual-mode transmission.

Normalized optical transmissions as a function of wavelength from 1520 nm to 1580 nm in dual-mode (*TE0+TE1-in*) are shown in Figs. 5.11(a) and (b) for *Out1* and *Out2* output ports, respectively. A -7.0 dB IL and -11.9 dB crosstalk are observed in the *Out1* output port, and -6.9 dB IL and -17.5 dB crosstalk are observer in the *Out2* output port. The normalized transmission of *TE0+TE1-in* input mode as a function of bias voltages of PS-2a and PS-2b phase shifters from 0 V to 4.0 V at 1560 nm are shown in Figs. 5.11(c) and (d), respectively. The lowest switching ER is 12.0 dB for the *TE0+TE1-in*$\rightarrow$*Out2* transmission. The dual-

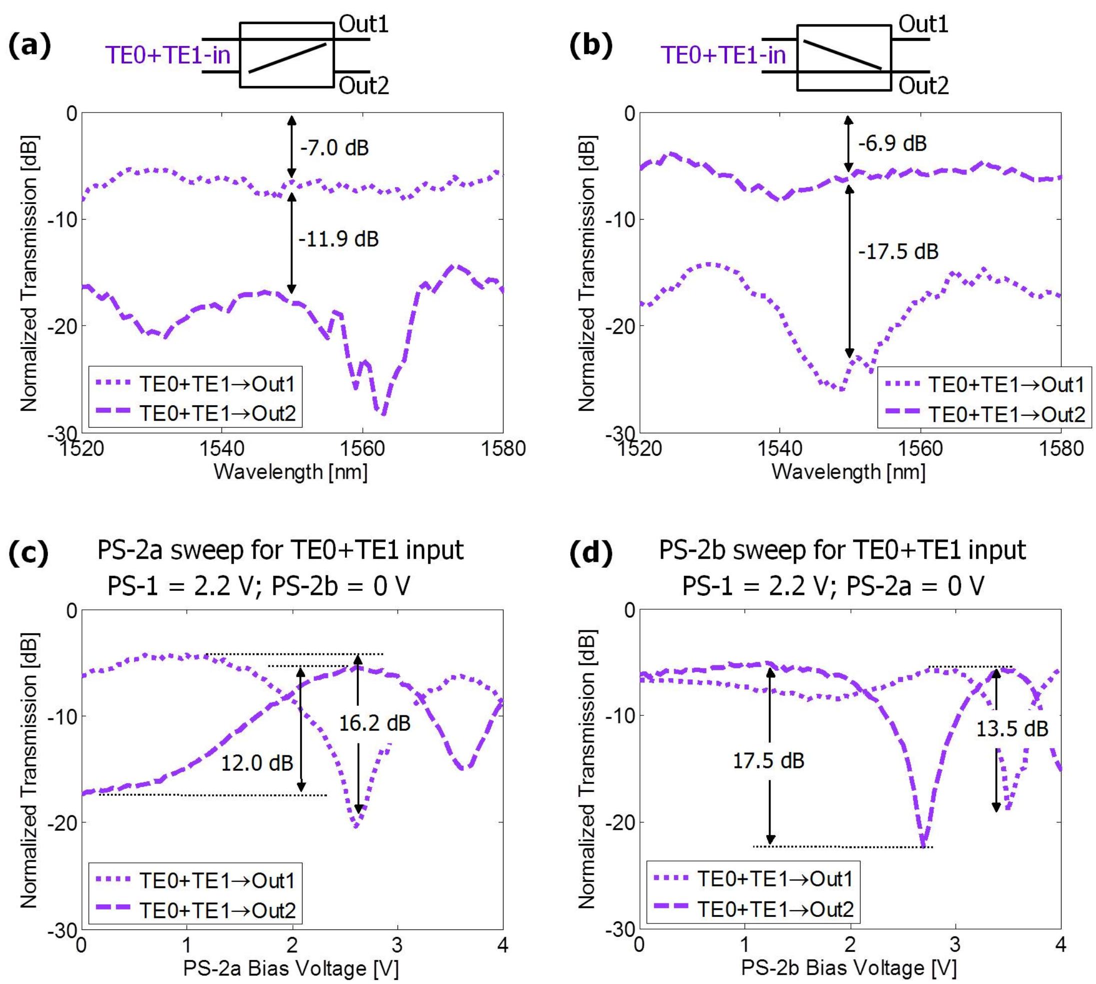

Figure 5.11 Normalized optical transmission of the SMS for the *TE0+TE1-in* input mode for the (a) *Out1* and the (b) *Out2* output ports as a function of wavelength; (c) and (d) are the normalized transmission for *TE0+TE1-in* input as a function of PS-2a and PS-2b bias voltages, respectively, from 0 V to 4.0 V when PS-1 = 2.2 V

mode switching performances, demonstrating $2{\times}10$ Gb/s aggregated bandwidth, are shown in Figs. 5.12(a) and (b) for the *Out1* and the *Out2* output ports, respectively. The slowest rise and fall times, in response to the 18.6 kHz square wave gating signal, are 7.1 μs and 7.6 μs, respectively. The eye height and the electrical SNR decrease in dual-mode compared to the individual-mode switching, which is attributed to the larger IL and crosstalk, observed

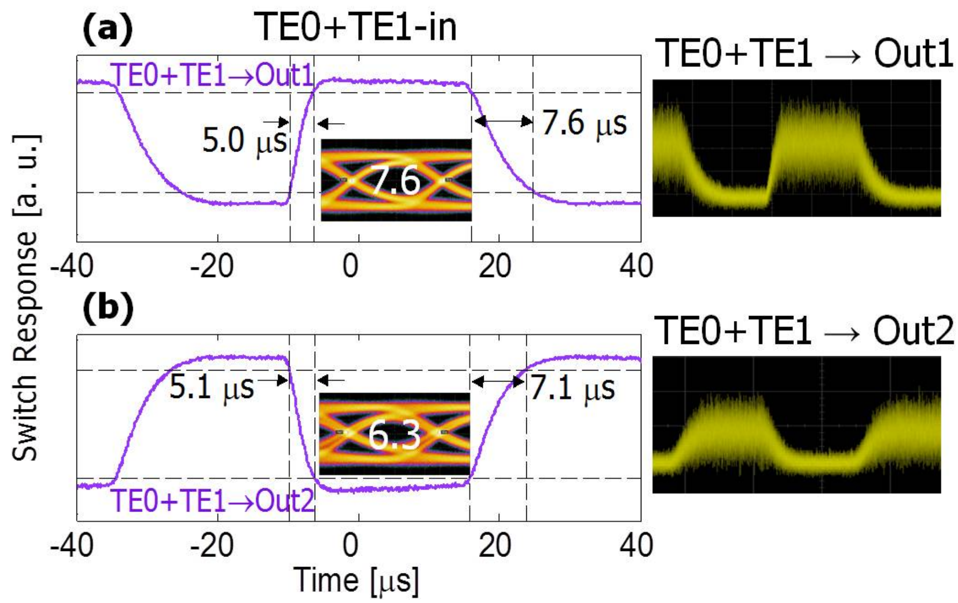

Figure 5.12 Measured on-off-keying switching of the MSS for the *TE0+TE1-in* input mode at 1560 nm, showing the static (left) and the dynamic (right) responses. Insets of the static responses show the measured eye diagrams with the electrical SNRs.

in Figs. 5 11(a) and (b). The dynamic switching is shown next to the static switching results. The CW measurement results are summarized in Table 5.1 and the switching performances are summarized in Table 5.2 for *TE0-in*, *TE1-in* and *TE0+TE1-in* input modes.

5.3 Discussion

5.3.1 Investigation of scalability

The SMS can be scaled up to switch higher order TE modes (e.g., TE3 and TE4) by carefully optimizing the width and length of the mode decomposer MMI (MMI-A) with additional output ports followed by the necessary phase shifters. However, the higher order modes will

Table 5.1 Insertion loss (IL), crosstalk, and average heater power consumption in the 2-mode SMS within 1520 nm and 1580 nm wavelength range

Input	Output	Insertion Loss (-dB)	Crosstalk (-dB)	Heater Power (mW)
TE0	Bar	2.0↔9.3	13.3↔30.7	48.3
	Cross	1.7↔12.3	9.2↔26.3	0
TE1	Bar	4.2↔10.5	7.5↔19.6	84.9
	Cross	5.6↔13.0	7.3↔27.0	126.3
TE0+TE1	Out1	5.3↔8.5	8.1↔20.6	98.2
	Out2	3.8↔9.7	8.9↔19.8	134.7

increase both the IL and the power consumption somewhat challenging its scalability. For example, the estimated IL and power consumption for the TE3 input mode in a similar 4-mode switch, calculated using numerical approximation, is -8.2 dB and 128 mW, respectively. In the proposed 4-mode SMS, as shown in Fig. 5.13(a), a 1×3 mode separator MMI of 7 μm width and 145.6 μm length reproduces the even TE0 and TE2 modes to its middle output port. The odd modes (i.e., TE1 and TE3) are divided into two components, and then mapped to the upper and the lower output ports. The TE1 mode is decomposed to TE0 components, and the TE3 mode is decomposed to TE1 components [92]. These decomposed mode components are phase-tuned and demultiplexed in the 2-mode (de)multiplexer. The demultiplexed modes are recombined in the 3 dB coupler stage followed by a 4×4 switching stage consisting of a 4×4 MMI and four phase shifters. There are eight phase shifters in this structure: each 2-mode switch has two phase shifters and the switching stage has four phase

Table 5.2 Switching performances for TE0, TE1 and TE0+TE1 input modes at 1560 nm

	Switching ER (dB)	Rise Time (μs)	Fall Time (μs)	Electrical SNR
TE0→Out1	17.7	9.5	7.4	11.0
TE0→Out2	20.1	9.8	9.6	10.5
TE1→Out1	21.8	7.4	9.6	9.1
TE1→Out2	19.2	7.0	8.3	9.7
TE0+TE1→Out1	5.0	7.6	8.3	7.6
TE0+TE1→Out2	7.1	5.1	8.3	6.3

shifters. The electric fields in the mode separator MMI for the first four TE mode inputs are shown in Fig. 5.13(b), demonstrating the capability of simultaneous 4-mode transmission.

5.3.2 Investigation of loss and power budget

To study the overall loss and power budget of the SMS, the 2-mode switch is compared with a mode selecting switch (MSS) allowing either the TE0 or TE1 mode transmission enabling a single-mode switch, reported in [70], and presented in section 4.3. As this MSS utilizes the same mode decomposer, cascaded MMI couplers and metal Ti/N phase shifter of similar phase tuning efficiency, the comparison is consistent and reasonable. The IL and power consumption of the proposed 3-mode switch, as shown in Fig. 5.2, is also considered in the scalability comparison. The measured average IL and average heater power for the mode selecting single-mode switch are previously reported to be -1.95 dB and 23.3 mW, respectively. The experimentally mesured average IL and average heater power for the 2-

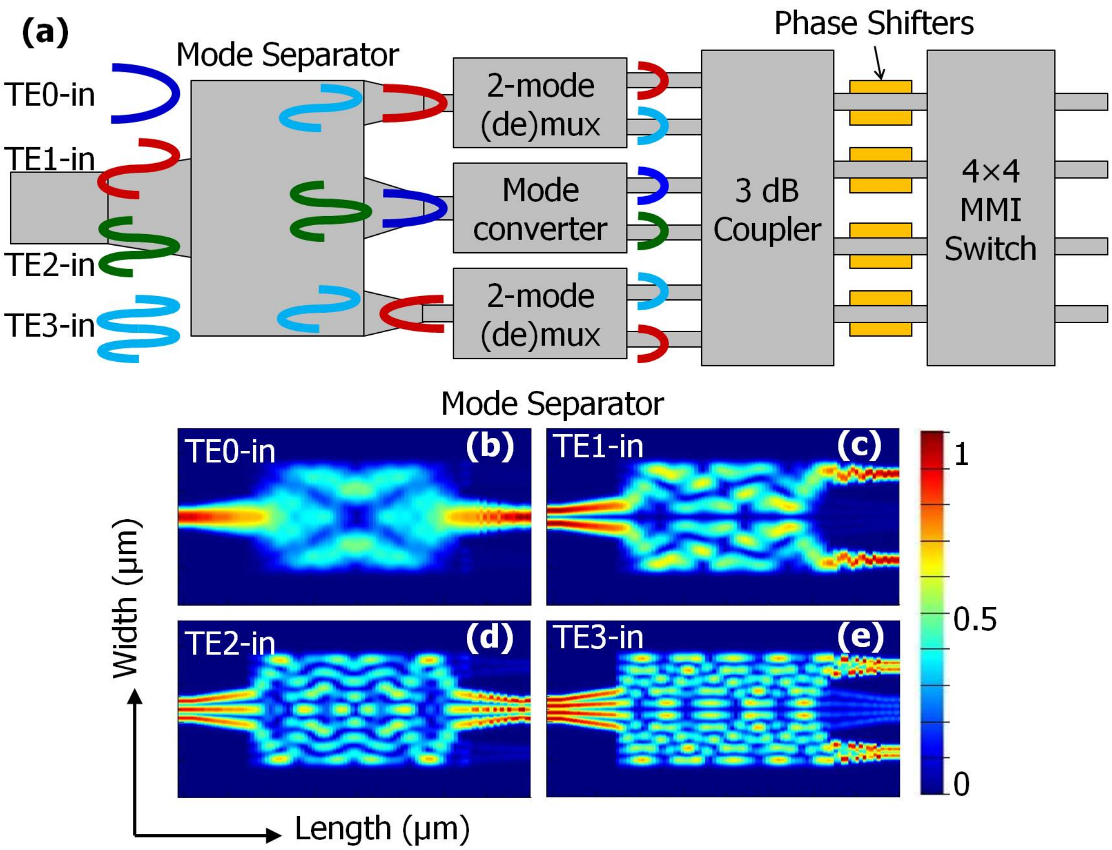

Figure 5.13 (a) Schematic block diagram of the 4-mode SMS for the switching of first four TE modes, i.e. TE0, TE1, TE2 and TE3; the simulated electric fields in the mode separator MMI are shown underneath for (b) *TE0-in*; (c) *TE1-in*; (d) *TE2-in*; and (e) *TE3-in* input modes.

mode SMS for the individual mode operation (i.e., *TE1-in* and *TE1-in*) are -6.8 dB and 65.0 mW, respectively in an ADC based SMS (see Table 5.1). As the dual-mode switching using ADC based mode multiplexer requires further optimization, this is not considered in the scalability study in Figs. 5.14(a) and (b). An initial characterization of the 3-mode switch demonstrates an average IL of -7.0 dB and an average heater power of 91.8 mW for the individual mode transmission. These values are plotted in Figs. 5.14(a) and (b) as a function of the number of TE modes. In a 2×2 MMI based single-mode MZI switch matrix, the overall IL from an input port to an output port can be estimated by simply adding up the ILs of each MMI along the I/O path, as each MMI is identically designed exhibiting similar IL and crosstalk. However, the dimensions of the MMIs, and the number of cascading stages change as the number of mode increases in the higher order SMS. Thus simulating the IL of a single MMI and adding it up for higher order mode switching is not an acceptable method. In Fig. 5.14(a), the IL of each MMI is estimated by EME simulation, and the S-parameters are extracted to build a circuit model in Lumerical's Interconnect [146]. The calculated ILs from this circuit level simulation are plotted in Fig. 5.14(a), along with the measured and fitted values. The higher ILs in the measured and the fitted plots than the simulated one is attributed to the higher scattering loss and wavelength sensitivity in the fabricated device, an impact of fabrication non-uniformity.

The power consumption per phase shifter is estimated through simulation, as reported in section 3.1 [136]. Based on the number of phase shifter used in 2-mode and 3-mode switches, we estimate the number of phase shifter required for higher order modes, and calculated the total heater power from simulation. The calculated average heater powers are plotted in Fig. 5.14(b), along with the fitted and measured values. The calculated and fitted powers are in good agreement. The slight variation arises from the uniform power increment in the calculated plot versus the change in heater power consumption for different phase shifters in the fabricated device. A -9.0 dB average IL and 193.0 mW average heater power is expected for a multimode switch capable of switching six TE modes. The heater power

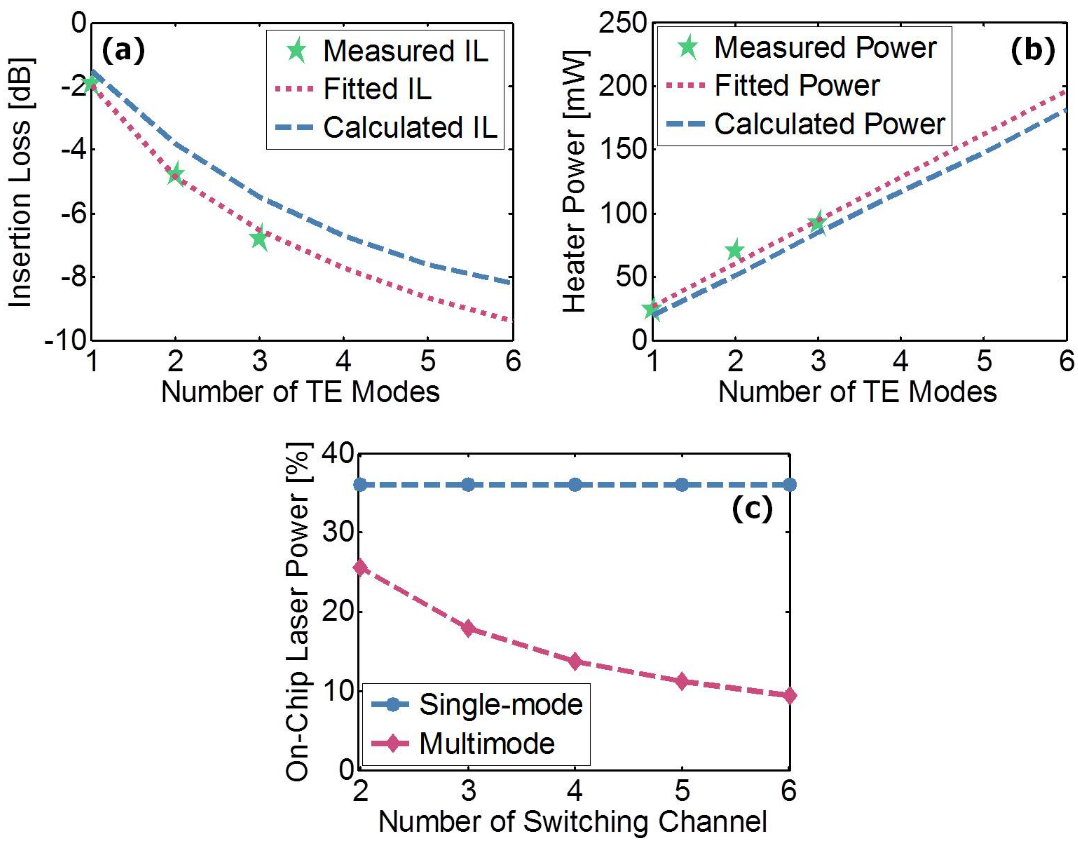

Figure 5.14 Measured (green star), fitted (pink dotted line) and simulated (blue dashed line) insertion loss (a) and average heater power (b) in the SMS as a function of number of propagating modes; (c) is the on-chip power fraction (%) of lasers with respect to total on-chip power in the single-mode (blue line) and the multimode (pink line) switches; the power consumption is calculated from the extrapolated heater powers from (b).

budget can be further improved by using resistive type doped silicon phase shifter [40] of 21 mW/π-shift, calculated in section 3.1, replacing the metal heater of 35.5 mW/π-shift, as measured in [70]. Using this resistive phase shifter, we achieved an on-chip energy efficiency of 1.55 pJ/bit, including the laser power, and a 2×10 Gb/s aggregated bandwidth in an RMDS based MDM photonics link. This type of phase shifter was not used to design the 2-mode and the 3-mode switch due to fabrication limitation. This estimation of energy efficiency is presented in section 4.4. As the same RMDS (MMI-A) can decompose TE0, TE1 and TE2 modes, a single device is required for the 2-mode switch and the 3-mode switch without increasing the footprint. The IL, device size and power consumption for more than 6 modes in single wavelength and single polarization (either TE or TM) is somewhat impractical and can be detrimental for error-free data transmission. For greater scalability, combined multiplexing techniques such as, WDM-MDM, MDM-PDM and WDM-MDM-PDM should be implemented.

5.3.3 Investigation of laser power fraction

As most of the power consumption of an integrated photonic switch is caused by the power of the laser [16], it is essential to evaluate an integrated switch in term of the on-chip laser power. The heater powers from Fig. 5.14(b) are used to calculate the on-chip power fraction (%) of the laser for single-mode and multimode switches of two to six switching channels, as shown in Fig. 5.14(c). A 2×2 MZI switch test structure with 2×2 MMI couplers and the same Ti/W metal heater phase shifter (as used in the SMS) is characterized as a single-mode 2-channel cross-bar switch. The measured average switching power of this 2×2 MZI switch is 40 mW. In the total on-chip power consumption of a switching channel, a 66 mW power of a 10 Gb/s directly modulated tunable on-chip VCSEL is included [147]. The on-chip power of a hybrid-integrated 40 Gb/s photoreceiver including a Ge-on-Si photodetector and a wire-bonded transimpedance amplifier (TIA) is reported to be 77 mW [148]. As the single-mode switching requires individual laser per switching channel, the ratio of laser power to the total on-chip power remains constant (38.1%) regardless of the number of channels, as shown in Fig. 5.14(c). On the other hand, a 3-channel multimode switch, for example, needs only one VCSEL providing equal optical power to each channel (3 mW optical output power). The power consumption by the laser for three-mode transmission is 79.7 mW including the 66 mW electrical driving power and 13.7 mW additional power to account for the higher optical output [149]. The laser wall-plug efficiency is not taken into account, as done in [16]. The receiver power and the heater power remain the same as the 3-channel single-mode switch. This estimates a laser power fraction of 19.8% in the 3-channel multimode switch, which is almost half the laser power fraction of a 3-channel single-mode switch of 36.1%. This allows large reduction in total on-chip power consumption in the multimode switch by saving approximately 27% energy in 2-channel switch up to 63% energy in the 6-channel switch compared to the corresponding single-mode switches. Thus, the proposed SMS can be used in the deployment of energy-efficient switch matrix in mode-division multiplexed integrated photonic systems. Indeed, the on-chip loss budget and the photodetector sensitivity have to be considered in this estimation, which needs detail investigation of power consumption analysis.

5.4 Summary

To summarize, in this chapter we presented a novel scalable multimode switch (SMS) using multimode interference couplers and Ti/W metal heater phase shifters for reconfigurable

MDM silicon photonic systems. To the best of our knowledge, this is the first demonstration of a SOI MDM switch that allows path-reconfigurable switching between first two (TE0 and TE1) or three (TE0, TE1 and TE2) TE modes using the same device, which can significantly improve the bandwidth density and power consumption. The 2-mode SMS exhibits $<$-14 dB crosstalk and $<$-7.3 dB IL in the individual-mode switching. The crosstalk and IL in the simultaneous dual-mode switching are $<$-11.9 dB and $<$-7.0 dB, respectively at 1550 nm. The measured switching ER is greater than 19.2 dB and 12.0 dB for individual-mode and dual-mode, respectively. Open and clear eye diagrams for all data channels demonstrate distortion-free data transmission with an aggregated bandwidth of 2×10 Gb/s. The rise and fall times are $<9.8\,\mu$s for the *TE0-in* input, $<9.7\,\mu$s for the *TE1-in* input, and $<7.6\,\mu$s for *TE0+TE1-in* input modes. The SMS can be scaled up for higher order mode switching by engineering the length and the width of the MMI couplers with more output ports and phase shifter stages. The power consumption analysis demonstrates the higher energy efficiency of the SMS than a single-mode MZI switch.

Chapter 6

3×10 Gb/s three-mode switch using 120° hybrid based unbalanced MZI

In this chapter, we demonstrate a three-mode switch (3MS) enabling reconfigurable switching of the first three transverse electric (TE) modes in the C-band using a 3×3 unbalanced MZI (UMZI) formed of a 120° optical hybrid MMI coupler. This is the experimental validation of the proposed SMS, presented in chapter 5, with 3-mode switching demonstrating greater scalability, higher aggregated bandwidth capacity and better energy efficiency. The results are published in [118]. The 3MS exploits the relative phase difference of the 120° optical hybrid to enable interferometric switching among the output ports of the UMZI. The 3MS is designed for TE polarization using 220 nm thick silicon channel waveguides, surrounded by 2.0 μm buried oxide (BOX) and 2.2 μm cladding layers of SiO_2. Ti/W thin film of 200 nm thickness and 6 μm width is deposited over the silicon waveguide as metal heater phase shifter. The waveguide widths for TE0, TE1 and TE2 mode propagations are optimized to be 0.5 μm, 1.0 μm and 1.45 μm, presented in section 5.1.1. An ADC based 3-mode multiplexer and MMI based mode decomposer, presented in section 5.1.2, are used to excite the TE0, TE1 and TE2 modes, and then demultiplex them into the fundamental mode components for phase-tuning. Titanium/tungsten (Ti/W) based thin film metal heaters are used as phase shifters. The 3MS exhibits less than 12.0 μs switching time and greater than 12.0 dB switching extinction ratio (ER) while dynamically switching high-speed non-return-to-zero (NRZ) 2^{31}-1 pseudo random bit sequence (PRBS31) optical payloads for an aggregated bandwidth of 30 Gb/s (3×10 Gb/s). An average power consumption of the heater of 94.8 mW is measured enabling energy-efficient 3-channel switching.

6.1 Design and working principle

The proposed three-mode switch, as shown in Fig. 6.1, is a similar design as Fig. 5.1 with bent MZI arms to reduce the device length. Three phase shifters, instead of two in the SMS, are required for the phase-tuning of three TE modes. Like the SMS, the 3MS consists of a tapered mode decomposer MMI (MMI-A) followed by the 3×3 unbalanced MZI (UMZI), comprised of two tapered cascaded MMIs (MMI-B and MMI-C). Four 200 μm long metal heaters are used as phase shifters. The PS-1a and the PS-1b phase shifters are used for tuning the relative phases of the decomposed mode components to optimize the insertion loss (IL) and the crosstalk. The PS-2a and the PS-2b phase shifters are used for applying

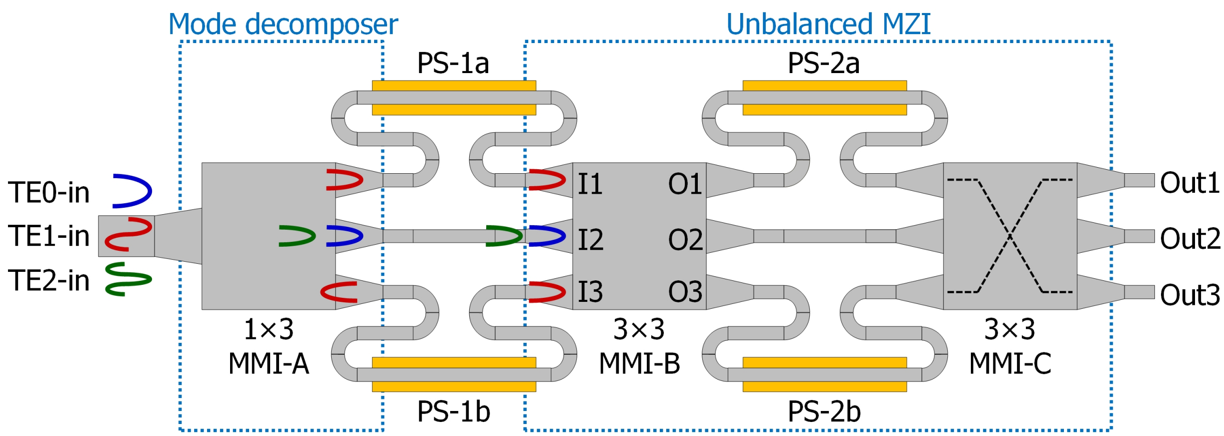

Figure 6.1 2D schematic of the three-mode switch (3MS) with three multimode inputs denoted as *TE0-in*, *TE1-in0*, and *TE2-in*; and three single mode outputs denoted as *Out1*, *Out2*, and *Out3*. the input ports of MMI-B (120° hybrid) are denoted as I1, I2 and I3, and its output ports are denoted as O1, O2 and O3.

required phase-shift in the UMZI to implement reconfigurable switching. The arms of the MMIs containing the phase shifters are bent to reduce the device footprint using 90° bends of 15 μm radii. The widths of all MMIs are 6 μm. The detail design and dimensions of the MMIs are discussed in section 4.1 and 5.1, and reported in [140].

The three TE modes, i.e., TE0, TE1 and TE2, are first multiplexed using a broadband ADC based mode multiplexer. The dimension and normalized optical transmission in this mode-multiplexer are shown in the experimental result section (section 6.2.1). After different optical modes are multiplexed in the mode-multiplexer, the mixed-mode signal is demultiplexed, and decomposed to its fundamental components in MMI-A, which is a reconfigurable multimode demultiplexer/switch (RMDS), as presented in chapter 4 [69]. The working principle of MMI-A is explained in section 5.1.2, and the simulated electric field profiles are shown in Fig. 5.3. The decomposed mode components for the *TE0-in*, *TE1-in* and *TE2-in* input modes are mapped to the MMI-A output ports as follows:

1. *TE0-in* input: the TE0 mode is mapped to the middle output port with 99.4% efficiency, but with an approximately 35% smaller mode-field diameter (MFD).

2. *TE1-in* input: the TE1 mode is divided into two fundamental components of opposite phases, and then mapped to the upper and lower output ports, each with 48.7% of the input power, with more than 97% overall efficiency.

3. *TE2-in* input: the TE2 mode is converted to the fundamental mode with 66.7% efficiency and mapped to the middle output port.

A longer MMI can potentially improve the conversion efficiency and reduce the scattering loss for the *TE2-in* input mode [90], but significantly increases the device length, hence, this method is avoided. Another approach is to use cascaded MRRs, but limiting the operating range of the 3MS due to the wavelength sensitivity of the micro-rings [107]. Using asymmetric directional couplers [77] and cascaded asymmetric Y-junctions [97] can improve the TE2→TE0 conversion efficiency. These devices, however, are more susceptible to fabrication process variation than MMIs. The outputs of the MMI-A are coupled to MMI-B's middle input port (I2) for the *TE0-in* and *TE2-in* input modes, and to the upper (I1) and the lower (I3) input ports for the *TE1-in* input mode, as shown in Fig. 5.3. The incoming light is equally distributed among the output ports of MMI-B for TE0 and TE2 modes. The imbalance in power splitting observed in the TE1 mode is compensated by the PS-2a and PS-2b phase shifters.

6.1.1 Design of the 3×3 unbalanced MZI

The 3×3 UMZI is designed analytically using the transfer matrix method (TMM) [150]. Although the more rigorous EME method can be used to generate the scattering matrix (S-matrix) utilizing bidirectional wave propagation, a large number of modes need to be considered to ensure the EME accuracy. This increases calculation time and complexity, especially in a phase sensitive device like the UMZI. Alternately, the TMM is attractive for its ability to decompose a complex structure into smaller components and calculate the transfer matrix of each component to directly generate the transmission spectrum of the complete device.

First, the analytical model is applied on a balanced 3×3 MZI to understand the switching in the ideal case. Then the transfer matrix of the UMZI is developed by compensating the optical phase delay associated with the bends and unbalanced arms. The characteristic equation for the output transmission of a balanced 3×3 MZI is defined as:

$$U_{out} = U \Phi U U_I \tag{6.1}$$

where U_I and U_{out} are the input and output matrices of the switch, U is the transfer matrix of the 3×3 general interference MMI (MMI-B and MMI-C), and Φ is the matrix of

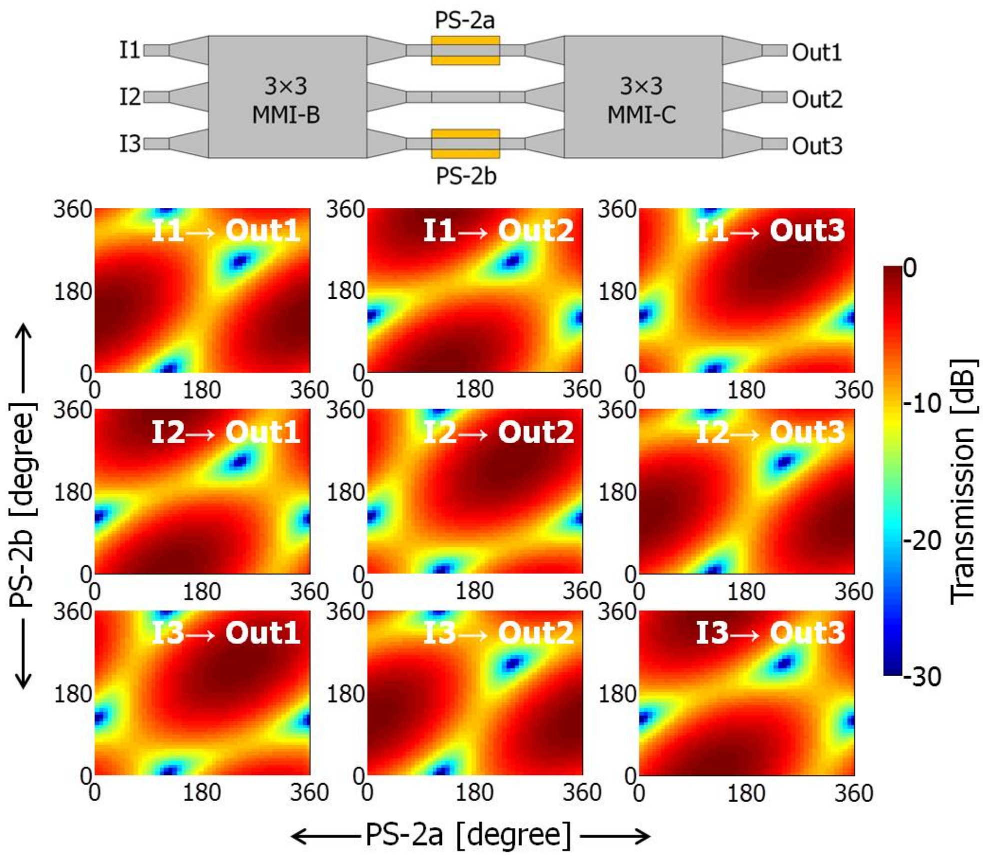

Figure 6.2 Simulated phase matrix of the 3×3 balanced MZI showing optical transmission for the inputs (I1, I2 and I3) to outputs (*Out1*, *Out2* and *Out3*) as a function of the combined phase-shifts of the PS-2a and the PS-2b phase shifters. The schematic of the 3×3 MZI is shown above.

the phase shifters. Using the amplitudes and phase-shifts of the 120° hybrid from Fig. 5.4, the transmission matrix of each input to each output of the 3×3 balanced MZI switch is generated in Matlab with respect to PS-2a and PS-2b phase shifters. This phase matrix is shown in Fig. 6.2. The applied phases for each individual transmission comply with the $2\pi/3$ phase requirement of the 120° hybrid. The optimal transmission maintains three groups of symmetry in phases I, II, III, which is summarized in Table 6.1.

In the UMZI, the optical path difference, ΔL, between the bent waveguides on the upper

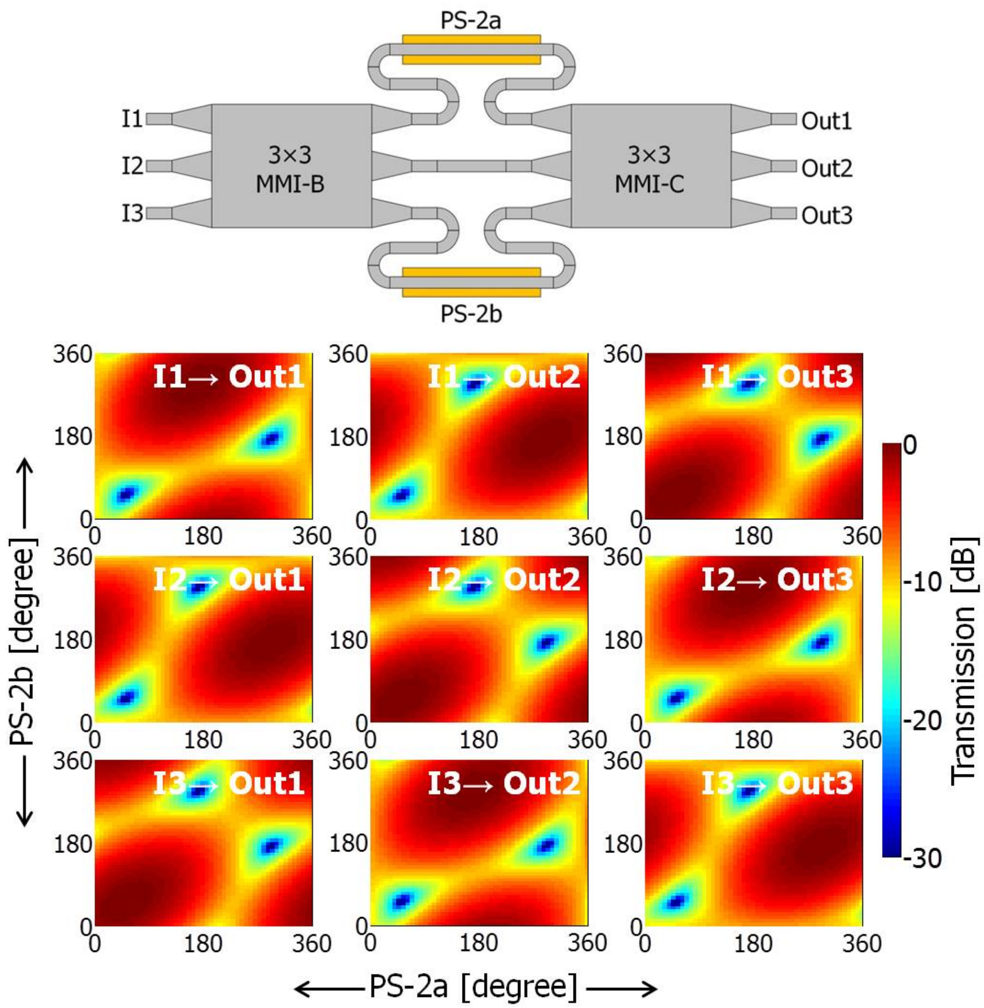

Figure 6.3 Simulated phase matrix of the 3×3 unbalanced MZI (UMZI) showing optical transmission for the inputs (I1, I2 and I3) to outputs (*Out1*, *Out2* and *Out3*) as a function of the combined phase-shifts of the PS-2a and the PS-2b phase shifters. The schematic of the 3×3 UMZI is shown above.

and the lower arms along the PS-2a and the PS-2b phase-shifters, and the smaller straight waveguide in the middle arm results in a phase difference of $\Delta\varphi$ defined by,

$$\Delta\varphi = \frac{2\pi n_{eff}}{\lambda}\Delta L \tag{6.2}$$

Table 6.1 Phase-symmetry in the 3×3 balanced MZI

Group	PS-2a phase	PS-2b phase	Transmission
I	0	$2\pi/3$	I1→Out1, I2→Out3, I3→Out2
II	$2\pi/3$	0	I1→Out2, I2→Out1, I3→Out3
III	$-2\pi/3$	$-2\pi/3$	I1→Out3, I2→Out2, I3→Out1

This phase difference is taken into account in the transfer matrix of the UMZI to determine the required phase shift for reconfigurable switching. The phase-compensated transfer function of the UMZI becomes:

$$U'_{out} = U\Phi' U U_I \tag{6.3}$$

where,

$$\Phi' = \Phi \pm \Delta\varphi \tag{6.4}$$

The three groups of symmetry I, II and III still applies in UMZI but the $2\pi/3$ phase requirement no longer exists. The transmission matrix of the UMZI with the corrected phase-shifts in PS-2a and the PS-2b is shown in Fig. 6.3. In the 3MS, the UMZI needs to be tuned according to these phases to achieve reconfigurable switching.

The UMZI transfer-matrix in the Eq. (6.6) is solved in Matlab by taking the phase-shifts of Fig. 6.3 into account. The solutions are plotted in Figs. 6.4(a) and 6.4(b) for I2 and (I1+I3) inputs, respectively. I2 input corresponds to the *TE0-in*/*TE2-in* input and (I1+I3) corresponds to the *TE1-in* input. The switching states are determined for the maximum

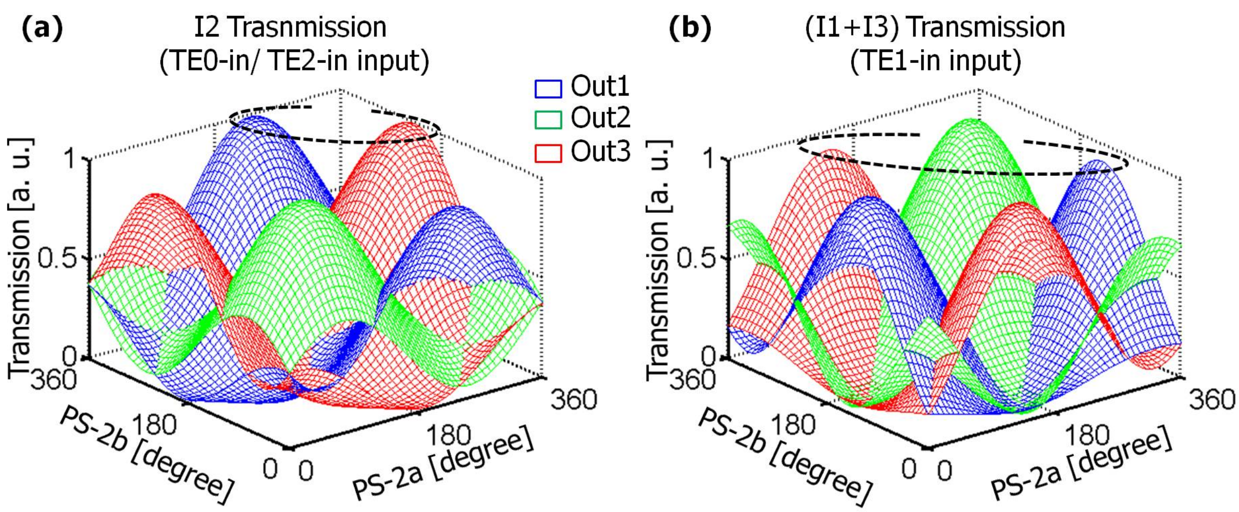

Figure 6.4 Solutions to the UMZI transfer matrix as a function of the combined phase-shifts of PS-2a and PS-2b phase shifters showing optical transmission and switching in all three output ports for (a) the I2 input port (*TE0-in* and *TE2-in* modes), and (b) the (I1+I3) input ports (*TE1-in* mode). The phase condition for the optimal transmission in each case is delimited by a black dotted line.

transmission in the expected output port and, at the same time, the minimum transmission in the crosstalk ports. The optimal transmissions are encircled by black dotted lines in each plot. For the I2 input condition (*TE0-in*/*TE2-in* input mode) in Fig. 6.4(a), switching occurs between *Out1* and *Out3* output ports with the optimal IL and crosstalk. From Fig. 6.3, the I2→Out2 switching should occur when PS-2a = PS-2b = 45°. As both phase shifters simultaneously need a non-zero phase-shift, the manual tuning of the test bed makes it difficult to achieve of the precise bias voltage needed. Moreover, the relative phase difference between the UMZI arms varies from the theoretical value due to the fabrication non-uniformity making phase tuning more challenging. An automated biasing technique is required to precisely tune both the phase shifters to enable switching at all output ports. This two-port switching will potentially limit the reconfigurability of the device but it is necessary for error-free data transmission. The phase condition required for three-port switching causes large crosstalk (more than 7% power leakage in each of the output ports), which will degrade the signal integrity and eye quality during high-speed data transmission. For the (I1+I3) input condition (*TE1-in* input mode) the optimal transmissions enable reconfigurable switching among all three output ports, as shown by the delimited dotted black line in Fig. 6.4(b).

6.2 Fabrication and characterization

The 3MS, similar to the SMS, is fabricated through Applied Nanotools Inc. in Alberta, Canada. The silicon device layer is patterned using a 100 keV electron-beam lithography (EBL) followed by an inductively coupled plasma-induced reactive ion etching (ICP-RIE) process. The Ti/W thin film as metal heater and aluminum thin film for metal routing are deposited using electron-beam evaporation. A thin (300 nm) SiO_2 passivation layer is deposited by chemical vapor deposition (CVD) to protect the metal layers. The optical micrograph of the fabricated chip is shown in Fig. 6.5(a). Surface grating couplers (GCs) are used to vertically couple the optical signal to and from the chip. The device footprint is estimated to be 0.157 mm^2 excluding the optical and electrical I/O ports.

The 3MS is first characterized with continuous wave (CW) optical input. The polarization controlled optical input from a tunable C-band laser is swept from 1520 nm to 1600 nm wavelength, and the output optical power is measured by an optical power meter. The IL

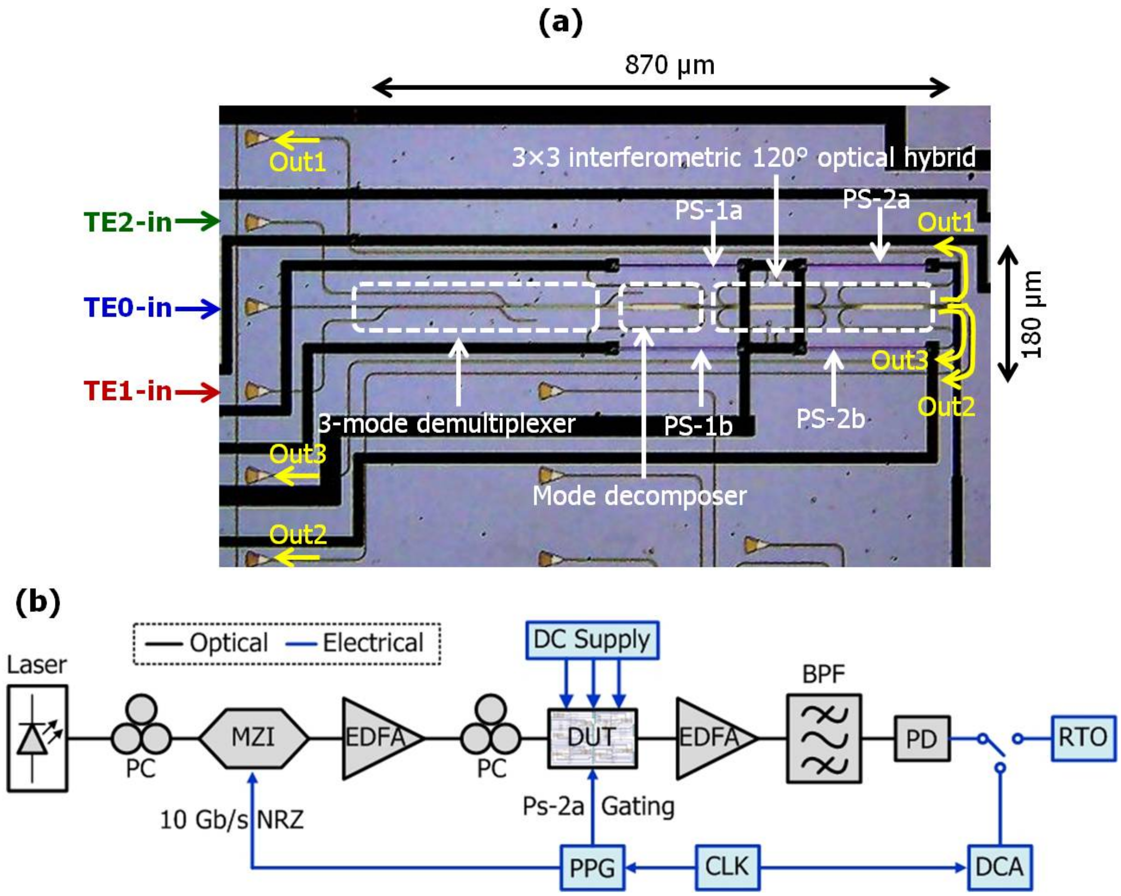

Figure 6.5 (a) Optical micrograph of the fabricated 3MS showing the complete device footprint excluding electrical pads; (b) experimental setup for the high-speed data transmission measurement for the 3MS. The optical and the electrical connections are shown as black and blue lines, respectively. PC: polarization controller; MZI: Mach-Zehnder interferometer modulator, EDFA: Erbium doped fiber amplifier, DUT: device under test, BPF: band-pass filter, PD: photodetector, RTO: real-time oscilloscope, DCA: digital communication analyzer, CLK: clock synthesizer, PPG: programmable pattern generator, NRZ: non-return-to-zero data signal.

and the crosstalk of the switch are minimized by tuning the DC bias voltages applied to the phase shifters. The experimental setup is similar to the one presented in section 5.2. Fig. 6.5(b) is the experimental setup for the high-speed data transmission measurement, where the 10 Gb/s NRZ PRBS31 payload, generated by a programmable patter generator

(PPG), modulates the CW optical signal. The modulated and amplified signal is transmitted through the device under test (DUT), and then detected by a 46 GHz off-chip photoreceiver of 0.7 A/W sensitivity. The eye diagrams are recorded by a digital communication analyzer (DCA). The dynamic switching response is recorded in real-time using a 350 MHz oscilloscope (RTO) by applying an 18.6 kHz electrical square wave gating signal from the PPG to the PS-2a phase shifter. The other phase shifters are biased at fixed voltages to achieve minimum IL and crosstalk.

6.2.1 Optical transmission characterization

A test structure of the ADC based 3-mode (de)multiplexer is first characterized with a CW optical input. Fig. 6.6(a) is the schematic of this ADC based mode (de)multiplexer and Figs. 6.6(b) - 6.6(d) are the normalized transmissions for the optical inputs for (de)multiplexing of TE0, TE1 and TE2 modes, respectively. As the optical I/Os, i.e., the GCs, are designed for single-mode coupling, the multiplexed modes need to be demultiplexed and converted to the fundamental modes to be detected at the output GCs. The IL varies from -0.3 dB to -2.9 dB for the TE0 mode, from -0.9 dB to -3.7 dB for the TE1 mode, and from -0.3 dB to -2.2 dB for the TE2 modes from 1520 nm to 1600 nm operating range. The worst crosstalks are -18.3 dB, -17.0 dB, and -19.6 dB for TE0, TE1 and TE2 modes, respectively.

The ADC based mode (de)multiplexer is characterized for one mode at a time to measure the IL and crosstalk for each incoming mode channel. In practice, this mode (de)multiplexer can be used for the excitation and simultaneous transmission of all three modes at a time

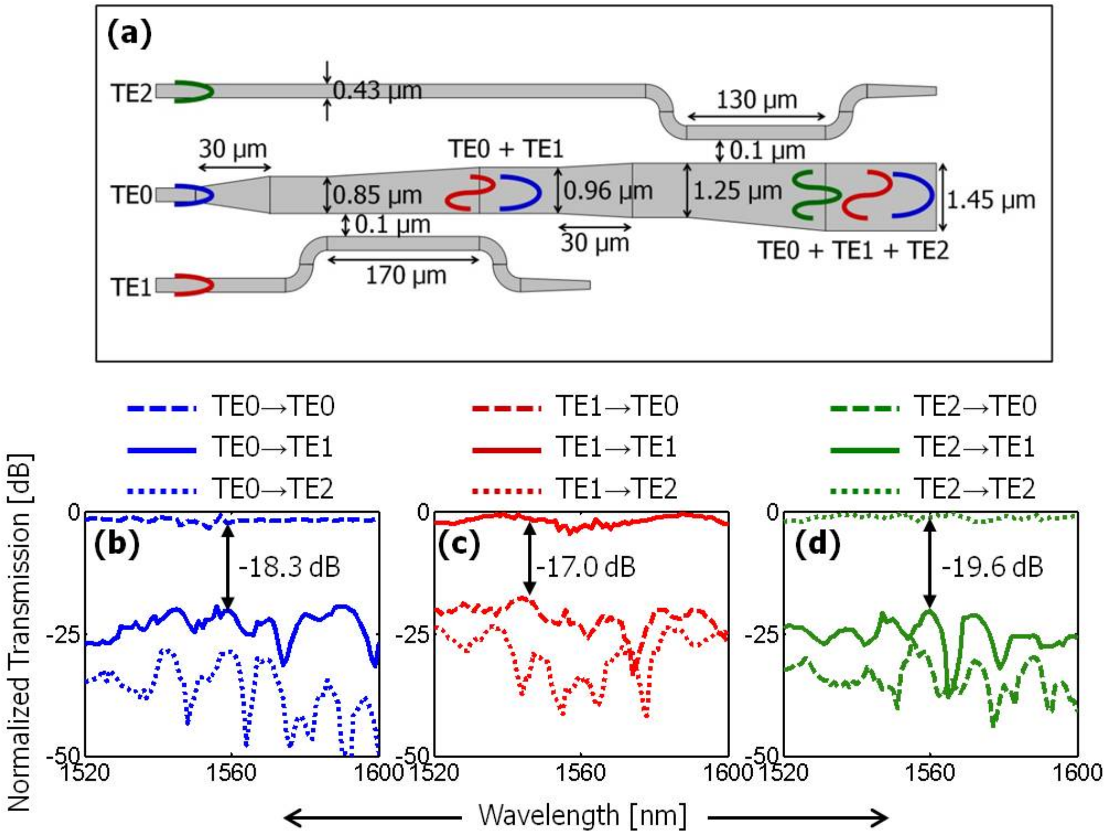

Figure 6.6 (a) 2D schematic of the ADC based 3-mode (de)multiplexer; the normalized optical transmissions of this (de)multiplexer as a function of wavelength are shown in (b) for the TE0 mode, in (c) for the TE1 mode and in (d) for the TE2 mode.

with an estimated maximum IL of -3.7 dB, and an estimated worst case crosstalk of -17.0 dB. The CW optical signal from a single tunable laser is divided by a 33% off-chip power splitter into three data channels, each of which is modulated by either off-chip or on-chip modulators. Indeed, the switching crosstalk in the 3×3 UMZI increases for three-mode simultaneous transmission. A design trade-off is necessary to achieve optimal performance from this high throughput 3MS.

The optical transmission in the 3MS, as a function of wavelength from 1520 nm to

1600 nm, normalized to a small waveguide test structure connecting two GCs, are shown in Fig. 6.7. *TE0-in*, *TE1-in* and *TE2-in* input modes are shown in the upper, middle and lower rows, respectively. The imbalance in effective optical path lengths between the spiral bent waveguide in the upper and the lower arms, and the straight waveguide in the middle arm of the UMZI results in an interferometric response with a small ($\sim$1.5 nm) free spectral range (FSR). This is different than the 2.5 nm FSR we presented in section 4.3.2 [70] due to the different lengths of the MZI arms. As this interference adds negligible variation in optical transmission ($<$ 0.5 dB), a larger sampling wavelength (1 nm) is taken for the experimental measurements. An extended FSR up to approximately 20 nm is observed, as shown in Figs. 6.7(a) - 6.7(f). This is attributed to the Vernier-effect induced FSR broadening caused by the multiple waveguide cavities formed of the upper arm (O1$\rightarrow$ PS-2a$\rightarrow$ O2) and the lower arm (O3$\rightarrow$ PS-2b$\rightarrow$ O2) [151, 152]. This extended FSR is not observed in our 2×2 based mode (de)multiplexer/switch presented in section 4.2, nor in the MSS presented in section 4.3 due to the absence of multiple cavities.

For the *TE0-in* input mode (Figs. 6.7(a) and 6.7(b)), the on-off switching occurs between the *Out1* and the *Out3* output ports, as explained in Fig. 6.4(a). The phase shifters are biased for the lowest crosstalk at 1560 nm. As the electro-optic modulator, used in the data transmission (Fig. 6.5(b)), is most stable at 1563.5 nm, the IL and the crosstalk are optimized around 1560 nm, which will facilitate data transmission measurement. For the *Out1* output port, the IL varies from -0.56 dB to -3.8 dB and the switching ER varies from 14.0 dB to 20.1 dB. For the *Out3* output port, the range of IL is -1.5 dB to -6.8 dB, and the range of

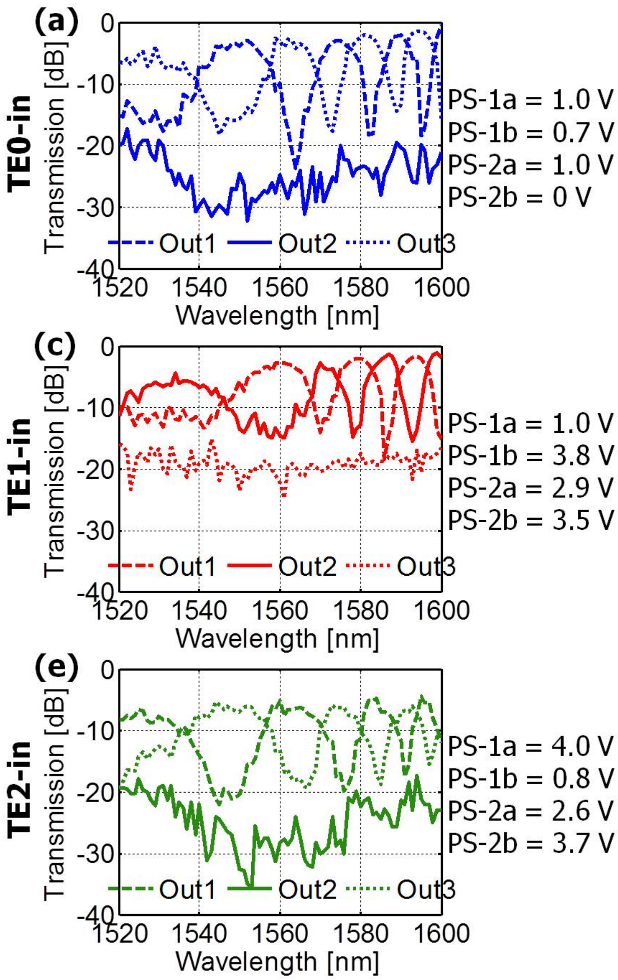

Figure 6.7 Normalized optical transmission as a function of wavelength showing reconfigurable switching between output ports for (a-b) *TE0-in*, (c-d) *TE1-in* and (e-f) *TE2-in* input modes. The applied bias voltages in each phase shifter are shown next to each transmission spectra.

switching ER is 12.7 dB to 18.2 dB, respectively. The crosstalk varies from -24.1 dB to -6.3 dB over the full spectrum.

As a multi-port interferometric device, the optical transmission in the UMZI is sensitive to the phase error and power imbalance in its arms, which imposes strict requirement of phase-control by precise tuning of bias voltages. A small imbalance in power splitting ratio and phase deviation due to fabrication non-uniformity can cause non-optimal switching resulting in higher IL and crosstalk, and lower ER [153, 154]. A look-up table based control algorithm can be used for the pre-compensation of the phase-error, which will potentially improve the switching performance [155]. The total heater power is estimated from the bias voltages to be 17.8 mW in Fig. 6.7(a) and 30.2 mW in Fig. 6.7(b).

The normalized transmissions for the *TE1-in* input mode are shown in Figs. 6.7(c) and 6.7(d) for the *Out1*/*Out2* switching and the *Out2*/*Out3* switching, respectively, with the estimated heater power to be 70.0 mW and 75.9 mW, respectively. The IL and switching ER at 1560 nm are less than -3.0 dB and greater than 12.3 dB. The worst case crosstalk at 1560 nm is -12.0 dB between *Out1* and *Out2* outputs in Fig. 6.7(c). For the *TE2-in* input mode, the IL and switching ER are less than -5.1 dB and greater than 11.6 dB at 1560 nm, respectively. The worst case crosstalk at 1560 nm is -10.8 dB in Fig. 6.7(f). The average IL and crosstalk increase in the *TE2-in* input mode. This is due to the imperfect TE2→TE0 conversion in MMI-A (Fig. 5.3(e)). Indeed, a design improvement is required to reduce this loss by optimizing the length, width, and I/O position of MMI-A. A design trade-off using an ADC based mode decomposer instead of the MMI-A can potentially reduce the loss at the cost of a large footprint. The average heater powers for the *TE2-in* input mode are 175.1 mW and 181.7 mW in Figs. 6.7(e) and 6.7(f), respectively. The overall average power consumption of the switch is 91.8 mW. The total power consumption can be significantly reduced by using a resistive phase-shifter of 21 mW/π-phase tuning efficiency, as presented in section 3.1 [136] .

6.2.2 Data transmission characterization

The switching performances in response to the gating signal (see Fig. 6.5(b)) applied at PS-2a phase shifter are shown in Figs. 6.8(a) and 6.8(b) for the *TE0-in* input mode, in Figs. 6.8(c) and 6.8(d) for *TE1-in* input mode, and in Figs. 6.8(e) and 6.8(f) for the *TE2-in* input mode. The rise time (10% to 90% increase in switching response) and the fall time (90% to 10% decrease in switching response) are estimated from the static switching without payload transmission. The slowest rise times in *TE0-in*, *TE1-in* and *TE2-in* inputs are 12.0 μs, 11.9 μs, and 11.1 μs, respectively. The slowest fall times are 10.0 μs, 10.9 μs, and 10.3 μs for *TE0-in*, *TE1-in* and *TE2-in* inputs, respectively. The switching time can be reduced to 2.0 μs by replacing the Ti/W heater with a doped silicon resistive heater [136], and further reduced to 2.5 ns using a p-i-n phase shifter [116]. The dynamic switching responses with 10 Gb/s NRZ PRBS31 optical payload are shown next to each channel. The higher crosstalk and lower switching ER in *TE2-in* input is attributed to the higher IL and crosstalk caused by the lower mode conversion efficiency, as shown in Figs. 6.8(e) and 6.8(f). The corresponding eye diagrams in each transmission are shown next to the switching responses. The electrical signal-to-noise ratios (SNRs) and peak-to-peak amplitudes are shown for each eye. Open eyes are observed in all cases confirming the signal integrity with distortion free high-speed data transmission. The switching performances of all three modes are summarized in Table 6.2.

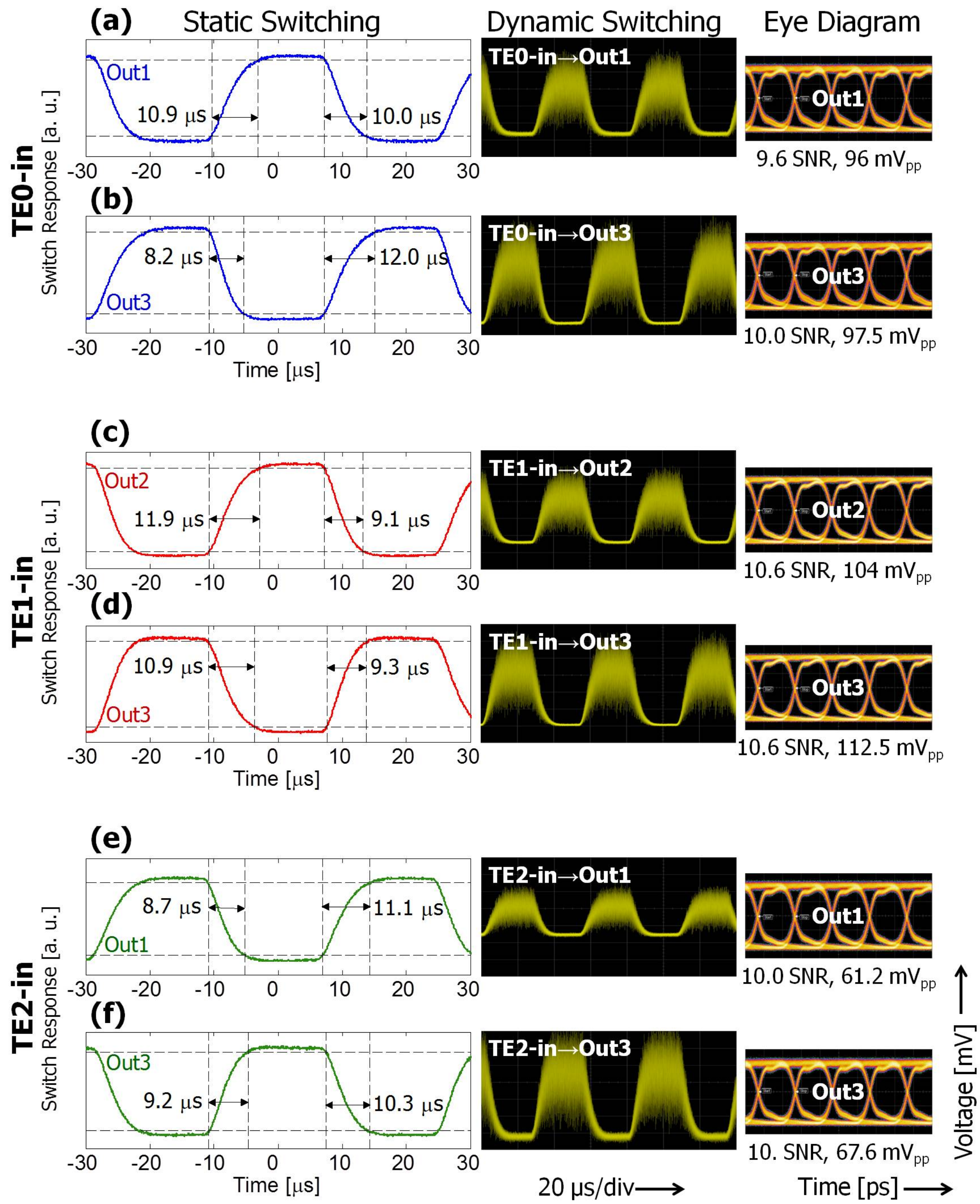

Figure 6.8 Measured static (left) and dynamic (middle) switching of the 3MS for (a-b) *TE0-in*, (c-d) *TE1-in* and (e-f) *TE2-in* input modes. The corresponding eye diagrams (right) with recorded electrical SNR and peak-to-peak voltage are shown next to each switching response.

Table 6.2 Switching performances for TE0, TE1 and TE2 input modes at 1560 nm

	Switching ER (dB)	Rise Time (μs)	Fall Time (μs)	Electrical SNR
TE0→Out1	14.0	10.9	10	9.6
TE0→Out3	12.7	8.2	12.0	10.0
TE1→Out2	12.3	11.9	9.1	10.6
TE1→Out3	12.5	10.9	9.3	10.6
TE3→Out1	12.0	8.7	11.1	10.0
TE3→Out3	11.6	9.2	10.3	10.0

6.2.3 Optical power budget

MDM silicon photonics switches offer energy advantage over the single-mode switches due to the use of a single laser to transmit optical signal over multiple guided modes. As most on-chip power is consumed by turning on the laser [16], using a single laser significantly improves the energy efficiency. The on-chip power budget of the 3MS is estimated considering the measured average IL of -7.0 dB from 1520 nm to 1600 nm operating range and the average heater power consumption of 94.8 mW. The measured fiber-to-chip optical coupling loss through the surface GCs is -13.2 dB from the input to the output. The total estimated on-chip power consumption is 237.8 mW including the transmitter and the receiver power consumptions. As low-power VCSELs with multimode fiber (MMF) and/or polymer waveguide are the current state-of-the art in silicon photonics short-reach interconnects [138], a 10 Gb/s directly modulated on-chip VCSEL of 66 mW driving power is considered as the

Table 6.3 Estimated power budget for the 3MS at 3×10 Gb/s aggregated bandwidth

Components	Electrical Power (mW)	Optical Loss (dB)
Direct Modulated VCSEL [156]	66	-
Photoreceiver [148]	77	-
Fiber-to-chip coupling	-	-13.2
3MS	94.8	-7.0
Total	237.8	-20.2
Energy efficiency	7.9 pJ/bit	

transmitter[156]. A 77 mW power consumption of a 40 Gb/s Ge-on-Si photodetector, wire-bonded to a transimpedance amplifier (TIA), is considered as receiver power [148]. Although simultaneous transmission and switching of three 10 Gb/s data signals over three modes is not demonstrated, we estimate the energy efficiency at 3×10 Gb/s, considering the maximum bandwidth capacity achievable by the device [157]. For the 3×10 Gb/s aggregated bandwidth, the energy efficiency of the 3MS is estimated to be 7.9 pJ/bit, including the driver power of the laser and the receiver. This can be significantly improved by using a more efficient phase shifter of resistive doped heater, and optimizing MMI-A for a higher TE0→TE2 conversion efficiency, which will lead the way towards the targeted attojoule optical interconnects [158]. The on-chip power budget is summarized in Table 6.3.

As presented in section 5.3.1, the 3MS can be scaled up to switch higher order TE modes (e.g., TE3 and TE4) by optimizing the mode decomposer MMI (MMI-A) with additional output ports followed by the necessary phase shifters. However, the higher order modes will increase both the IL and the power consumption leading to some scalability challenges. For example, the estimated IL and power consumption for the TE3 input mode in a similar 4-mode switch, calculated using numerical approximation, is -8.5 dB and 125 mW, respectively. The scalability can be further improved by introducing polarization division multiplexing (PDM) alongside MDM, where the MMIs are designed to be polarization insensitive such that the beat lengths for the TE and the TM polarizations are equal [159]. A hybrid WDM-MDM switch can be implemented by adding DWDM filters, before the ADC based mode (de)multiplexer, using either arrayed-waveguide gratings (AWGs) [105] or MRRs [78].

6.3 Summary

To summarize, we presented a silicon photonics three-mode switch using 120° optical hybrid based thermo-optically tuned 3×3 unbalanced MZI (UMZI). The design methodology of the UMZI is discussed. The proposed device enables reconfigurable switching of high-speed modulated signal over the first three TE modes (TE0, TE1, and TE2). Less than 12.0 μs switching time is demonstrated while switching 10 Gb/s NRZ PRBS31 optical payload, and open eye diagrams are recorded in each switching channel. The highest IL, lowest switching ER, and worst case crosstalk at 1560 nm are measured to be -5.1 dB, 12.3 dB, and -11 dB, respectively, for the *TE2-in* input mode. An average 91.8 mW overall power consumption is estimated. The same structure can be used for switching first two (TE0 and TE1) and first three (TE0, TE1 and TE2) TE modes offering footprint efficiency and higher bandwidth density. By carefully designing the width and length of the mode decomposer MMI (MMI-

A), and adding necessary phase shifters, the 3MS can be scaled up to accommodate higher order modes (e.g., TE3, TE4, etc.) without significant change in the device footprint. The proposed switch can be used in reconfigurable mode-division-multiplexed silicon photonics interconnects for the deployment of high throughput energy-efficient switch matrix.

Chapter 7

Future works

In this chapter, two possible research directions are discussed to further enhance and improve the investigation on SiP MDM interconnects. First an on-chip optical I/O interface is proposed using a SiP tunable vertical grating coupler (TVGC) for efficient opto-electronic co-packaging of silicon MDM PICs with off-chip active components, such as VCSELs and photodetectors. Next, a statistical investigation is proposed to study the fabrication non-uniformity in mode-multiplexed devices by structural parameter variation using different fabrication technologies. These proposals will help continue the promising works on MDM switches with more scopes of research contributions. Although the proposed devices are not directly related to the reconfigurable multimode switches, they are crucial for the commercialization and a broader understanding of MDM SiP systems. To reduce the overall power consumption of an on-chip MDM switch, the active elements, i.e., lasers and photodetectors should be placed close to SiP platform by 3D integration techniques such as, flip-chip bonding. In this context, a tunable and misalignment tolerant perfectly vertical surface grating coupler is necessary. Fabrication non-uniformity, which is a concern in any SiP system, affects the MDM devices in a larger scale as inter-modal crosstalk increases due to side-wall roughness and waveguide width variation. The higher crosstalk results in more BER power penalty. Therefore, it is imperative to investigate the proposed devices for a complete study of MDM SiP switches.

7.1 TVGC for low-loss opto-electronic packaging

Although SiP has been developed as a promising technology for optical interconnects, the indirect band gap of silicon limits its use as an optical source and detector by monolithic integration. An industry-suitable alternative is to heterogeneously integrate III-V lasers, such as DFBs, DBRs and VCSELs, on silicon photonics platform by wafer-bonding or flip-chip bonding. III-V components such as InP and InGaAs lasers and modulators can take advantage of lithographic precision and alignment accuracy allowing large-scale integration. The primary objective of this project is to develop a novel heterogeneous packaging solution for silicon photonics based optical interconnects for high-speed, robust, low power and densely packed opto-electronic systems. The conceptual diagram of an example of the proposed project is shown in Fig. 7.1.

The proposed design depicts the 2.5D integration of a silicon-based PIC co-packaged with a III-V active photonic devices and driver electronics on silicon interposer platform.

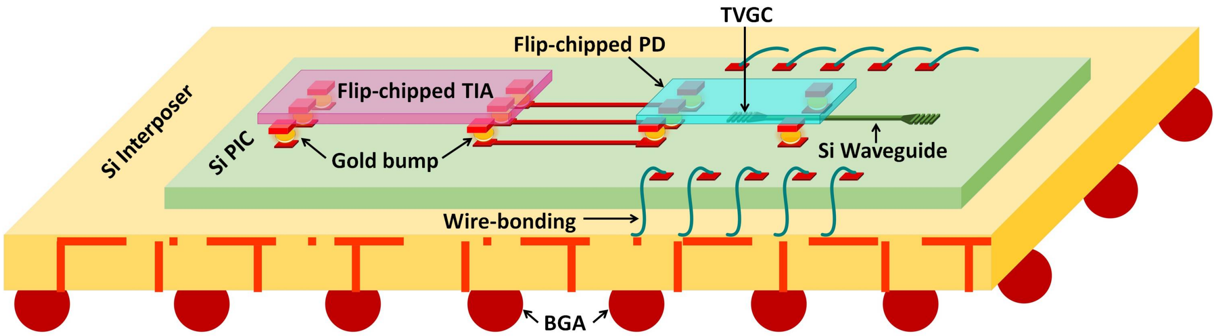

Figure 7.1 Conceptual diagram of the opto-electronic co-packaging of a SiP PIC and a photoreceiver including a III-V PD and a TIA, wire-bonded to the silicon interposer.

The PIC may consist of combinations of optical devices and systems including modulator, filter, arrayed waveguide gratings (AWG) and switch matrices, although in the schematic a strip waveguide is shown connecting two tunable vertical grating couplers (TVGC) for the sake of simplicity. The TVGC is a crucial component in this project as the off-chip source/detector needs perfectly aligned vertical free-space coupling. The III-V die can be VCSELs or quantum dot (QD) lasers, metal semiconductor metal (MSM) or QD avalanche photo diodes (APD), or semiconductor optical emplifiers (SOAs). The InP photodetector or VCSEL is flip-chip bonded through gold micro-bumps formed on metal pads which can be fabricated using metal evaporation and lift-off process or sputtering deposition. The electronic driver/TIA chip is also flip-chip bonded on the PIC for maintaining high-speed operation and to reduce the parasitic effect from wire-bonding.

For low power consumption, the integration of III-V devices must ensure efficient light coupling to and from the silicon waveguide. The packaged system should ensure lower coupling loss, higher alignment accuracy and tolerance, low power consumption and high-

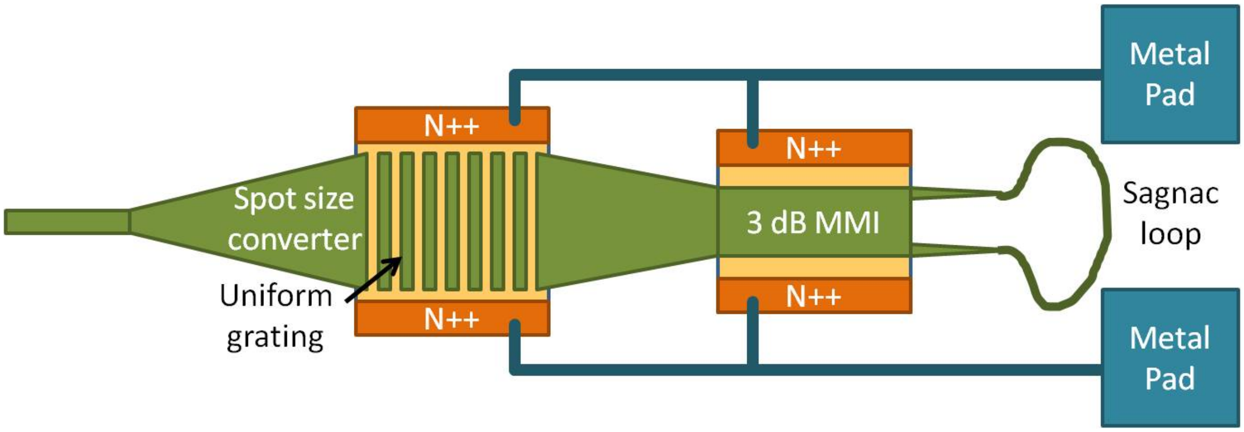

Figure 7.2 Schematic (top view) of the TVGC

speed operation. With this goal in mind, we propose a tunable vertical grating coupler (TVGC) formed of a uniform grating, two spot-size converters, and a 3 dB 1×2 MMI coupler with an integrated Sagnac loop mirror [160]. A schematic of this device is shown in Fig 7.2. The design methodology of the vertical grating is similar to [161], where two different oxide etchings are used to form a DBR back mirror reducing the high back reflection. We replace this DBR mirror by the MMI based Sagnac loop, and take advantage of the single oxide etching avoiding fabrication complexity. Both the grating and the MMI are designed using silicon rib waveguides with N++ doped silicon slabs to provide TO phase-shift. This allows longitudinal angle tuning capability for the TVGC by adjusting the temperature dependent wavelength shift, following the relation [162]:

$$sin(\theta) = \frac{n_{eff}\Lambda - \lambda_0}{\Lambda} \tag{7.1}$$

where n_{eff} is the effective index of the waveguide within the grating, Λ is the grating pitch, and λ_0 is the free-space wavelength.

7.2 Fabrication non-uniformity in SiP MDM interconnects

As the device size is continuously shrinking in SiP PICs, fabrication variability and non-uniformity are becoming more and more challenging to deal with. Both systematic and random variability can cause PIC performance variation jeopardizing system malfunctioning. Although both regular and random variabilities are possible to limit below 3% [163], in a phase sensitive device like mode demultiplexer or mode switch, this variation can be detrimental. The ideally non-overlapping modes in a multimode bus waveguide fail to obey the characteristic nature of orthogonality in the presence of random non-uniformity in the waveguide side-walls and surface. These non-uniformities, usually a result of inefficient etching, may not entirely kill the MDM device operations but impose challenges in mitigating crosstalk [164].

We propose to study the effect of fabrication non-uniformity on SiP MDM devices in both by systematic statistical investigation. Both macro-scale and micro-scale analysis should be done for a detail understanding of process variation induced crosstalk. In macro-scale, numerous devices should be designed with variable widths and lengths of the MDM devices, such as ADCs, tapers, MMIs and multimode bus waveguides in different fabrication platforms, i.e., Ebeam lithography and deep ultra-violate (DUV) lithography. For the micro-analysis, random bumps and valleys in the waveguide side-walls are mimicked in the PIC by inten-

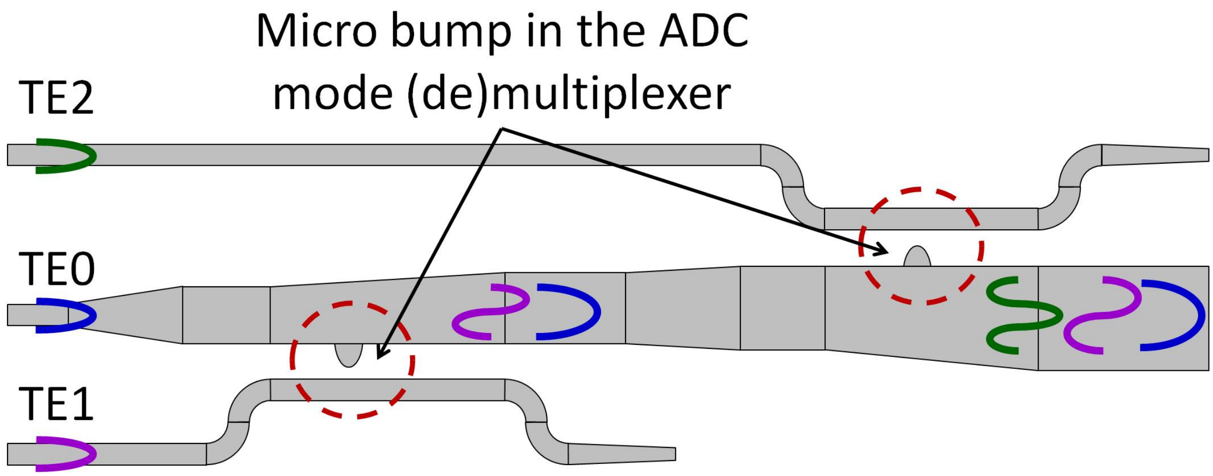

Figure 7.3 Schematic of a three-mode ADC based (de)multiplexer with intentionally added micro bumps in the coupler regions.

tionally adding small circles of variable radii. A trend analysis will be done on these devices for over 300 iterations, as in [165], to develop a statistical map over the full SOI wafer for each fabrication process. A useful tool for this type of study is Monte-Carlo analysis, which allows to develop a variance map for one or more parameter variation of the PIC and the MDM system. A theoretical model will be proposed for the fabrication non-uniformity in SiP MDM devices, as done in [122].

7.3 Summary

In this chapter, we discussed two crucial challenges in SiP as well as MDM interconnects namely, packaging and fabrication variability. We proposed possible methodologies to further investigate on these challenges to develop more robust and more efficient chip prototypes. The scope and functionality of silicon interposer as a mid-board carrier needs to be tested as a new technology paradigm. As the loss and crosstalk in the multimode propagation increase with the number of waveguide modes, the potential of scalable MDM interconnects becomes limited. A detail study towards mitigating crosstalk by proper control of process variation will lead to low-loss high-efficient MDM systems.

Chapter 8

Conclusion

In this thesis, four SiP switches are presented using different types of TO phase shifters for short reach data center applications. Design, simulation, experimental validation, and power budget analysis are included in each case. The need for optical interconnects in future Zetta scale data centers has been discussed. Mode-division-multiplexing has been proposed as a viable alternative to conventional WDM for high throughput low-power on-board and on-chip systems in data intensive computing environments.

In chapter 2, the theory of thermo-optic effect is described with examples of various TO phase shifters. Their applications in reported literatures are mentioned. Operation principle of the SiP switch building blocks are discussed. A detail discussion is added on mode-division-multiplexing with the fundamental concept of waveguide modes. Applications and research progress of SiP MDM interconnects are detailed.

In chapter 3, a rearrangable non-blocking O-band 4×4 Beneš switch is experimentally demonstrated. The energy consumption analysis demonstrated promising performance of the doped silicon phase shifter compared to over-clad metal heaters. A 2.4 μs switching speed and a 1.9 dB power penalty is measured for 10^{-12} BER, which remains within the already reported range. However, the relatively higher crosstalk is likely to deteriorate non-blocking application of data transmission.

The capacity limitation of SiP switches is addressed in chapter 4 by introducing a reconfigurable multimode (de)multiplexer/switch (RMDS). This novel component exhibits low-loss low-crosstalk data transmission by exploiting mode diversity - the basis of MDM interconnects. The versatility of RMDS is demonstrated by its utilization in both a (de)multiplexer and a mode selecting switch, which opens up immense research scope on its application, design improvement, scalability and prototyping. An aggregated bandwidth of 2×10 Gb/s is experimentally demonstrated with 2.8 dB BER power penalty for the mode (de)multiplexer, and the switching time is measured to be 10.9 μs. However, the higher IL for the TE1 mode switching remains a concern, which should be reduced by proper design of the MMIs and phase shifters. Also, the energy per bit matrix is only estimated from previously reported results, and needs experimental validation.

The structural dimension of the mode decomposer MMI is significantly improved in the scalable mode switch, presented in chapter 5. Rigorous numerical analysis and parameter optimization are used to explore the scalability of the design. Both individual-mode and simultaneous two-mode switching is experimentally presented with 9.8 μs switching time constant and $<$ - 11.9 dB crosstalk. The IL is improved to be -7.3 dB. Detail analysis on scalability, power consumption and IL demonstrate potential energy advantage by saving 63% on-chip laser power in a 6-channel multimode switch relative to a similar single-mode switch. The power consumption can be further improved by more efficient phase shifter. The scalability potential needs experimental validation by designing and testing the proposed four-mode switch.

Chapter 6 presents a three-mode switch (3MS) realized using the same SMS of chapter 5. This proves the footprint efficiency of this device enabling path reconfigurable switching of either first two or first three TE modes. The relative phase-difference of the outputs of a 120° optical hybrid is exploited to enable simultaneous three-mode switching with 91.8 mW average heater power consumption and 12.0 μs switching time constant. A worst case crosstalk is measured to be -11.0 dB at 1550 nm. Polarization diversity can further increase the bandwidth capacity of this device, implemented by polarization insensitive MMIs or adding polarization splitter-rotator in the inputs. Introducing MRR based wavelength filters with the 3MS can implement a WDM-MDM-PDM switch for even greater bandwidth capacity.

Finally, some future research directions are presented in chapter 7. A tunable vertical grating coupler is proposed to facilitate the packaging challenge of SiP interconnects. A tunable MMI based integrated Sagnac loop is used as a 100% reflective mirror reducing back reflection. Wavelength tunability is introduced by doping the partially etched silicon layer of the grating area for thermo-optic phase-shift. A systematic study on fabrication non-uniformity of SiP MDM devices is proposed. The scopes and challenges of this investigation is discussed as a research roadmap towards energy-efficient MDM interconnects.

Bibliography

[1] "Cisco global cloud index: Forecast and methodology, 2016–2021," https://www.cisco.com/c/en/us/solutions/collateral/service-provider/global-cloud-index-gci/white-paper-c11-738085.html, Cisco Systems, Tech. Rep., 2017, accessed: November-19-2018.

[2] M. D. Avgerinou, P. Bertoldi, and L. Castellazzi, "Trends in data centre energy consumption under the european code of conduct for data centre energy efficiency," *Energies*, vol. 10, no. 10, p. 1470, September 2017.

[3] W. Dargie, D. Schoeniger, L. Szilagyi, X. An, R. Henker, and F. Ellinger, "A highly adaptive and energy-efficient optical interconnect for on-board server communications," in *2017 26th International Conference on Computer Communication and Networks (ICCCN)*, July 2017, pp. 1–8.

[4] D. A. B. Miller, "Device requirements for optical interconnects to silicon chips," *Proceedings of the IEEE*, vol. 97, no. 7, pp. 1166–1185, July 2009.

[5] J. W. Goodman, F. J. Leonberger, , and R. A. Athale, "Optical interconnections for VLSI systems," *Proceedings of the IEEE*, vol. 72, no. 7, pp. 850–866, July 1984.

[6] D. A. B. Miller, "Rationale and challenges for optical interconnects to electronic chips," *Proceedings of the IEEE*, vol. 88, no. 6, pp. 728–749, June 2000.

[7] F. Kiamilev, P. Marchand, A. V. Krishnamoorthy, S. C. Esener, and S. H. Lee, "Performance comparison between optoelectronic and VLSI multistage interconnection networks," *Journal of Lightwave Technology*, vol. 9, no. 12, pp. 1674–1692, Dec 1991.

[8] A. V. Krishnamoorthy and D. A. B. Miller, "Scaling optoelectronic-VLSI circuits into the 21st century: a technology roadmap," *IEEE Journal of Selected Topics in Quantum Electronics*, vol. 2, no. 1, pp. 55–76, April 1996.

[9] D. A. B. Miller, "Optical interconnects to silicon," *IEEE Journal of Selected Topics in Quantum Electronics*, vol. 6, no. 6, pp. 1312–1317, Nov 2000.

[10] H. Soda, K. ichi Iga, C. Kitahara, and Y. Suematsu, "GaInAsP/InP Surface Emitting Injection Lasers," *Japanese Journal of Applied Physics*, vol. 18, no. 12, pp. 2329–2330, dec 1979.

[11] J. A. Kash, F. E. Doany, L. Schares, C. L. Schow, C. Schuster, D. M. Kuchta, P. K. Pepeljugoski, J. M. Trewhella, C. W. Baks, R. A. John, L. Shan, Y. H. Kwark, R. A. Budd, P. Chiniwalla, F. R. Libsch, J. Rosner, C. K. Tsang, C. S. Patel, J. D. Schaub, D. Kucharski, D. Guckenberger, S. Hegde, H. Nyikal, R. Dangel, and F. Horst, "Chip-to-chip optical interconnects," in *Optical Fiber Communication Conference and Exposition and The National Fiber Optic Engineers Conference*. Optical Society of America, 2006, p. OFA3.

[12] P. Moser, J. A. Lott, P. Wolf, G. Larisch, H. Li, N. N. Ledentsov, and D. Bimberg, "56 fJ dissipated energy per bit of oxide-confined 850 nm VCSELs operating at 25 Gbit/s," *Electronics Letters*, vol. 48, no. 20, pp. 1292–1294, Sep. 2012.

[13] S. J. B. Yoo, "The role of photonics in future computing systems and data centers," in *2013 18th OptoElectronics and Communications Conference held jointly with 2013 International Conference on Photonics in Switching (OECC/PS)*, June 2013, pp. 1–2.

[14] H. Nasu, "Short-reach optical interconnects employing high-density parallel-optical modules," *IEEE Journal of Selected Topics in Quantum Electronics*, vol. 16, no. 5, pp. 1337–1346, Sep. 2010.

[15] C. Doerr, "Silicon photonic integration in telecommunications," *Frontiers in Physics*, vol. 3, p. 37, 2015.

[16] A. V. Krishnamoorthy, H. Schwetman, X. Zheng, and R. Ho, "Energy-efficient photonics in future high-connectivity computing systems," *Journal of Lightwave Technology*, vol. 33, no. 4, pp. 889–900, Feb 2015.

[17] D. Tsiokos and G. Kanellos, *Optical interconnects: Fundamentals*, ser. Woodhead Publishing Series in Electronic and Optical Materials. Woodhead Publishing, 2017, pp. 43–73.

[18] A. Vahdat, H. Liu, and C. Johnson, "The emerging optical data center," in *2011 Optical Fiber Communication Conference and Exposition and the National Fiber Optic Engineers Conference*, March 2011, pp. 1–3.

[19] D. M. Gill, J. E. Proesel, C. Xiong, J. S. Orcutt, J. C. Rosenberg, M. H. Khater, T. Barwicz, S. Assefa, S. M. Shank, C. Reinholm, J. Ellis-Monaghan, E. Kiewra, S. Kamlapurkar, C. M. Breslin, W. M. J. Green, W. Haensch, and Y. A. Vlasov, "Demonstration of a high extinction ratio monolithic CMOS integrated nanophotonic transmitter and 16 Gb/s optical link," *IEEE Journal of Selected Topics in Quantum Electronics*, vol. 21, no. 4, pp. 212–222, July 2015.

[20] J. B. Driscoll, P. Doussiere, S. Islam, R. Narayan, W. Lin, H. Mahalingam, J. S. Park, Y. Lin, K. Nguyen, K. Roelofs, A. Dahal, R. Venables, L. Liao, R. Jones, D. Zhu, S. Priyadarshi, B. Parthasarathy, and Y. Akulova, "First 400G 8-channel CWDM silicon photonic integrated transmitter," in *2018 IEEE 15th International Conference on Group IV Photonics (GFP)*, Aug 2018, pp. 1–2.

[21] T. Pinguet, S. Denton, S. Gloeckner, M. Mack, G. Masini, A. Mekis, S. Pang, M. Peterson, S. Sahni, and P. D. Dobbelaere, "High-volume manufacturing platform for silicon photonics," *Proceedings of the IEEE*, vol. 106, no. 12, pp. 2281–2290, Dec 2018.

[22] A. La Porta, J. Weiss, R. Dangel, D. Jubin, N. Meier, J. Hofrichter, C. Caer, F. Horst, and B. J. Offrein, "Silicon photonics packaging for highly scalable optical interconnects," in *2015 IEEE 65th Electronic Components and Technology Conference (ECTC)*, May 2015, pp. 1299–1304.

[23] J. Happich, "CMOS-compatible intra-chip photonics brings new class of sensors," https://www.eenewseurope.com/news/, October 2013, accessed: May-02-2019.

[24] H. D. Thacker, X. Zheng, J. Lexau, R. Shafiiha, I. Shubin, S. Lin, S. Djordjevic, P. Amberg, E. Chang, F. Liu, J. Simons, J.-H. Lee, A. Abed, H. Liang, Y. Luo, J. Yao, D. Feng, M. Asghari, R. Ho, K. Raj, J. E. Cunningham, and A. V. Krishnamoorthy, "An all-solid-state, WDM silicon photonic digital link for chip-to-chip communications," *Optics Express*, vol. 23, no. 10, pp. 12 808–12 822, May 2015.

[25] C. T. D. Anthony L. Lentine, "Challenges in the implementation of dense wavelength division multiplexed (DWDM) optical interconnects using resonant silicon photonics," in *Proc. SPIE, Broadband Access Communication Technologies*, vol. 9772, 2016.

[26] R. Essiambre, G. Kramer, P. J. Winzer, G. J. Foschini, and B. Goebel, "Capacity limits of optical fiber networks," *Journal of Lightwave Technology*, vol. 28, no. 4, pp. 662–701, Feb 2010.

[27] P. J. Winzer, "Energy-efficient optical transport capacity scaling through spatial multiplexing," *IEEE Photonics Technology Letters*, vol. 23, no. 13, pp. 851–853, July 2011.

[28] J. Wang, S. Chen, and D. Dai, "Silicon hybrid demultiplexer with 64 channels for wavelength/mode-division multiplexed on-chip optical interconnects," *Optics Letters*, vol. 39, no. 24, pp. 6993–6996, Dec 2014.

[29] D. Dai, "Silicon nanophotonic integrated devices for on-chip multiplexing and switching," *Journal of Light. Tech.*, vol. 35, no. 4, pp. 572–587, Feb 2017.

[30] L.-W. Luo, N. Ophir, C. P. Chen, L. H. Gabrielli, C. B. Poitras, K. Bergman, and M. Lipson, "WDM-compatible mode-division multiplexing on a silicon chip," *Nature Communications*, vol. 5, p. 3069, Jan 2014.

[31] H. Jia, T. Zhou, L. Zhang, J. Ding, X. Fu, and L. Yang, "Optical switch compatible with wavelength division multiplexing and mode division multiplexing for photonic networks-on-chip," *Optics Express*, vol. 25, no. 17, pp. 20 698–20 707, Aug 2017.

[32] T. Zhou, H. Jia, J. Ding, L. Zhang, X. Fu, and L. Yang, "On-chip broadband silicon thermo-optic 2×2 four-mode optical switch for optical space and local mode switching," *Optics Express*, vol. 26, no. 7, pp. 8375–8384, Apr 2018.

[33] D. Dai, J. Wang, and S. He, "silicon multimode photonic integrated devices for on-chip mode-division-multiplexed optical interconnects," *Progress in Electromagnetics Research*, vol. 143, pp. 773–819, 2013.

[34] B. G. Lee, N. Dupuis, P. Pepeljugoski, L. Schares, R. Budd, J. R. Bickford, and C. L. Schow, "Silicon photonic switch fabrics in computer communications systems," *Journal of Lightwave Technology*, vol. 33, no. 4, p. 768777, Feb 2015.

[35] E. Ramírez-Cruz, R. Gutiérrez-Castrejón, P. Torres-Ferrera, and D. Ceballos-Herrera, "An alternative for the implementation of 40-km reach Ethernet at 400 Gb/s using an 8×50 Gb/s PHY at 1310 nm with SOA pre-amplification," *Optical Switching and Networking*, vol. 22, pp. 86–94, 2016.

[36] L. Lu, S. Zhao, L. Zhou, D. Li, Z. Li, M. Wang, X. Li, and J. Chen, "16 × 16 non-blocking silicon optical switch based on electro-optic Mach-Zehnder interferometers," *Optics Express*, vol. 24, no. 9, pp. 9295–9307, May 2016.

[37] L. Qiao, W. Tang, and T. Chu, "32 × 32 silicon electro-optic switch with built-in monitors and balanced-status units," *Scientific Reports*, vol. 7, no. 42306, Feb. 2017.

[38] D. Dai, J. Wang, and S. He, "Silicon multimode photonic integrated devices for on-chip mode-division-multiplexed optical interconnects (invited review)," *Progress In Electromagnetics Research*, vol. 143, pp. 773–819, Dec 2013.

[39] N. Dupuis, B. G. Lee, A. V. Rylyakov, D. M. Kuchta, C. W. Baks, J. S. Orcutt, D. M. Gill, W. M. J. Green, and C. L. Schow, "Design and fabrication of low-insertion-loss and low-crosstalk broadband 2 × 2 MachZehnder silicon photonic switches," *Journal of Lightwave Technology*, vol. 33, no. 17, pp. 3597–3606, Sep. 2015.

[40] M. R. Watts, J. Sun, C. DeRose, D. C. Trotter, R. W. Young, and G. N. Nielson, "Adiabatic thermo-optic Mach-Zehnder switch," *Optics Letters*, vol. 38, no. 5, pp. 733–735, Mar 2013.

[41] G. Coppola, L. Sirleto, I. Rendina, and M. Iodice, "Advance in thermo-optical switches: principles, materials, design, and device structure," *Optical Engineering*, vol. 50, no. 7, pp. 1–15, 2011.

[42] E. Havinga, "The temperature dependence of dielectric constants," *Journal of Physics and Chemistry of Solids*, vol. 18, no. 2, pp. 253–255, 1961.

[43] A. J. Bosman and E. E. Havinga, "Temperature dependence of dielectric constants of cubic ionic compounds," *Physical Review*, vol. 129, pp. 1593–1600, Feb 1963.

[44] Y. Tsay, B. Bendow, and S. S. Mitra, "Theory of the temperature derivative of the refractive index in transparent crystals," *Physical Review B*, vol. 8, pp. 2688–2696, Sep 1973.

[45] Y. Varshni, "Temperature dependence of the energy gap in semiconductors," *Physica*, vol. 34, no. 1, pp. 149–154, 1967.

[46] G. Ghosh, *Handbook of Thermo-optic Coefficient of Optical Materials with Applications.* Academic Press, 1997, ch. 3: Thermo-optic Coefficients.

[47] W. Sellmeier, "Ueber die durch aetherschwingungen erregten mitschwingungen der körpertheilchen und deren rückwirkung auf die ersteren, besonders zur erklärung der dispersion und ihrer anomalien," *Annalen der Physik*, vol. 221, no. 4, pp. 520–549, 1872.

[48] B. J. Frey, D. B. Leviton, and T. J. Madison, "Temperature-dependent refractive index of silicon and germanium," in *Proceedings of SPIE - The International Society for Optical Engineering*, vol. 6273, 2006.

[49] T. S. El-Bawab, *Optical Switching.* Springer US, 2006, ch. 4: Thermo-optic Switching.

[50] L. Chrostowski and M. Hochberg, *Silicon Photonics Design: From Devices to Systems.* Cambridge University Press, 2015.

[51] U. Fischer, T. Zinke, B. Schuppert, and K. Petermann, "Singlemode optical switches based on SOI waveguides with large cross-section," *Electronics Letters*, vol. 30, no. 5, pp. 406–408, March 1994.

[52] Y. Hida, H. Onose, and S. Imamura, "Polymer waveguide thermooptic switch with low electric power consumption at 1.3 μm," *IEEE Photonics Technology Letters*, vol. 5, no. 7, pp. 782–784, July 1993.

[53] Z. Lu, K. Murray, H. Jayatilleka, and L. Chrostowski, "Michelson interferometer thermo-optic switch on SOI with a 50-μW power consumption," *IEEE Photonics Technology Letters*, vol. 27, no. 22, pp. 2319–2322, Nov 2015.

[54] J. E. Cunningham, I. Shubin, X. Zheng, T. Pinguet, A. Mekis, Y. Luo, H. Thacker, G. Li, J. Yao, K. Raj, and A. V. Krishnamoorthy, "Highly-efficient thermally-tuned resonant optical filters," *Optics Express*, vol. 18, no. 18, pp. 19 055–19 063, Aug 2010.

[55] Q. Fang, J. F. Song, T. Liow, H. Cai, M. B. Yu, G. Q. Lo, and D. Kwong, "Ultralow power silicon photonics thermo-optic switch with suspended phase arms," *IEEE Photonics Technology Letters*, vol. 23, no. 8, pp. 525–527, April 2011.

[56] R. L. Espinola, M. C. Tsai, J. T. Yardley, and R. M. Osgood, "Fast and low-power thermooptic switch on thin silicon-on-insulator," *IEEE Photonics Technology Letters*, vol. 15, no. 10, pp. 1366–1368, Oct 2003.

[57] A. von Meier, *Electric Power Systems: A Conceptual Introduction*, ser. Wiley Survival Guides in Engineering and Science. Wiley, 2006. [Online]. Available: https://books.google.ca/books?id=bWAi22IB3lkC

[58] A. Masood, M. Pantouvaki, D. Goossens, G. Lepage, P. Verheyen, J. V. Campenhout, P. Absil, D. V. Thourhout, and W. Bogaerts, "Fabrication and characterization of CMOS-compatible integrated tungsten heaters for thermo-optic tuning in silicon photonics devices," *Optical Materials Express*, vol. 4, no. 7, pp. 1383–1388, Jul 2014.

[59] A. Masood, M. Pantouvaki, G. Lepage, P. Verheyen, J. Van Campenhout, P. Absil, D. Van Thourhout, and W. Bogaerts, "Comparison of heater architectures for thermal control of silicon photonic circuits," in *10th International Conference on Group IV Photonics*, Aug 2013, pp. 83–84.

[60] N. C. Harris, Y. Ma, J. Mower, T. Baehr-Jones, D. Englund, M. Hochberg, and C. Galland, "Efficient, compact and low loss thermo-optic phase shifter in silicon," *Optics Express*, vol. 22, no. 9, pp. 10 487–10 493, May 2014.

[61] K. S. Novoselov, A. K. Geim, S. V. Morozov, D. Jiang, Y. Zhang, S. V. Dubonos, I. V. Grigorieva, and A. A. Firsov, "Electric field effect in atomically thin carbon films," *Science*, vol. 306, no. 5696, pp. 666–669, 2004.

[62] K. Solehmainen, M. Kapulainen, M. Harjanne, and T. Aalto, "Adiabatic and multimode interference couplers on silicon-on-insulator," *IEEE Photonics Technology Letters*, vol. 18, no. 21, pp. 2287–2289, Nov 2006.

[63] L. B. Soldano and E. C. M. Pennings, "Optical multi-mode interference devices based on self-imaging: principles and applications," *Journal of Lightwave Technology*, vol. 13, no. 4, pp. 615–627, April 1995.

[64] H. Yang, Y. Kuan, T. Xiang, Y. Zhu, X. Cai, and L. Liu, "Broadband polarization-insensitive optical switch on silicon-on-insulator platform," *Optics Express*, vol. 26, no. 11, pp. 14 340–14 345, May 2018.

[65] S. Wang and D. Dai, "Polarization-insensitive 2×2 thermo-optic Mach-Zehnder switch on silicon," *Optics Letters*, vol. 43, no. 11, pp. 2531–2534, Jun 2018.

[66] H. Zhou, J. Song, E. K. S. Chee, C. Li, H. Zhang, and G. Lo, "A compact thermo-optical multimode-interference silicon-based 1×4 nano-photonic switch," *Optics Express*, vol. 21, no. 18, pp. 21 403–21 413, Sep 2013.

[67] S. Kim, J. You, H. Rhee, D. E. Yoo, D. Lee, K. Yu, and H. Park, "High-performance silicon MMI switch based on thermo-optic control of interference modes," *IEEE Photonics Technology Letters*, vol. 30, no. 16, pp. 1427–1430, Aug 2018.

[68] H. Zhou, J. Song, E. K. S. Chee, C. Li, H. Zhang, and G. Lo, "A compact thermo-optical multimode-interference silicon-based 1×4 nano-photonic switch," *Optics Express*, vol. 21, no. 18, pp. 21 403–21 413, Sep 2013.

[69] R. B. Priti and O. Liboiron-Ladouceur, "A reconfigurable multimode demultiplexer/switch for mode-multiplexed silicon photonics interconnects," *IEEE Journal of Selected Topics in Quantum Electronics*, vol. 24, no. 6, pp. 1–10, Nov 2018.

[70] R. B. Priti, H. P. Bazargani, Y. Xiong, and O. Liboiron-Ladouceur, "Mode selecting switch using multimode interference for on-chip optical interconnects," *Optics Letters*, vol. 42, no. 20, pp. 4131–4134, Oct 2017.

[71] T. Uematsu, Y. Ishizaka, Y. Kawaguchi, K. Saitoh, and M. Koshiba, "Design of a compact two-mode multi/demultiplexer consisting of multimode interference waveguides and a wavelength-insensitive phase shifter for mode-division multiplexing transmission," *Journal of Lightwave Technology*, vol. 30, no. 15, pp. 2421–2426, Aug 2012.

[72] J. Leuthold, R. Hess, J. Eckner, P. A. Besse, and H. Melchior, "Spatial mode filters realized with multimode interference couplers," *Optics Letters*, vol. 21, no. 11, pp. 836–838, Jun 1996.

[73] A. Yariv and P. Yeh, *Photonics: Optical Electronics in Modern Communications*, ser. Oxford Series in Electrical an. Oxford University Press, 2007.

[74] Y. Shoji, K. Kintaka, S. Suda, H. Kawashima, T. Hasama, and H. Ishikawa, "Low-crosstalk 2×2 thermo-optic switch with silicon wire waveguides," *Optics Express*, vol. 18, no. 9, pp. 9071–9075, Apr 2010.

[75] J. Song, Q. Fang, S. H. Tao, T. Y. Liow, M. B. Yu, G. Q. Lo, and D. L. Kwong, "Fast and low power michelson interferometer thermo-optical switch on SOI," *Optics Express*, vol. 16, no. 20, pp. 15 304–15 311, Sep 2008.

[76] S. Chen, Y. Shi, S. He, and D. Dai, "Low-loss and broadband 2×2 silicon thermo-optic Mach–Zehnder switch with bent directional couplers," *Optics Letters*, vol. 41, no. 4, pp. 836–839, Feb 2016.

[77] D. Dai, J. Wang, and Y. Shi, "Silicon mode (de)multiplexer enabling high capacity photonic networks-on-chip with a single-wavelength-carrier light," *Optics Letters*, vol. 38, no. 9, pp. 1422–1424, May 2013.

[78] S. Wang, H. Wu, M. Zhang, and D. Dai, "A 32-channel hybrid wavelength-/mode-division (de)multiplexer on silicon," *IEEE Photonics Technology Letters*, vol. 30, no. 13, pp. 1194–1197, July 2018.

[79] C. Pollock and M. Lipson, *Integrated Photonics*. Springer US, 2003, ch. 3.

[80] W. J. Westerveld and H. P. Urbach, *Silicon Photonics*, ser. 2053-2563. IOP Publishing, 2017, ch. 2:Waveguide.

[81] C. Li, D. Liu, and D. Dai, "Multimode silicon photonics," *Nanophotonics*, vol. 0, no. 0, 2018.

[82] R. J. Essiambre, R. Ryf, N. K. Fontaine, and S. Randel, "Breakthroughs in photonics 2012: Space-division multiplexing in multimode and multicore fibers for high-capacity optical communication," *IEEE Photonics Journal*, vol. 5, no. 2, pp. 0 701 307–0 701 307, April 2013.

[83] D. J. Richardson, J. M. Fini, and L. E. Nelson, "Space-division multiplexing in optical fibres," *Nature Photonics*, vol. 7, pp. 354–362, 2013.

[84] Y. Huang, G. Xu, and S. Ho, "An ultracompact optical mode order converter," *IEEE Photonics Technology Letters*, vol. 18, no. 21, pp. 2281–2283, Nov 2006.

[85] F. Guo, D. Lu, R. Zhang, H. Wang, W. Wang, and C. Ji, "Two-mode converters at 1.3 μm based on multimode interference couplers on InP substrates," *Chinese Physics Letters*, vol. 33, no. 2, p. 024203, Feb 2016.

[86] A. Hosseini, J. Covey, D. N. Kwong, and R. T. Chen, "Tapered multi-mode interference couplers for high order mode power extraction," *Journal of Optics*, vol. 12, no. 7, p. 075502, Jun 2010.

[87] Y. Chaen, R. Tanaka, and K. Hamamoto, "Optical mode converter using multi-mode interference structure," in *Technical Digest of the Eighteenth Microoptics Conference*, Oct 2013, pp. 1–2.

[88] D. Dai, Y. Tang, and J. E. Bowers, "Mode conversion in tapered submicron silicon ridge optical waveguides," *Optics Express*, vol. 20, no. 12, pp. 13 425–13 439, Jun 2012.

[89] D. Chen, X. Xiao, L. Wang, Y. Yu, W. Liu, and Q. Yang, "Low-loss and fabrication tolerant silicon mode-order converters based on novel compact tapers," *Optics Express*, vol. 23, no. 9, pp. 11 152–11 159, May 2015.

[90] J. Qiu, D. Zhang, Y. Tian, J. Wu, Y. Li, and Y. Wang, "Performance analysis of a broadband second-order mode converter based on multimode interference coupler and phase shifter," *IEEE Photonics Journal*, vol. 7, no. 5, pp. 1–8, Oct 2015.

[91] J. Leuthold, J. Eckner, E. Gamper, P. A. Besse, and H. Melchior, "Multimode interference couplers for the conversion and combining of zero- and first-order modes," *Journal of Lightwave Technology*, vol. 16, no. 7, pp. 1228–1239, July 1998.

[92] Y. Kawaguchi and K. Tsutsumi, "Mode multiplexing and demultiplexing devices using multimode interference couplers," *Electronics Letters*, vol. 38, no. 25, pp. 1701–1702, Dec 2002.

[93] M. Ye, Y. Yu, J. Zou, W. Yang, and X. Zhang, "On-chip multiplexing conversion between wavelength division multiplexing - polarization division multiplexing and wavelength division multiplexing - mode division multiplexing," *Optics Letters*, vol. 39, no. 4, pp. 758–761, Feb 2014.

[94] Y. Ding, J. Xu, F. D. Ros, B. Huang, H. Ou, and C. Peucheret, "On-chip two-mode division multiplexing using tapered directional coupler-based mode multiplexer and demultiplexer," *Optics Express*, vol. 21, no. 8, pp. 10 376–10 382, Apr 2013.

[95] J. Xing, Z. Li, X. Xiao, J. Yu, and Y. Yu, "Two-mode multiplexer and demultiplexer based on adiabatic couplers," *Optics Letters*, vol. 38, no. 17, pp. 3468–3470, Sep 2013.

[96] J. B. Driscoll, R. R. Grote, B. Souhan, J. I. Dadap, M. Lu, and R. M. Osgood, "Asymmetric Y junctions in silicon waveguides for on-chip mode-division multiplexing," *Optics Letters*, vol. 38, no. 11, pp. 1854–1856, Jun 2013.

[97] W. Chen, P. Wang, T. Yang, G. Wang, T. Dai, Y. Zhang, L. Zhou, X. Jiang, and J. Yang, "Silicon three-mode (de)multiplexer based on cascaded asymmetric Y-junctions," *Optics Letters*, vol. 41, no. 12, pp. 2851–2854, Jun 2016.

[98] C. Sun, Y. Yu, M. Ye, G. Chen, and X. Zhang, "An ultra-low crosstalk and broadband two-mode (de)multiplexer based on adiabatic couplers," *Scientific Reports*, vol. 6, no. 38494, Dec 2016.

[99] Z. Zhang, Y. Yu, and S. Fu, "Broadband on-chip mode-division multiplexer based on adiabatic couplers and symmetric Y-junction," *IEEE Photonics Journal*, vol. 9, no. 2, pp. 1–6, April 2017.

[100] Y. Li, C. Li, C. Li, B. Cheng, and C. Xue, "Compact two-mode (de)multiplexer based on symmetric Y-junction and multimode interference waveguides," *Optics Express*, vol. 22, no. 5, pp. 5781–5786, Mar 2014.

[101] F. Guo, D. Lu, R. Zhang, H. Wang, and C. Ji, "A two-mode (de)multiplexer based on multimode interferometer coupler and Y-junction on inp substrate," *IEEE Photonics Journal*, vol. 8, no. 1, pp. 1–8, Feb 2016.

[102] H. Xiao, Z. Liu, X. Han, J. Yang, G. Ren, A. Mitchell, and Y. Tian, "On-chip reconfigurable and scalable optical mode multiplexer/demultiplexer based on three-waveguide-coupling structure," *Optics Express*, vol. 26, no. 17, pp. 22 366–22 377, Aug 2018.

[103] Q. Huang, Y. Wu, W. Jin, and K. S. Chiang, "Mode multiplexer with cascaded vertical asymmetric waveguide directional couplers," *Journal of Lightwave Technology*, vol. 36, no. 14, pp. 2903–2911, July 2018.

[104] W. Jiang, "Reconfigurable three-dimensional mode (de)multiplexer/switch via triple-silicon-ITO-waveguide directional coupler," *Opt. Express*, vol. 26, no. 20, pp. 26 257–26 271, Oct 2018.

[105] J. Wang, S. Chen, and D. Dai, "Silicon hybrid demultiplexer with 64 channels for wavelength/mode-division multiplexed on-chip optical interconnects," *Optics Letters*, vol. 39, no. 24, pp. 6993–6996, Dec 2014.

[106] C. Sun, Y. Yu, G. Chen, and X. Zhang, "Silicon mode multiplexer processing dual-path mode-division multiplexing signals," *Optics Letters*, vol. 41, no. 23, pp. 5511–5514, Dec 2016.

[107] B. Stern, X. Zhu, C. P. Chen, L. D. Tzuang, J. Cardenas, K. Bergman, and M. Lipson, "On-chip mode-division multiplexing switch," *Optica*, vol. 2, no. 6, pp. 530–535, Jun 2015.

[108] R. Imansyah, T. Tanaka, L. Himbele, H. Jiang, and K. Hamamoto, "Electrically controlled optical-mode switch for fundamental mode and first order mode," *Japanese Journal of Applied Physics*, vol. 55, no. 8S3, p. 08RB06, Jul 2016.

[109] C. Sun, Y. Yu, G. Chen, and X. Zhang, "On-chip switch for reconfigurable mode-multiplexing optical network," *Optics Express*, vol. 24, no. 19, pp. 21 722–21 728, Sep 2016.

[110] Q. Huang, W. Jin, and K. S. Chiang, "Broadband mode switch based on a three-dimensional waveguide Mach-Zehnder interferometer," *Optics Letters*, vol. 42, no. 23, pp. 4877–4880, Dec 2017.

[111] Z. Zhang, X. Hu, and J. Wang, "On-chip optical mode exchange using tapered directional coupler," *Scientific Reports*, vol. 5, p. 16072, Nov 2015.

[112] C. Sun, Y. Yu, G. Chen, and X. Zhang, "Integrated switchable mode exchange for reconfigurable mode-multiplexing optical networks," *Optics Letters*, vol. 41, no. 14, pp. 3257–3260, Jul 2016.

[113] M. Ye, Y. Yu, C. Sun, and X. Zhang, "On-chip data exchange for mode division multiplexed signals," *Optics Express*, vol. 24, no. 1, pp. 528–535, Jan 2016.

[114] L. Yang, T. Zhou, H. Jia, S. Yang, J. Ding, X. Fu, and L. Zhang, "General architectures for on-chip optical space and mode switching," *Optica*, vol. 5, no. 2, pp. 180–187, Feb 2018.

[115] C. Sun, W. Wu, Y. Yu, G. Chen, X. Zhang, X. Chen, D. J. Thomson, and G. T. Reed, "De-multiplexing free on-chip low-loss multimode switch enabling reconfigurable intermode and inter-path routing," *Nanophotonics*, vol. 7, no. 9, pp. 1571–1580, Jul 2018.

[116] Y. Xiong, R. B. Priti, and O. Liboiron-Ladouceur, "High-speed two-mode switch for mode-division multiplexing optical networks," *Optica*, vol. 4, no. 9, pp. 1098–1102, Sep 2017.

[117] R. B. Priti and O. Liboiron-Ladouceur, "A broadband rearrangable non-blocking MZI-based thermo-optic O-band switch in silicon-on-insulator," in *Advanced Photonics 2017 (IPR, NOMA, Sensors, Networks, SPPCom, PS)*. Optical Society of America, 2017, p. PM4D.2.

[118] R. B. Priti, G. Zhang, and O. Liboiron-Ladouceur, "3×10 Gb/s silicon three-mode switch with 120° hybrid based unbalanced Mach-Zehnder interferometer," *Optics Express*, vol. 27, no. 10, pp. 14 199–14 212, May 2019.

[119] M. R. Watts, J. Sun, C. DeRose, D. C. Trotter, R. W. Young, and G. N. Nielson, "Adiabatic thermo-optic Mach-Zehnder switch," *Optics Letters*, vol. 38, no. 5, pp. 733–735, Mar 2013.

[120] W. S. Fegadolli, G. Vargas, X. Wang, F. Valini, L. A. M. Barea, J. E. B. Oliveira, N. Frateschi, A. Scherer, V. R. Almeida, and R. R. Panepucci, "Reconfigurable silicon thermo-optical ring resonator switch based on Vernier effect control," *Optics Express*, vol. 20, no. 13, pp. 14 722–14 733, Jun 2012.

[121] L. Lu, L. Zhou, S. Li, Z. Li, X. Li, and J. Chen, "4×4 nonblocking silicon thermo-optic switches based on multimode interferometers," *Journal of Lightwave Technology*, vol. 33, no. 4, pp. 857–864, 2015.

[122] M. Nikdast, G. Nicolescu, J. Trajkovic, and O. Liboiron-Ladouceur, "Chip-scale silicon photonic interconnects: A formal study on fabrication non-uniformity," *Journal of Lightwave Technology*, vol. 34, no. 16, pp. 3682–3695, Aug 2016.

[123] J. V. Campenhout, W. M. J. Green, S. Assefa, and Y. A. Vlasov, "Low-power, 2×2 silicon electro-optic switch with 110-nm bandwidth for broadband reconfigurable optical networks," *Optics Express*, vol. 17, no. 26, pp. 24 020–24 029, Dec 2009.

[124] K. Jinguji, N. Takato, A. Sugita, and M. Kawachi, "Mach-Zehnder interferometer type optical waveguide coupler with wavelength-flattened coupling ratio," *Electronics Letters*, vol. 26, no. 17, pp. 1326–1327, Aug 1990.

[125] L. Chen and Y. Chen, "Compact, low-loss and low-power 8×8 broadband silicon optical switch," *Optics Express*, vol. 20, no. 17, pp. 18 977–18 985, Aug 2012.

[126] A. Masood, M. Pantouvaki, G. Lepage, P. Verheyen, J. Van Campenhout, P. Absil, D. Van Thourhout, and W. Bogaerts, "Comparison of heater architectures for thermal control of silicon photonic circuits," in *10th International Conference on Group IV Photonics*, Aug 2013, pp. 83–84.

[127] M. S. Hai, M. M. P. Fard, D. An, F. Gambini, S. Faralli, G. B. Preve, G. W. Roberts, and O. Liboiron-Ladouceur, "Automated characterization of SiP MZI-based switches," in *2015 IEEE Optical Interconnects Conference (OI)*, April 2015, pp. 94–95.

[128] H. Shoman, H. Jayatilleka, A. H. K. Park, A. Mistry, N. A. F. Jaeger, S. Shekhar, and L. Chrostowski, "Compact wavelength- and bandwidth-tunable microring modulator," *Optics Express*, vol. 27, no. 19, pp. 26 661–26 675, Sep 2019.

[129] N. Dupuis, F. Doany, R. A. Budd, L. Schares, C. W. Baks, D. M. Kuchta, T. Hirokawa, and B. G. Lee, "A nonblocking 4×4 Mach-Zehnder switch with integrated gain and nanosecond-scale reconfiguration time," in *Optical Fiber Communication Conference (OFC) 2019*. Optical Society of America, 2019, p. W1E.2.

[130] L. Lu, S. Zhao, L. Zhou, D. Li, Z. Li, M. Wang, X. Li, and J. Chen, "16×16 non-blocking silicon optical switch based on electro-optic Mach-Zehnder interferometers," *Optics Express*, vol. 24, no. 9, pp. 9295–9307, May 2016.

[131] L. Chung, S. Lee, and Y. Lin, "Principles and application of reduced beat length in MMI couplers," *Optics Express*, vol. 14, no. 19, pp. 8753–8764, Sep 2006.

[132] Y. Fu, T. Ye, W. Tang, and T. Chu, "Efficient adiabatic silicon-on-insulator waveguide taper," *Photonics Research*, vol. 2, no. 3, pp. A41–A44, Jun 2014.

[133] O. Svelto, *Ray and Wave Propagation through Optical Media.* Boston, MA: Springer US, 1998, pp. 129–160.

[134] D. F. Grosz and R. J. Essiambre, "On the role of optical fibers as channel decorrelators in system experiments," in *13th Annual Meeting of IEEE Lasers and Electro-Optics Society 2000 (Cat. No 00CH37080)*, vol. 1, Nov 2000, pp. 340–341.

[135] H. Xiao, L. Deng, G. Zhao, Z. Liu, Y. Meng, X. Guo, G. Liu, S. Liu, J. Ding, and Y. Tian, "Optical mode switch based on multimode interference couplers," *Journal of Optics*, vol. 19, no. 2, p. 025802, Dec 2016.

[136] R. B. Priti, Y. Xiong, and O. Liboiron-Ladouceur, "Efficiency improvement of an O-band SOI-MZI thermo-optic matrix switch," in *2016 IEEE Photonics Conference (IPC)*, Oct 2016, pp. 823–824.

[137] X. Zheng, Y. Luo, J. Lexau, F. Liu, G. Li, H. D. Thacker, I. Shubin, J. Yao, R. Ho, J. E. Cunningham, and A. V. Krishnamoorthy, "2-pJ/bit (on-chip) 10-Gb/s digital CMOS silicon photonic link," *IEEE Photonics Technology Letters*, vol. 24, no. 14, pp. 1260–1262, July 2012.

[138] C. A. Thraskias, E. N. Lallas, N. Neumann, L. Schares, B. J. Offrein, R. Henker, D. Plettemeier, F. Ellinger, J. Leuthold, and I. Tomkos, "Survey of photonic and plasmonic interconnect technologies for intra-data center and high-performance computing communications," *IEEE Communications Surveys Tutorials*, vol. 20, no. 4, pp. 2758–2783, 2018.

[139] X. Zhou, H. Liu, R. Urata, t. . S. l. d. c. i. C. Sara Zebian", and solutions, *Optical Fiber Technology*, vol. 44, pp. 61–68, 2018.

[140] R. B. Priti, F. Shokraneh, and O. Liboiron-Ladouceur, "Scalable 2×2 multimode switch for mode-multiplexed silicon photonics interconnects," in *2018 Asia Communications and Photonics Conference (ACP)*, October 2018, pp. 1–3.

[141] R. B. Priti and O. Liboiron-Ladouceur, "Reconfigurable and scalable multimode silicon photonics switch for energy-efficient mode-division-multiplexing systems," *IEEE Journal of Lightwave Technology*, 2019, in Press.

[142] P. J. Reyes-Iglesias, I. Molina-Fernández, A. Moscoso-Mártir, and A. Ortega-Moñux, "High-performance monolithically integrated 120° downconverter with relaxed hardware constraints," *Optics Express*, vol. 20, no. 5, pp. 5725–5741, Feb 2012.

[143] J. D. Love and N. Riesen, "Single-, few-, and multimode Y-junctions," *Journal of Lightwave Technology*, vol. 30, no. 3, pp. 304–309, Feb 2012.

[144] M. Teng, K. Kojima, T. Koike-Akino, B. Wang, C. Lin, and K. Parsons, "Broadband SOI mode order converter based on topology optimization," in *2018 Optical Fiber Communications Conference and Exposition (OFC)*, March 2018, p. 13.

[145] "NanoSOI fabrication process," http://www.appliednt.com/nanosoi/, accessed: April-29-2019.

[146] "MMI coupler," https://www.lumerical.com/, accessed: April-29-2019.

[147] S. Paul, C. Gierl, J. Cesar, Q. T. Le, M. Malekizandi, B. Kögel, C. Neumeyr, M. Ortsiefer, and F. Köppers, “10-Gb/s direct modulation of widely tunable 1550-nm MEMS VCSEL,” *IEEE Journal of Selected Topics in Quantum Electronics*, vol. 21, no. 6, pp. 436–443, Nov 2015.

[148] Z. Xuan, R. Ding, Y. Liu, T. Baehr-Jones, M. Hochberg, and F. Aflatouni, “A low-power hybrid-integrated 40-Gb/s optical receiver in silicon,” *IEEE Transactions on Microwave Theory and Techniques*, vol. 66, pp. 589–595, 2018.

[149] W. Hamad, M. B. Sanayeh, T. Siepelmeyer, H. Hamad, and W. H. E. Hofmann, “Small-signal analysis of high-performance VCSELs,” *IEEE Photonics Journal*, vol. 11, no. 2, pp. 1–12, April 2019.

[150] C. D. Truong, D. H. Tran, T. A. Tran, and T. T. Le, “3×3 multimode interference optical switches using electro-optic effects as phase shifters,” *Optics Communications*, vol. 292, pp. 78 – 83, 2013.

[151] B. Troia, A. Z. Khokhar, M. Nedeljkovic, S. A. Reynolds, Y. Hu, G. Z. Mashanovich, and V. M. N. Passaro, “Design procedure and fabrication of reproducible silicon Vernier devices for high-performance refractive index sensing,” *Sensors*, vol. 15, no. 6, pp. 13 548–13 567, 2015.

[152] M. L. Notte and V. M. Passaro, “Ultra high sensitivity chemical photonic sensing by Mach-Zehnder interferometer enhanced Vernier-effect,” *Sensors and Actuators B: Chemical*, vol. 176, pp. 994–1007, 2013.

[153] N. S. Lagali, M. R. Paiam, R. I. MacDonald, K. Worhoff, and A. Driessen, “Analysis of generalized Mach-Zehnder interferometers for variable-ratio power splitting and optimized switching,” *Journal of Lightwave Technology*, vol. 17, no. 12, pp. 2542–2550, Dec 1999.

[154] R. M. Jenkins, J. M. Heaton, D. R. Wight, J. T. Parker, J. C. H. Birbeck, G. W. Smith, and K. P. Hilton, “Novel 1×N and N×N integrated optical switches using self-imaging multimode GaAs/AlGaAs waveguides,” *Applied Physics Letters*, vol. 64, pp. 684–686, feb 1994.

[155] F. G. de Magalhães, R. Priti, M. Nikdast, F. Hessel, O. Liboiron-Ladouceur, and G. Nicolescu, “Design and modelling of a low-latency centralized controller for optical integrated networks,” *IEEE Communications Letters*, vol. 20, no. 3, pp. 462–465, March 2016.

[156] S. Paul, C. Gierl, J. Cesar, Q. T. Le, M. Malekizandi, B. Kögel, C. Neumeyr, M. Ortsiefer, and F. Küppers, “10-Gb/s direct modulation of widely tunable 1550-nm MEMS VCSEL,” *IEEE Journal of Selected Topics in Quantum Electronics*, vol. 21, no. 6, pp. 436–443, Nov 2015.

[157] C. Kachris, K. Bergman, and I. Tomkos, Eds., *Optical Interconnects for Future Data Center Networks*, ser. Optical Networks. Springer-Verlag New York, 2013.

[158] D. A. B. Miller, "Attojoule optoelectronics for low-energy information processing and communications," *Journal of Lightwave Technology*, vol. 35, no. 3, pp. 346–396, Feb 2017.

[159] D. Dai and S. He, "Optimization of ultracompact polarization-insensitive multimode interference couplers based on Si nanowire waveguides," *IEEE Photonics Technology Letters*, vol. 18, no. 19, pp. 2017–2019, Oct 2006.

[160] Y. Zhang, S. Yang, H. Guan, A. E.-J. Lim, G.-Q. Lo, P. Magill, T. Baehr-Jones, and M. Hochberg, "Sagnac loop mirror and micro-ring based laser cavity for silicon-on-insulator," *Optics Express*, vol. 22, no. 15, pp. 17 872–17 879, Jul 2014.

[161] H.-L. Tseng, E. Chen, H. Rong, and N. Na, "High-performance silicon-on-insulator grating coupler with completely vertical emission," *Optics Express*, vol. 23, no. 19, pp. 24 433–24 439, Sep 2015.

[162] J. K. Doylend, M. J. R. Heck, J. T. Bovington, J. D. Peters, L. A. Coldren, and J. E. Bowers, "Two-dimensional free-space beam steering with an optical phased array on silicon-on-insulator," *Optics Express*, vol. 19, no. 22, pp. 21 595–21 604, Oct 2011.

[163] K. Kuhn, C. Kenyon, A. Kornfeld, M. Liu, A. Maheshwari, W. kai Shih, S. Sivakumar, G. Taylor, P. VanDerVoorn, and K. Zawadzki, "Managing process variation in Intel's 45 nm CMOS technology," *Intel Technology Journal*, vol. 12, no. 2, pp. 92–110, 2008.

[164] G. Neuberger, G. Wirth, and R. Reis, *Protecting Chips Against Hold Time Violations Due to Variability*. Springer Netherlands, 2013, ch. 2: Process Variability.

[165] L. Chrostowski, X. Wang, J. Flueckiger, Y. Wu, Y. Wang, and S. T. Fard, "Impact of fabrication non-uniformity on chip-scale silicon photonic integrated circuits," in *OFC 2014*, March 2014, pp. 1–3.